Università degli Studi "Roma Tre"

Dipartimento di Scienze

CORSO DI DOTTORATO DI RICERCA IN

Scienze della Materia, Nanotecnologie e Sistemi Complessi

XXXII° Ciclo

Antifouling nanodevices for the development of an innovative multifunctional coating

Ludovica Ruggiero

Tutors:

Prof.ssa Maria Antonietta Ricci

Dott.ssa Armida Sodo

November 2019

Contents

Chapter 1

Introduction

Since ancient times, in western countries, stone is the most widely used building material, because it is available everywhere on the Earth and offers a large variety of mechanical and aesthetic properties. It is resistant and at the same time can be moulded by using carving tools [1].

Natural stones exhibit a very heterogeneous and anisotropic fabric, with a wide range of mineral composition, textural and structural properties (e.g. porosity, pore size distribution and pore shape). The physical and chemical properties of different types of stone may differ a lot and determine different durability, in particular against weathering [2-3]. In addition to the variety of natural stones, there are plenty of man-made stone materials (concrete, brickwork, mortar) of specific colours and textures. All of them are used to fulfil the physical and technical requirements demanded by engineers and architects as well as to guarantee aesthetic and artistic values [4-5]. The variety of stone materials entails complex conservation issues.

Most historical buildings and monuments, that are a seamless part of our urban landscape, use natural stone as the main construction material and are subjected to a deterioration process that is familiar to anyone: even if some of them do not seem affected by centuries of weather exposure, the majority of stone buildings/monuments are undergoing gradual or episodic deterioration. In fact, the maintenance of outdoor stone materials and ornamentation requires an enormous amount of time and money, and specific and updated knowledge and skills by the restorers. Before taking any action to prevent or remedy the stone deterioration, it is critical to determine the causes of the deterioration process. This is not always obvious and straightforward, as sometimes several different deterioration agents act simultaneously and in a synergic manner. Besides vandalism and unintentional damage by humans, recent literature evidenced that the deterioration process is the result of a complex interaction with the environment: local climate, exposition, pollution, biological activity, interaction with other construction materials (e.g. mortars) are indeed the most relevant degradation agents [6-7].

The immediate consequence of the interaction of stone materials and their environment is a chemical and physical alteration of the stone followed, in most of the cases, by biological colonization. Stone materials, from natural to man-made, are commonly colonized by a large variety of microorganisms. The microflora, synergistically with other environmental agents and with antagonistic associations, induces transformations in rocks, also in terms of cultural value and economical viewpoints, in particular when these are used as building materials [8]. These determine degradation of both appearance and robustness of the artifacts.

This thesis deals with the biodeterioration of stone materials, and proposes innovative solutions for the reduction of the environmental impact, which increase the effectiveness of the restoration treatments over time. In detail, the thesis reports the synthesis of two different nanocontainers, which are charged with biocides and embedded into a coating suitable for protection of stones. Complete chemico-physical characterization of the nanoparticles, study of the biocide release kinetics and efficacy are also reported.

In the next paragraphs, an overview of the biodeterioration on stone materials, the topics associated with biocides, such as the method of application and the durability of the antifouling treatments, the problems linked to the interaction with the substrate, the toxicity and the innovative research points of view will be discussed in details.

1.1 Biodeterioration

The term biodeterioration was defined by Hueck (1965) as *"any undesirable change in the properties of a material caused by the vital activities of living organisms"* [9]. It can be seen as a complex ecological process, driven by interactions among microorganisms, substrate and environmental factors (water, light, temperature, etc.)[10].

Biodeterioration of stone materials can be described as a sequence of different phases (Fig. 1): the first step is the formation and growth of complex biofilms, containing different communities of microorganisms, each of them with specific heterogeneous metabolic activities. Under favourable environmental conditions, the initial adhesion of microorganisms to the surface starts and microcolonies are generated by cell division. Once the population size has reached a threshold value, cell-to-cell communication triggers the formation of the mature biofilm. Biofilm bacteria produce large amounts of exopolymers (EPS), consisting mainly of polysaccharides, pigments, lipids, and proteins. The EPS plays a variety of functions, including protection of the microorganisms from desiccation, erosion, antibiotics, and disinfectants; they also act as nutrients and energy storage [11-12]. During biofilm development, a complex 3D structure grows on the stone surface. In addition, the physico-chemical environment is heterogeneous within a biofilm, due to gradients of pH, redox potential and ionic strength [13]. Availability of oxygen, access to light and / or nutrients vary through the biofilm, as a consequence, each microorganism has to adapt to a particular microenvironment, depending on its location in the biofilm. Thus, there is a huge heterogeneity in cellular activity within the biofilm [14-15]. At this stage, the biomass forms a surface network of filaments, where heterotrophic microorganisms can grow by decomposing the organic material produced by primary cells: this eventually starts off the growth of a more complex microbial community. The slimy surfaces of this biofilm favour the trapping of environmental particles (pollen, spores, and abiotic particles). These combined into the biofilm layer with components derived from the mineral surface and cellular debris, produce complex crusts and patinas. Moreover, EPS cause mechanical stresses to the mineral structure, due to shrinking and swelling cycles of the colloidal biogenic slimes inside the stone pore. This can lead to the alteration of pore size and distribution, and in particular to the broadening of pores after

penetration of hyphae and filaments, with consequent loosening of stone particles from the parent rock material. The latter alteration is particularly frequent in granitic rocks.

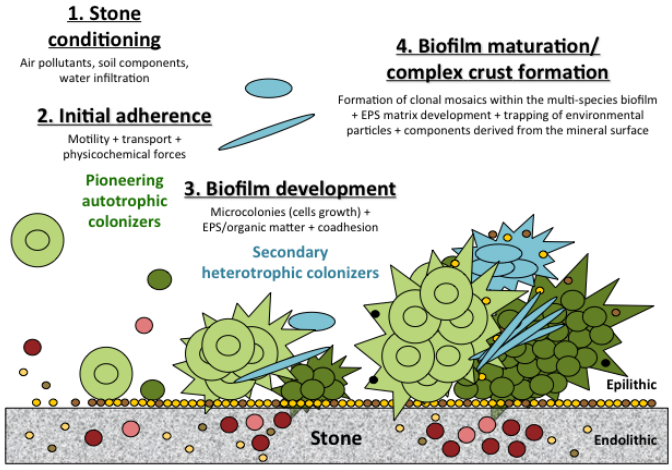

Fig. 1 Steps of the development of multispecies biofilms on stone. Yellow, brown and dark small circles: organic and inorganic molecules and ions. Single and double green circles: pioneering autotrophic colonizers, i.e. cyanobacteria and algae, respectively. Blue cells: secondary heterotrophic colonizers, i.e. bacteria and fungi [14].

The quantification and characterization of the biomass colonizing stone are essential prerequisites to implement appropriate control strategies and treatments.

Depending on the situation (climate, type of stone *etc.*) and on the type of microorganisms, the microbial colonization of stone monuments can result in different kinds of deterioration of buildings [16-17]. In Table I the colonization temporal trends of the principal microorganisms, their activities, and consequent damage of stone materials are summarized.

Table I Microbial activities involved in deterioration of stone material.

Temporal trend		**Microrganism**	**Microbial activity**	**Damage caused**
Colonization temporal trend	**Pioneering colonization**	Microalgae Cyanobacteria	Surface growth	Discoloration, water retention
	Secondary colonization	Lichens Fungi	Acid production	Corrosion, erosion
			Hydrolytic enzymes	Increased fragility, erosion
			Chelation	Corrosion, etching
			H_2S production	Corrosion
			Growth of microbial filaments	Physical damage to surface, increase in permeability
	Growth of a more complex microbial community	Microalgae Cyanobacteria Lichens Fungi	Inhomogeneous growth/activity	Corrosion due to concentration cells
			Metabolic activity	Blistering, embrittlement

During the processes of biodeterioration, stone materials are used by the micro-organisms both as nutrients (as in the case of heterotrophic organisms, e.g. bacteria, and fungi) or simply as a physical support for their growth (this is the case of autotrophic organisms, namely algae and cyanobacteria) [18-22].

Phototrophic microorganisms[1] cause not only aesthetic damage to stones, but also structural ones, as in moderate climates they fed on pollution from anthropogenic sources and excrete corrosive acids and compounds [23]. In particular, algae cause dissolution of marble and limestone, by excreting organic acids: oxalic, citric, gluconic, fumaric, malic, formic, etc. [24]. Thus, microbial contamination acts as a precursor of the formation of detrimental crusts on rock surfaces caused by acidolytic and oxidoreductive (bio-)erosion of the mineral structure. These epilithic and endolithic[2] organisms can potentially contribute to the breakdown of rock crystalline structures such as sandstone, granite, gneiss, limestone, dolomite, basalt, bricks, or even glazes [16-17; 25]. Finally, the breathing of microorganisms induces corrosion of the mineral matrix, such as $CaCO_3$ in limestone and mortars, since released CO_2 reacts with water and forms carbonic acid (H_2CO_3) [26-28].

[1] Phototrophs are the organisms that carry out photon capture to acquire energy, such as microalgae and cyanobacteria.

[2] The microorganisms colonizing the stone monument surface are divers. They can be distinguished according to their location on or in the stone. The microbial colonizers are called epilithic when they are located on top of the rock. Microorganisms living inside the rock within cracks and fractures, or in the pore space of sandstone or granites are termed endolithic.

1.2 Protection of stone from biodeterioration: common approaches

As already said, the protection of outdoor stone monuments from microbial deterioration is a difficult issue, due to the ubiquitous distribution and variety of microorganisms. The control of biodeterioration is principally based on the biological patina removal and inhibition or delay of new colonisations.

In restoration practice, the removal of patinas, crusts and vegetation is the first step of any conservation and restoration campaign [29].

The elimination of biological growth is usually based on three approaches: a) mechanical removal, b) physical eradication, c) use of biocides.

Cleaning using brushing, scalpels, sand blasting, air abrasive, low-pressure washing, vacuuming, and ultrasounds are classified as mechanical approaches for the treatment of the microbial growth. Differently, the physical eradication of microorganisms is carried out applying methods such as electromagnetic wavelengths, high temperatures and laser [29].

The biodeteriogens, the material of the artifact and its conservation state drive the choice of the cleaning method, nevertheless the application of chemicals (biocides) is the most widely used antifouling approach.

1.2.1 Biocide approach: definition and characteristics

A biocide is defined in the European legislation as a chemical substance or microorganism intended to destroy, deter, render harmless, or exert a controlling effect on any harmful organism. The US Environmental Protection Agency (EPA) uses a slightly different definition for biocides as "*a diverse group of poisonous substances including preservatives, insecticides, disinfectants, and pesticides used for the control of organisms that are harmful to human or animal health or that cause damage to natural or manufactured products*"[30].

The Biocidal Products Regulation (BPR, Regulation (EU) 528/2012) classifies the biocidal products into 22 different product types (PT), sometimes splitted in multiple subgroups. The biocides for protection of cultural heritage belong to the preservatives main group and are classified as product-type 10, namely masonry preservatives [31].

Biocides are toxic chemicals that can affect both macro- or micro-flora responsible for biodeterioration. Biocidal products contain one or more biocidal active substances and may contain other non-active co-formulants that generally improve the performance as well as the desired pH, viscosity, colour, odour, etc. of the final product [32].

Biocides act on organisms interacting with cells in three regions: the cell wall, the cytoplasmic membrane, and the cytoplasm. Extracellular material, cell morphology, and cellular chemical composition affect the access of biocides to these regions. The mechanisms of interaction between biocides and cells depend on the chemical diversity of the biocides, although the final damaging outcomes may show considerable similarity.

The type of damage produced by the biocide on the microbial cells determines its final effect that is called “microbiostatic” or “microbiocidal”. Microbiostatic agents react reversibly with cell

components such as nucleic acids and proteins, whilst microbicidal compounds cause irreversible damage which leads to lyses of the cells or to coagulation of the cytoplasm [33]. However, the inhibitory or biocidal effect of the compound is determined not only by its chemical nature, but also by its concentration. A biocide may be inhibitory at low and biocidal at high concentrations respectively, and thus it is extremely important to tune the dose [33].
According to their mechanism of action, the biocides can be classified as:

1) Membrane-active

   The membrane-active biocides, positively charged, interact with the cell wall and/or the outer membrane, attracted by the negatively charged surface. Ionic interaction with phospholipids of the cell wall leads to their partial adsorption. This process causes loss of the permeability barrier function and modifies the membrane potential and electron transport chain. The leakage of metabolites (such as K^+ ions and inorganic phosphate), the lysis of the cell, and the disappearance of membrane enzymes are among the reported impacts of quaternary ammonium salts (QACs) on bacteria. Membrane-active microbiocides such as QACs are governed in their interactions with cells by the balance between their hydrophobic and polar groups. Membrane-active microbicides include quaternary ammonium salts, alcohols, phenols, salicylanilides, carbanilides, dibenzamidines [29,34].

2) Electrophilic active

   The greatest number of microbiocides in use today belongs to the group of electrophilic active compounds whose molecule is characterized by the presence of a carbonyl group. The reactivity of these compounds depends on their low steric hindrance and strong electron withdrawing capability. In fact, the electron deficiency at the carbonyl carbon atom enables these substances to react with nucleophilic cell components.
   This kind of microbicides includes aldehydes, compounds with activate halogen atoms (chlorine, bromine, iodine), compounds with an activated N–S bond. Most of them have the disadvantage of a slow microbicidal effect [29,34].

3) Agents with oxidizing activity

   The oxidizing agents (hydrogen peroxide and chlorine- containing compounds) have a microbiocide effect due to their strong oxidizing power, their strong affinity to electrons that is also directed toward organic matter including microorganisms. The effect is not selective and covers bacteria, algae, yeasts, fungi, but also spores. They have an intrinsic limited chemical stability. A drawback is that high reactivity and low persistence can leave some microorganisms unharmed, especially those that proliferate in biofilms [29,34].

4) Chelate formers

The antimicrobial activity of chelate formers is partly due to their ability to compete for the complexion of metal cations necessary for the functional cell metabolism. They include azoles and the dithiocarbamates [29,34].

Due to the wide range of materials used in the cultural heritage buildings and to the different types of microorganisms involved in their deterioration, the availability of a large range of biocides is needed.

Biocides must be carefully selected for appropriate activity and handled with care, according to safety regulations. For cultural heritage conservation, the most important parameters in choosing a valid biocide are the bioselectivity, the compatibility with the materials, the capability of providing protection over the required time scale and a good low cost/benefit ratio.
Biocide manufacturers have to meet the following additional requirements: 1) long shelf-life,
2) low ecotoxicity, 3) biodegradability. The last two have become increasingly important recently, as governments have become more concerned with environmental problems arising from the unregulated disposal of biocides.
Many factors can affect the performance of biocides on outdoor stone artifacts. They vary with the composition of the biocide, the method of application, the properties of the surface, the physical–chemical properties of the substrate and the degree of exposure of the surface to rain.
Other factors affecting biocides' performance are contact time, interfering substances, temperature, and concentration [35].
This thesis explores aspects related to the use of biocides, such as the method of application and the durability of the antifouling treatments, the problems linked to the interaction between the biocides and the substrate, the toxicity for the operator and for the environment.

1.3.1 Methods of application and durability

The chemicals commonly used are in form of liquids, emulsion formulations, and dispersible powders. Depending on the form, biocides can be applied in various modalities: as an aerosol or as a poultice, by brushing, by injection or immersion, or by spray. In alternative they can be inlaid into a "vehicle" which will fix it to the surface (e.g. in a coating). The application methods must also be carefully chosen in function of the biodeterioration, the climatic condition, the conservative state of the substrate. Moreover the treatment must be effective and long lasting, in order to be cost effective, and it must be sufficiently diluted in order not to harm the environment, when leached by rain. Many biocides are short-lived or degradable through abiotic and biotic processes, while others may transform into more toxic or persistent compounds. Many biocides are only effective for a short period of time (6 months–1 year), making frequent re-application necessary [36].

1.3.2 Material compatibility and possible interferences

The biocides should not induce any chemico–physical variations in the substrate, especially where frequent re-applications are likely. Since it is possible that other chemical treatments have been applied to the same stone over time, the biocides should not interact with products used for cleaning, or with consolidants and protective coatings [33]. It is important to known the exact composition of the biocides, in order to avoid those containing compounds which interact with stone minerals, determining changes of the porosity and permeability of the material, thus affecting durability of the material itself [37-38]. The potential interference with the substrate can be checked by the localized application and using low doses [39]. Some biocides (now obsolete), such as aggressive and strongly oxidizing chemicals (e.g. hydrogen peroxide), can oxidize metal ions (e.g. iron), leading to corrosion of minerals and causing rust or black stains, even if often stabilized by the addition of acids. In a similar way, chlorine-containing compounds are now avoided in this field, due to their not negligible interactions with stone materials [40].
The evaluation of all the possible interferences implies the analysis of the following parameters before and after treatment: dry weight, colour, water absorption by capillarity, calcium ion concentration, and surface micromorphology observed under optical and scanning electron microscopes [41-43].

1.3.3 Toxicity

A substantial part of all biocidal products currently available on the market act through toxic mechanisms exhibiting numerous pharmacological activities toward a number of specific cellular targets, including damaging or inhibiting the synthesis of cell walls, and affecting DNA or RNA, proteins or metabolic pathways. For these reasons, commercial and traditional biocides may be dangerous for human health and the environment, although they have different toxicological profiles, as indicated by EU reference databases.
Several biocides that were widely used in the past, such as the organo-metallic compounds (e.g., tributyltin oxide (TBTO)) and the phenolic derivates (e.g. dichlorophen, pentachlorophenol and sodium pentachlorophenate), turned out to be dangerous for their acute toxicity, their suspect teratogenicactivity or their environmental risk, and thus withdrawn from the market [44].

What has been said so far implies the necessity of environmentally-friendly innovative approaches that overcome the limitations associated with the biocides actually used. This goal can be achieved by proposing adequate alternative materials, products and methods of intervention instead of the traditional ones.

Consequently, considerable studies have been made to implement and evaluate alternative environment-friendly biocides [45-46]. Recent findings suggest potential natural sources for the control of biological growth on stones [45], and several natural substances with antimicrobial action have been identified and extracted from a very wide range of sources, including plants,

microorganisms and animals [46]. Among these we focus on Lichen secondary metabolites (LSM) and Natural Products Antifouling (NPAs).

Lichen are known to produce enormous amounts of chemically diverse group of relatively low molecular weight secondary metabolites, ranging from aliphatic compounds like caperatic acid to aromatic like lobaric acid [47]. LSM are a group of more than 800 compounds, in part exclusively synthesized by lichen forming fungi, which include aliphatic, cycloaliphatic, aromatic and terpenic components [48-49]. Many LSM show antibiotic, antiviral and anti-proliferative functions, suggesting their potential use for therapeutic applications [50]. The antimicrobial activity of LSM has been assessed against a wide set of bacteria and filamentous fungi, mainly of medical interest [51-52] or plant pathogens [53], but researches overlooked their effects against rock-dwelling organisms, thus preventing the evaluation of their potential use for the control of the biological colonization on stone materials.

The NPAs are advantageous over conventional toxic biocides in that they are less toxic, effective at low concentrations, biodegradable, have a broad spectrum antifouling activity [54-57]. In general, the search for NPAs is greatly encouraged as they act as repellents more than as strong toxic agents. Natural antifoulants are common and include toxins, anaesthetics, surface-active agents, attachment and/or metamorphosis inhibitors and repellents [58-60]. These are produced by, many marine organisms, in the form of highly water soluble secondary metabolites, preventing adhesion of microorganisms on their surface.

The majority of NPAs identified so far are terpenoids, steroids, carotenoids, phenolics, furanones, alkaloids, peptides and lactones. They have been isolated from a wide range of organisms, mainly sponges and soft corals, known for maintaining foul-free surfaces. Other groups include seaweeds, seagrasses, and microorganisms. Summing up, to date about 145 NPAs have been isolated and identified from marine organisms, as reported in the graph below (Fig. 2).

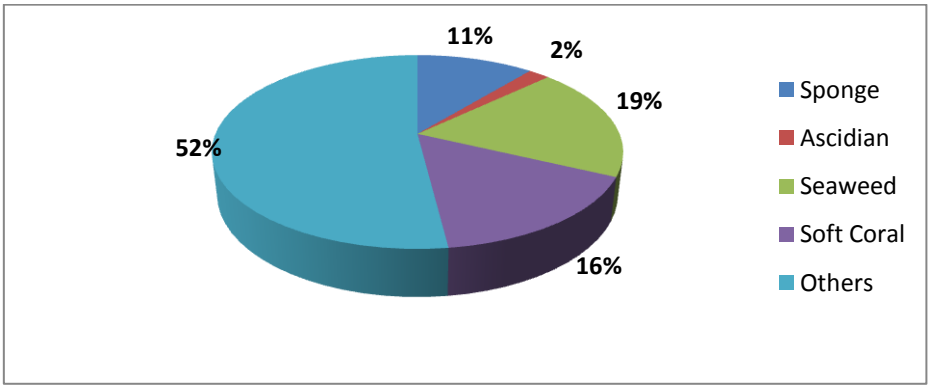

Fig.2 NPAs isolated from marine sources

In this thesis, two environmentally-friendly compounds belonging to the class of lichen secondary metabolites (LSM) and to that of Natural Products Antifouling (NPAs) have been selected and used in the synthesis of the nanoparticles: namely, usnic acid (UA) and zosteric acid sodium salt (ZS), respectively.

1.4 Multifunctional coatings: the encapsulation of the biocides

All the biocides, environmentally-friendly or not, if directly applied on the stone surface, are easily washed away. In order to develop an antifouling treatment with a higher efficacy over time, this thesis proposes the realization of an innovative coating with antifouling properties [61].

Coatings are mainly applied on surfaces for decorative, protective, or functional purposes. The term "functional coatings" describes systems which possess, besides the classical properties of a coating (i.e., decoration and protection), an additional functionality [62].

Self-cleaning [63], easy-to clean (anti-graffiti) [64], antifouling [65], antibacterial [66-67] coatings are becoming increasingly important in different sectors [68].

Antifouling and antimicrobial coatings are probably the most widespread examples of functional or smart coatings. Most antifouling coatings are prepared by dispersion of biocides molecules in the wet coating material [69-70]. This practice suffers from some drawbacks, such as poor control of the release rate of the antifoulants or degradation of the active substance. Indeed most biocides are small molecules diffusing very fast through the coating matrix, which quickly release the active compound and lose its antifouling function before the end of its intended life time.

On the other hand, increasing the amount of biocides in the coating in order to extend its function in time is not economically, environmentally and practically sustainable. Moreover, the use of high concentrations of biocides in the formulation may result in a macroscopic phase separation of the film [71].

Since the effectiveness and efficiency of several biocides lasts only for a short period of time (between 6 months and one year), frequent treatments or many application cycles are usually needed [72]. Thus improving the performance of the antifouling coating is necessary from economic and environmental point of views.

In this thesis, the encapsulation of the biocides in "reservoirs" is attempted in order to reduce the amount of bioactive compounds while preserving a satisfactory long-lasting antifouling action. In practice the biocides are confined into capsules or core–shell particles, precluding direct contact with the adjacent environment [73].

The release rate of the active compounds from the coating is controlled by the slow release from the capsules to the surrounding coating matrix; at the same time the encapsulated biocide is protected from degradation and washout.

The term "capsules" covers a broad range of colloidal particles of different sizes, morphologies and chemical compositions (see Fig. 3). Submicron capsules are typically referred to as nanocapsules. Likewise, the encapsulation is typically termed nanoencapsulation for nanocapsules whereas microencapsulation usually refers to microcapsules.

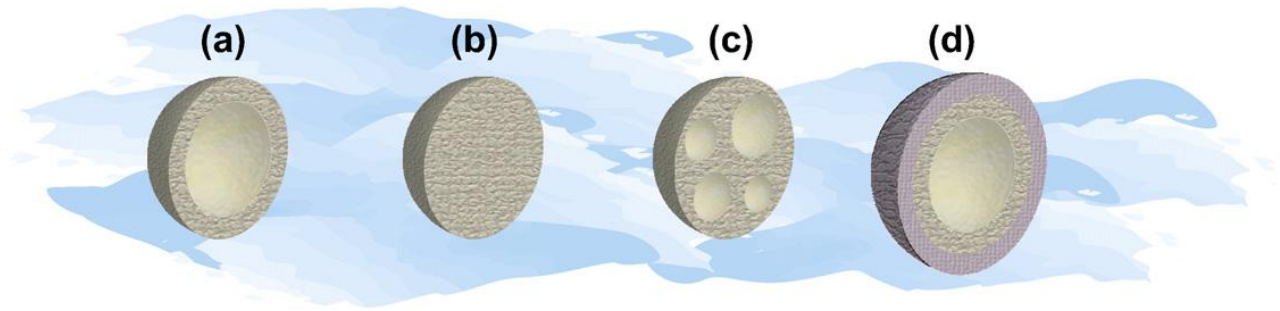

Fig.3 Capsule morphologies; a) core–shell, b) microsphere (monolithic/matrix), c) multicore–shell and d) core–multishell.

There are numerous methods available to encapsulate biocides. The choice of encapsulation method depends on the intended release profile and on the physico-chemical properties of the biocide (polarity, size, charge, surface activity, etc). In general, encapsulation techniques are divided into two basic groups, namely chemical and physical, with the latter being further subdivided into physico-chemical and physico-mechanical techniques [68]. Some of the important processes used for microencapsulation are summarized in Table II.

Table II Different techniques used for microencapsulation [68].

Chemical processes	**Physical and physico-chemical processes**	**Physico-mechanical**
Suspension	Coacervation	Spray-drying
Polycondensation	*Sol-gel encapsulation*	Multiple nozzle spraying
Dispersion	Layer-by-Layer (L-B-L) assembly	Fluid-bed coating
Miniemulsion polymerization	Supercritical CO_2-assisted microencapsulation	Centrifugal techniques
		Vacuum encapsulation
		Elactrostatic encapsulation

In this contest, the miniemulsion polymerization and the sol-gel techniques will be detailed, because the combination of these two methods was applied for synthesis of the silica nanocontainers studied in this thesis project. Special emphasis is attributed to the sol-gel method that was also applied for the development of a multifunctional coating.

The miniemulsion polymerization is largely used for the synthesis of nanocontainers due to unique properties, such as ultralow interfacial tension, large interfacial area, thermodynamic stability and the ability to solubilise otherwise immiscible liquids. It promises to be one of the versatile preparation methods enabling to control the particle size, morphology, homogeneity and textural properties [74-75].

The miniemulsion are originated by the combination of four components: i) non-polar phase (usually oil), ii) ionic surfactants, iii) co-surfactants (generally 4–10 carbon chain aliphatic alcohol) and iv) an aqueous phase.

The surfactant and cosurfactant, when properly selected, forms a mixed film at the oil/water (O/W) interface, resulting in an interfacial pressure exceeding the initial positive interfacial tension.

On a microscopic level, the surfactant molecules form an interfacial film separating the polar and the non-polar domains. This interfacial layer forms different nanostructures, ranging from droplets of oil dispersed in a continuous water phase (O/W-miniemulsion or direct miniemulsion) over a bicontinuous ''sponge'' phase to water droplets dispersed in a continuous oil phase (W/O miniemulsion or inverse miniemulsion). The type and amount of surfactant and cosurfactant, the concentration of precursor solution, the kind of oil phase, and the water-to-oil ratio affect the stability of an emulsion and further affect the morphology and size distribution of the produced particles.

In particular, the surfactant molecules are amphiphilic with a long hydrocarbon tail and a relatively small ionic or polar head group. Amphiphiles can be ionic (cationic, anionic), zwitterionic, or non-ionic depending on the nature of their head groups. Cetyltrimethylammonium bromide (CTAB), sodium dodecyl sulfate (SDS), sodium 1,4-bis (2-ethylhexyl)-p-sulfosuccinate (DOSS) or poly(ethylene glycol) (PEG)ethers represent some of the most widely applied surfactants [76] (see Fig.4).

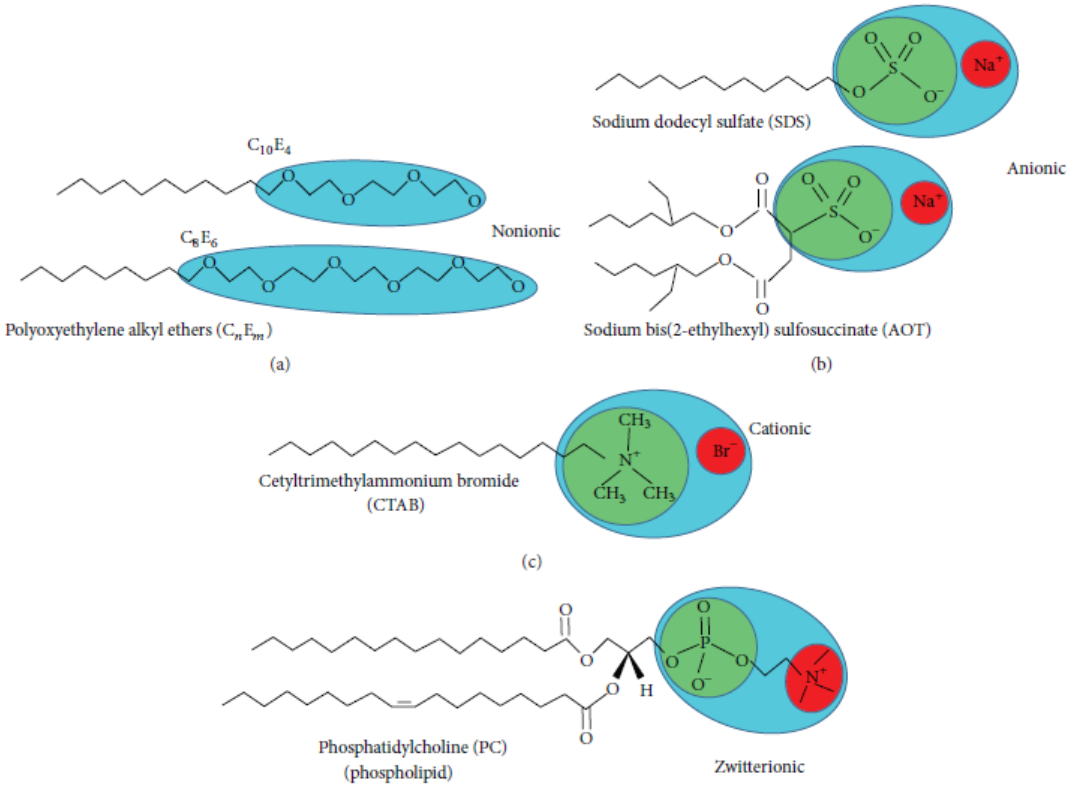

*Fig.*4 *Example of most common non-ionic (a), anionic (b), cationic (c), and zwitterionic (d) amphiphilic molecule*[77].

For storage and controlled delivery applications, silica mesoporous materials are usually preferred, being inert and non-toxic [78-79]. Usually, silica nanoparticles, produced by sol-gel method, are used to load active compounds through either a physical adsorption procedure or a physico-chemical interaction after the funtionalization of the surface. The physical adsorption procedure

involves the use of silica nanoparticles as scaffolds where the active compound is adsorbed. This method is relatively simple and allows loading of nanoparticles with different types of biocides depending on the solvent; nevertheless it has an intrinsic drawback, due to the fast and easy leakage of biocides from the scaffold surface [80-81]. In the physico-chemical procedure, instead, the silica surface is functionalized in order to promote chemical bonds with the biocides. Functional groups, targeting ligands and stimuli-sensitive molecules can be conjugated to the internal pores and the outer surface of nanoparticles [82-83]: this procedure allows longer release times, but the synthesis is much more complex, time consuming, and more importantly strictly specific of each selected class of biocides.
In order to overcome the limits of the physical adsorption procedure and the synthetic difficulties of the functionalised surface, this thesis presents a procedure for encapsulation of the biocide into silica nanocapsules and the entrapment of the biocide into silica mesoporous nanoparticles, directly during the synthesis of the two nano containers.

Silica inorganic nanoparticles can be obtained by polymerization of different precursors, trough sol-gel processes, taking place at the miniemulsion interface. Sol–gel template synthesis is the prevailing method for producing mesoporous silica nanoparticles (MSNs) [84-85]. It consists in the hydrolysis and polycondensation of organosilanes in aqueous or water–alcohol media in the presence of surfactant micelles as organic templates. Typically CTAB is used as template agent and an alkoxide such as tetraethylorthosilicate (TEOS) is used as silica source. Under the alkaline conditions, TEOS undergoes hydrolysis followed by condensation into silica (see Table III).

Table III Hydrolysis and condensation of alkoxides with general formula: M (OR)n, where M = element with valence n and R = alkoxide group

Gel formation	
Hydrolysis	$M(OR)_n + H_2O \rightleftarrows M(OR)_{n-1}(OH) + ROH$
Condensation	$M{-}OH + M{-}OX \rightleftarrows M{-}O{-}M + X{-}OH$ con X=H o R

The transition from sol to gel involves two key steps, such as hydrolysis and polycondensation reactions. The hydrolysis takes place also by small amounts of water. Since water and alkoxides are immiscible, a mutual solvent, such as alcohol, is normally used as homogenizing agent.
In the hydrolysis reaction, the alkoxide groups (OR) are replaced stepwise by hydroxyl groups (OH):

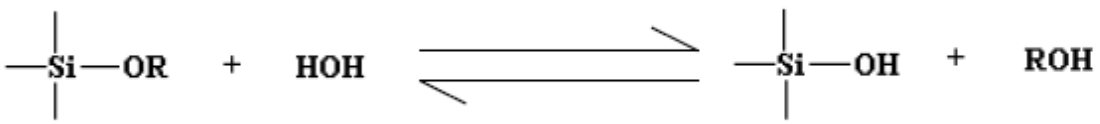

Simultaneously to the hydrolysis, the polycondensation reactions occur:

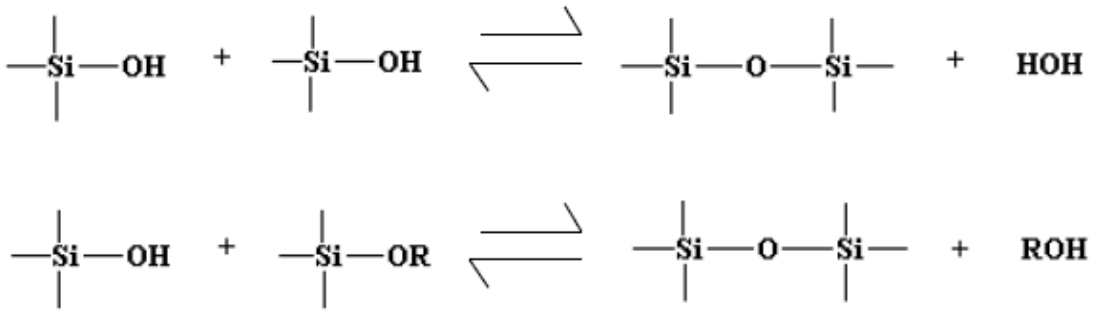

The polycondensation reactions involve hydroxyl groups and result in M-O-M' linkages which, in turn, yield a three dimensional network, the gel, upon a polymeric weight and cross-linking degree increase. The gel state is then best described as a viscoelastic material composed of interpenetrating solid and liquid phases [86].

The hydrolysis and condensation reactions are catalysed by acids and bases. The choice of the catalyst and therefore of the pH of the reaction environment determines the type of siliceous particles, conditioning the encapsulation properties (Table IV). Its structure is strongly dependent on the water content in the system and on the catalysis nature. In acidic solution or for low water concentration, weakly crosslinked linear chains are produced, resulting in a soft gel, which can be readily redispersed in solution. On the other hand, in based-catalyzed solutions, branched clusters are preferentially formed and their tendency to coalesce is responsible of the solution gelation [87-88].

Table IV Characteristics of the sol-gel process depending on the type of catalyst

Acid catalysis	**Basic catalysis**
Fast hydrolysis	Slow hydrolysis
Reversible and incomplete hydrolysis (re-esterification)	Absolute and complete hydrolysis
Condensation proceeds by reaction of neutral species with protonated Si-OH groups	Condensation proceeds by addition of monomers to the Si-O- groups of the cluster
Low branching chains	Spherical particles and strongly reticulated structures

During the condensation process, the anionic soluble silica, which can be regarded as an anionic polyelectrolyte, organizes around the template, i.e. the surfactant aggregate. This aggregate may be hexagonal, bicontinuous cubic, lamellar, etc. depending on the choice of surfactant and the molar ratio, as reported in Fig.5.

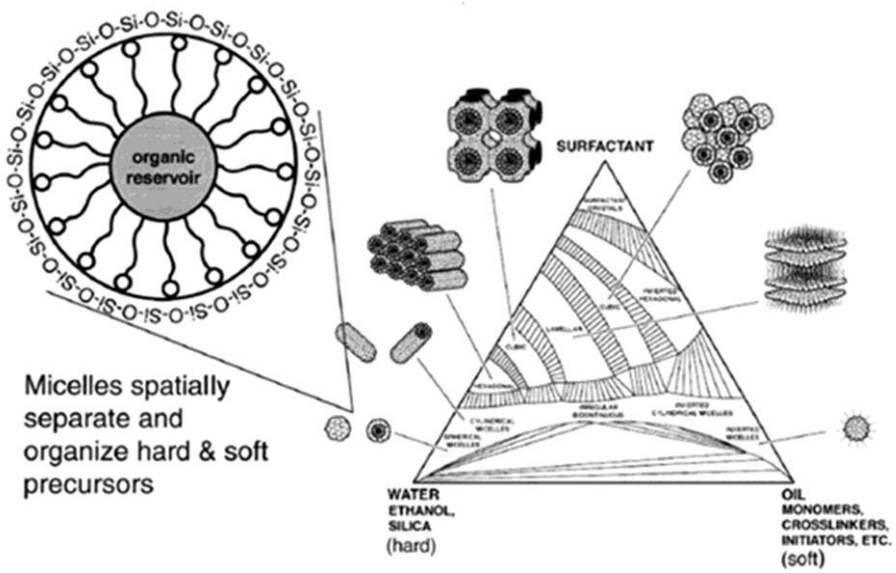

Fig.5 Schematic surfactant ±oil ±water phase diagram. With the introduction of hydrophobic organic (or generally soft) precursors and hydrophilic inorganic (or generally hard) precursors, organic constituents' partition within the hydrophobic micellar interiors, while inorganic constituents are organized around the micellar exteriors [86].

The wet material, obtained by the alkoxide hydrolysis and polycondensation reactions, is not the end product. In fact, it is necessary a drying stage in order to obtain the final product, with the required characteristics. In this phase, the desorption of water and residual alcohol physically linked to the polymeric network evaporate with a time rate that depends on the environmental conditions [89-90].

The synthesis often yields materials with extreme control of the pore diameter, which theoretically doubles the length of the hydrocarbon tail of the cationic surfactant used as the template the pore size can also be manipulated by addition of a cosolvent that swells the surfactant aggregate and plays the role of cosolvent and template (droplets) [91]. If the cosolvent is a high boiling compound (i.e. kerosene, hexane, and trimethylbenzene), it is necessary to remove the compounds through either calcinations or washing with organic solvents [92].

In the present thesis, we have successfully fabricated two novel silica nanocontainers: the first one employs low boiling point ethyl ether as cosolvent and template and the second one is obtained without cosolvent.

The sol-gel process has been widely studied and applied for the production not only of the silica nanocontainers, but also for the realization of different kind of coatings [93].

The sol-gel offers a better control of the chemical composition, excellent homogeneity, low process temperature, uniformity over large area allowing to produce high-quality films up to micron thickness [94-95].

In cultural heritage fields, sol-gel TEOS- based coatings have been commonly used in the consolidation of decaying stone heritages. These products polymerize with the porous structure of the decaying materials, significantly increasing the cohesion of the materials. Thus, ideally, an amorphous SiO_2 gel reconnects the binder between the mineral grains lost during the decaying

processes. The result is often accompanied by an appreciable increase in the strength of the stone [96].

Nevertheless, these consolidants crack during the drying phase due to the developed capillary force. Cracking occurs as a result of intrinsic stresses caused by the existence of a meniscus at the liquid-vapor interface, which generates a differential capillary pressure within the gel. This makes the network shrink until it becomes stiff enough to withstand the stress imposed by capillary pressure [97-98]. This brittle gel fragments create a secondary capillary network in the stone, which may accelerate the rate of deterioration by increasing water uptake or by detaching crumbly fragments on decayed stones.

Recently it has been shown that this critical drawback can be overcome by addition to the sol surfactants or other inorganic compounds. These act as a template to obtain large pores once the rigid mineral framework is formed and thus reduce the capillary stresses (inversely proportional to the pore size) generated during drying [99-101].

Moreover the elastic properties of the gels can be modified by addition of flexible linear segments of polydimethylsiloxane (PDMS) to the sol. This introduces elastic “bridges” into the silica gel, increasing flexibility and strength of the coating and accelerating the gelation process. Incidentally, addition PDMS to the silicon alkoxide does not increase the viscosity of the initial sol, and accelerates the gelling process, avoiding gel fracture during the drying stage, due to the formation of a more uniform size distribution of mesopores [101-102].

Commonly, TEOS-based commercial products are applied on silicate materials (e.g. bricks) because of the lack of mineral interfacial bonding when used on stones with relatively high contents of calcite and/or with some clay.

The limited effectiveness as consolidant on pure carbonate stone (i.e. marble, travertine) is due to the poor chemical affinity between carbonate salt and alkoxysilanes. Carbonate salts do not have active-OH groups on the surface available for interaction with TEOS and no chemical bonds between the stone materials and the TEOS-based consolidant are formed. N-octylamine, a non ionic surfactant, opportunely added in the consolidant formulation, increases the interaction between a non-siliceous stone and these kinds of siloxane products [103-105].

In the light of what has been said so far, this thesis reports the synthesis and test of a hybrid silica coating with the addition of two different kinds of nanoparticles. The nanoparticles have been selected in order to give self-cleaning and antifouling properties to the final coating. For this reason the addition of commercial TiO_2 nanoparticles and SiO_2 nanocontainers will be explored.

Chapter 2

Materials and methods

2.1 Selected biocides

2-mercaptobenzothiazole (MBT)

The 2-mercaptobenzothiazole (MBT) is a bicyclic heteroatomic molecule, widely used as preservative and biocide and commonly employed as a copper corrosion inhibitor. The MBT is an organosulfur compound and the molecule consists of a benzene ring fused to a 2-mercaptothiazole ring, which includes an endocyclic and an exocyclic S atom and an endocyclic N atom. It exists in two tautomeric forms, namely thiol (I) and thione (II), and according to the literature, the thione form is the prevailing specie (see Table V).

Table V Molecular structure of 2-mercaptobenzothiazole and properties

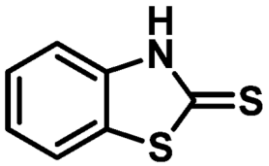 Thiol form	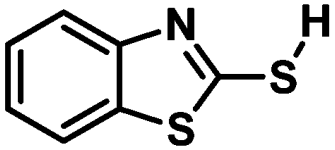 Thion form	Chemical formula	$C_7H_5NS_2$
		Molar mass	167.24 g mol-1
		Melting point	177-181 °C

MBT is used in cultural heritage restoration, because it is effective against a broad spectrum of microorganisms, except fungi. Its efficacy depends on the coordination capability that inhibits the binding of N/O/S donor groups of biological macromolecules [106].

Usnic acid (UA)

Usnic acid (UA) is a lichen secondary metabolite (LMS) compound and presents as a yellowish pigment in the lichens cortical layer. Usnic acid has been identified in many genera of lichens including *Usnea, Cladonia, Lecanora, Ramalina, Evernia, Parmelia and Alectoria*. Since its first isolation in 1844, usnic acid has become the most extensively studied lichen metabolite and one of the few commercially available [107].

Usnic acid exhibits several biological and pharmacological properties such as anti-microbial activity against human and plant pathogens, anti-viral, anti-proloferative, anti-inflammatory and analgesic activity. Nevertheless, the practical use of usnic acid in therapy has been rather limited due to its poor solubility in water.

Usnic acid (UA) is a low-molecular weight dibenzofuran derivative (2,6- diacetyl-7,9-dihydroxy-8,9b-dimethyl-1,3[2H,9bH]-dibenzo-furandione), which occurs in two enantiomeric forms differing in the orientation of the methyl group located in the stereogenic centre at the 9b position (see

Table VI) [108-109]. The lipophilic nature of this molecule is deeply linked with its cytotoxic effect: indeed the triketone present in the molecule and the intra molecular hydrogen bonds contribute to the biocidal properties.

Table VI Molecular structure of (+) usnic acid

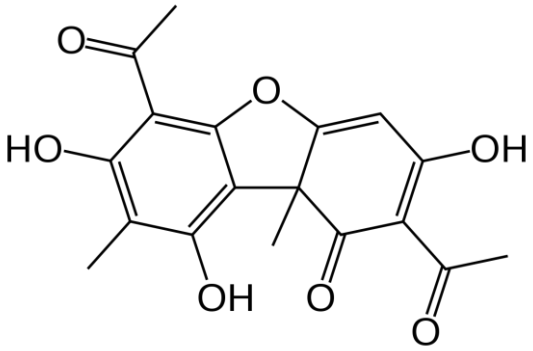	Chemical formula	$C_{18}H_{16}O_7$
	Molar mass	344,315 g mol^{-1}
	Melting point	204 °C

Zosteric acid sodium salt (ZS)

Zosteric acid (ZA), or p-(sulfoxy) cinnamic acid (Table VII), is a natural antifouling product, first extracted from eelgrass *Zostera marina*. In order to protect itself the seagrass *Zostera marina* produces and continuously releases complex mixtures of water soluble compounds (among these zosteric acid is one of the most abundant), which prevent biofouling by deterring colonization of bacteria, yeast, fungi, algae and bivalves on solid surfaces or plant leafs [110]. Application of zosteric acid as a natural anti-adhesive agent may replace other chemical treatments in agriculture, medicine and industrial activities. The antifouling capability of the zosteric acid and its sodium salt is attributed to the sulfate group present in these compounds. These antifoulants binds on the cell surfaces at non-toxic concentrations, inhibiting the adhesion of microorganisms and successive formation of biofilm [111].

Table VII Molecular structure of zosteric acid and properties

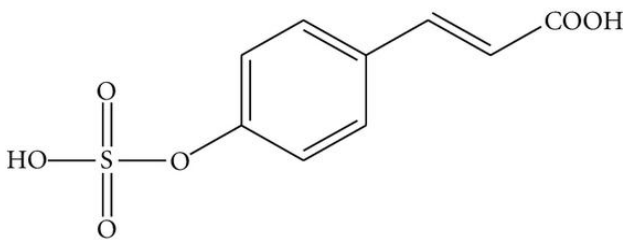	Chemical formula	$C_9H_8O_6S$
	Molar mass	244,22 g mol^{-1}
	Melting point	210-220 °C

2.2 Synthesis of silica nanocapsules loaded with three different biocides

Although empty silica nanocontainers have been synthesized and characterized before starting the synthesis of the active compounds, only the protocol for the synthesis of the loaded ones is reported here, as the two protocols differ only for the addition of the biocide.

Silica nanocapsules (Si-NC) loaded with the three selected biocides, were prepared by one-step self-assembly method, involving TEOS polymerization assisted by a cationic surfactant (CTAB).

This sol-gel synthesis procedure is showed in the flow-chart reported in Fig. 6.

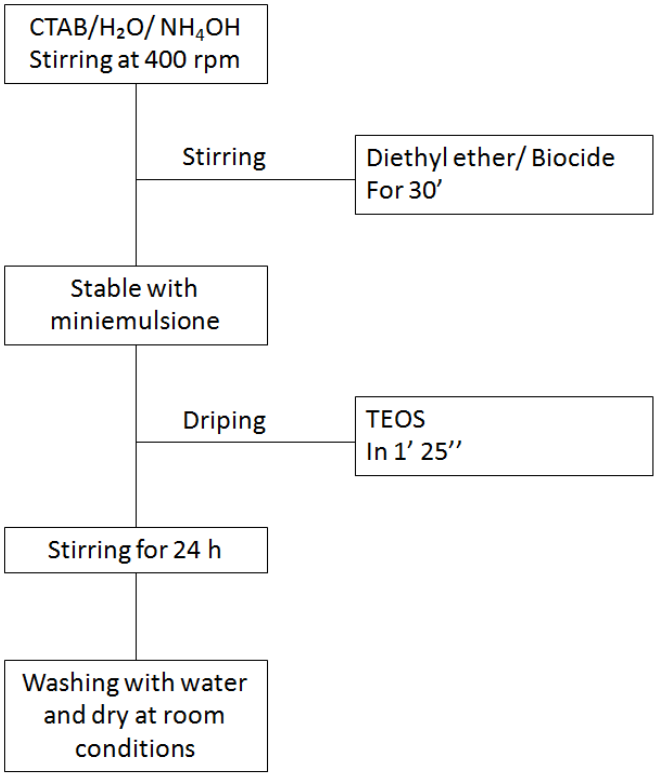

Fig.6 Flow-chart of the silica nanocapsules synthesis procedure

We have used cetyltrimethylammonium bromide (CTAB, Aldrich), ammonia solution (NH_3aq 30%, Aldrich), tetraethoxysilane (TEOS, Aldrich) and ethyl ether (Et_2O, Aldrich) for the preparation of the nanocapsules. These have been loaded with:

i) 2-mercaptobenzothiazole (Aldrich);
ii) Usnic acid (Aldrich);
iii) Zosteric acid sodium salt, was synthesized from trans-4-hydroxycinnamic and the sulphur trioxide pyridine complex in the laboratory of CNR-ICMATE (Padua, Italy).

According to a typical synthesis procedure of silica nanocapsules (Si-NC) [112], CTAB (0.25 g) is dissolved in deionised water (35 mL) and stirred (150 rpm) at 55°C for 15 min. After complete

dissolution of CTAB, 0.25 mL of ammonia aqueous solution (25–28% V) is added into the mixture under continued stirring.

At this point, for the synthesis of loaded nanocontainers an additional step is added to the synthesis. In the case of MBT and UA, 0.01 g of biocide dissolved in 25 mL of diethyl ether are added to the aqueous solution under constant stirring. While in the case of ZS, due to its low solubility in diethyl ether, a ZS solution in methanol (5 ml, 1.3% in wt) is dissolved in 25 ml of diethyl ether and added to the aqueous solution under constant stirring (400 rpm). After 30 minutes, when the miniemulsion is stabilized, 2 mL of TEOS are slowly dripped into the emulsion, using a syringe pump with a flux of 670 µl/min. The reaction is left to proceed at room temperature for 24 h under constant stirring (400 rpm). The obtained precipitate is finally filtered under vacuum, repeatedly washed (in deionised water), and dried at room temperature.

The loaded silica nanocapsules will be indicated in the text with these abbreviations: Si-NC_MBT, Si-NC_ZS, Si-NC_UA.

A small portion of all products has been calcined at 550 °C for 5 h in order to remove residual CTAB and other organic components, for control measurements.

2.3 Synthesis of the silica mesoporous nanoparticles loaded with the biocides

For the synthesis of the silica mesoporous nanoparticles (Si-MNP), a solution of CTAB (0.25 g) and biocide (0.01 g) in 20 mL of water is sonicated for 30 minutes. The same procedure has been followed for all considered biocides (MBT, ZS and UA).

At the same time in a different backer, 875 µL of NaOH aqueous solution (2.0 M) are diluted into 100 mL of deionised water and then added to the first solution. The final solution is heated to 80 ˚C. After reaching the temperature, 1.25 mL of TEOS are dripped by a burette and the final mixture is kept under fast stirring (400 rpm) for additional 2 h. Finally, the silica nanoparticles are collected by filtration and washed several times with water.

The principal steps of this synthesis procedure are reported in Fig.7.

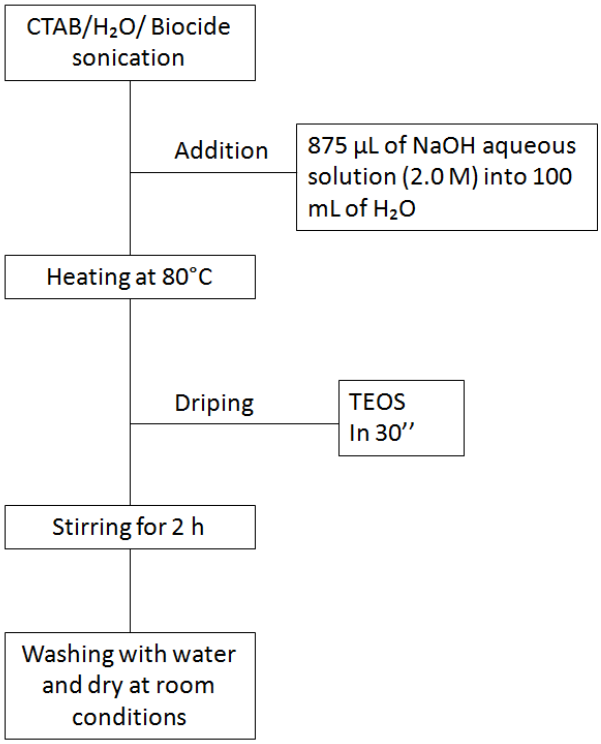

Fig.7 Flow-chart of the mesoporous silica nanoparticles synthesis procedure

As in the case of loaded Si-NC, a small portion of both products has been calcined at 550 °C for 5 h in order to remove residual CTAB and other organic components, for control measurements.

In order to evaluate the effective encapsulation of the biocide, an additional control sample has been prepared, by physical adsorption of MBT on a portion of calcined Si-MNP: these samples will be labelled as MNP-impregnated. Physically adsorption of MBT on Si-NC is performed mixing the dry silica nanoparticles with a water solution of 2-mercaptobenzothiazole (0,4 mg/ml). The MBT and Si-NC suspension was transferred to a vacuum jar, which was then evacuated by a vacuum pump.

2.4 Experimental procedure to characterize the nanocontainers under study

The nanoreservoirs have been deeply characterized as far their dimensions and textural properties, loading capability, and release rate in aqueous solution, by different analytical techniques as summarized in the diagram below (Fig. 8).

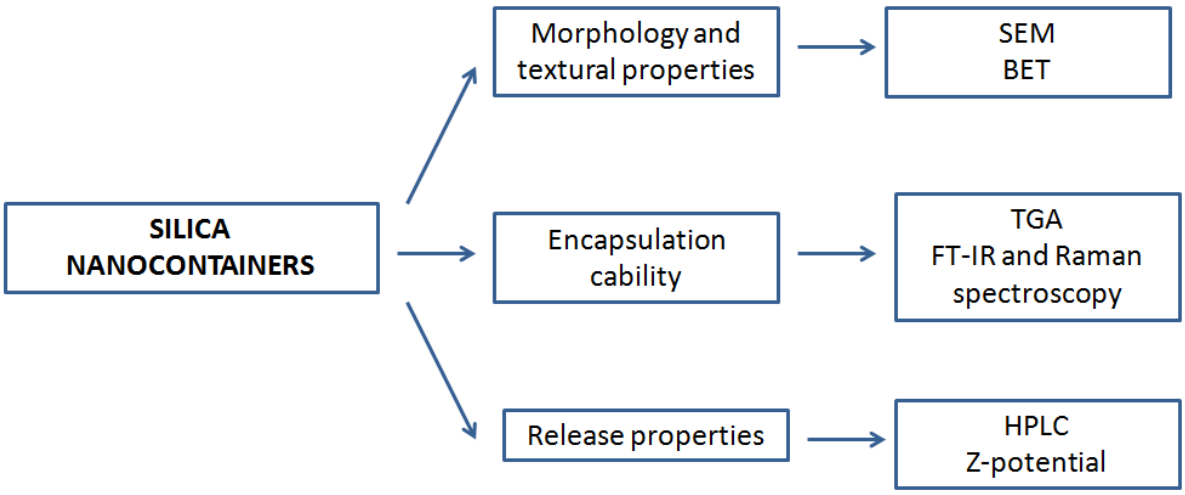

Fig.8 Diagram of the characterization techniques applied on the different silica nanoreservoirs.

The morphology of the nanosystems has been investigated by using a Field Emission Scanning Electron Microscope (FE-SEM, SUPRA™ 35, Carl Zeiss SMT, Oberkochen, Germany) with a field emission gun as electron source at an acceleration voltage of 5 to 15 kV. To avoid charging effects, the samples were previously sputtered with a thin layer of gold. Particle size has been investigated and the particles distribution processed using the ImageJ software.

Textural properties have been investigated by the N_2 adsorption–desorption isotherms at -196 °C using a Micromeritics Gemini V apparatus.
Each sample was previously degassed in flowing He at 150 °C using a Micromeritics Flow Prep accessory. The specific surface area has been calculated by the Brunauer–Emmett– Teller (BET) method by using adsorption data in the range $0.04 < P/P° < 0.30$. The pore size distribution has been obtained from the desorption branch using the Barrett–Joyner–Halenda (BJH) method. The total pore volume has been calculated from the maximum adsorption point at $P/P° = 0.98$.

Thermal stability and biocide content have been determined by thermogravimetric analysis, using a TG-DSC (Mettler Toledo, STAR System) with simultaneous thermogravimetry and scanning calorimetry abilities. The measurements have been carried out under air atmosphere, with a heating rate of 10 °C/min in the temperature range of 30-800 °C.

The presence of the biocide in the system and its interaction with the silica network can be probed by means of complementary spectroscopic techniques, specifically FTIR and Raman.

The infrared (IR) spectra of the synthesis reagents (e.g. MBT and CTAB) and the nanosilica systems were investigated using a Bruker TensorII FTIR spectrometer in Attenuated Total Reflection (ATR) mode. Samples, in the form of powder, were placed on the top of a diamond ATR crystal and pressed to obtain complete adhesion at the interface. The spectra were measured in the 4000–400 cm-1 range by coadding 256 scans at 2 cm^{-1} resolution. Due to the high refractive index of diamond (n=2.4) the penetration depth of the IR beam into the sample is about 2 microns, giving spectroscopic information comparable to the one obtained in transmission mode.

Raman measurements have been performed at room temperature using an inVia Renishaw Raman spectrometer equipped with a diode laser (785 nm, output power 200 mW), an edge filter to select the Raman scattering avoiding the elastic contribution , a 1200 lines/mm diffraction grating and a Peltier cooled 1024x256 pixel CCD detector. Samples have been mounted on the manual stage of a Leica DM2700 M confocal microscope. Focusing of the laser beam and collection of Raman signals has been realised by a 50x long-working distance objective. The spectra have been recorded using a laser power at about 39 mW on the sample. Several scans with different acquisition time, depending on the sample, have been collected in order to improve the signal-to-noise ratio. The Raman spectrometer has been calibrated prior to the measurements using a Si wafer and by performing the automatic offset correction. The spectra acquisition and data analyses have been accomplished using WiRE™ and Origin softwares. To get a representative spectrum for each sample, ten spectra, collected on different point, have been averaged and normalized. The peak positions are estimated to be accurate to at least ±2 cm^{-1}.

The release profiles of biocides have been monitored by High Performance Liquid Chromatography (HPLC) coupled with a diode-array ultraviolet (UV-DAD) detector, for the quantitative analysis. In the case of silica nanocontainers loaded with MBT an isocratic mixture of water and acetonitrile was used for the mobile phase, while for the silica nanocontainers loaded with ZS was added 0.1% formic acid to water/acetonitrile. For the release study of UA methanol was used as mobile phase. The correlation coefficient of the calibration curves obtained with 10 biocides standards was higher than 0.999.
For HPLC analysis, acetonitrile and ethanol (RS-Plus grade), purchased from Sigma-Aldrich Fluka, have been used. Distilled water was further purified through a Milli-Q Plus apparatus (Millipore, Bedford, MA USA). Samples of 5 mg of each loaded nanosystem (Si-NC, Si-MNP, MNP-impregnated) were dispersed in 1 mL of solvent (H_2O, EtOH, mixture 90:10 H_2O/ Acetone) and monitored at time intervals between 0 and 120 days. 1 mL of each sample has been collected and filtered through a PTFE syringe filter (Iso-DiscTM Filters PTFE-13-2 13mm x 0.2µm, Sigma-Aldrich) prior to injection of 20 µL into the HPLC/UV-DAD system. Liquid chromatography was performed under reversed phase (RP) conditions by means of a HPLC system Infinity 1260 series (Agilent, Santa Clara, California, USA) using Phenomenex® Luna column (C18, 50 x 4.60 mm, Phenomenex®, Torrance, California, USA) protected by a guard column of the same type (4.0 x 10 mm, 5 µm) and kept at 25°C.

The ζ potential measurements were carried out to evaluate the presence of the biocide on the nanocontainers surface. Electrophoretic mobility measurements were performed using a Malvern NanoZetaSizer apparatus, equipped with a 5mW HeNe laser (Malvern Instruments Ltd, UK) in a quasi-backscattering configuration (the diffused light is collected at an angle of 173°). Measurements were carried out using Mixed Mode Measurement (M3) method combined with Phase Analysis Light Scattering (PALS) technique, using capillary cuvettes with palladium electrodes (disposable cuvettes, Malvern, UK). The measured electrophoretic mobility μe was converted into Zeta potential through the Smoluchowski relation $\zeta = \mu e \eta / \varepsilon$, where ε is the permittivity of the solvent and η is the viscosity.

2.5 Synthesis of multifunctional coatings

The coating has been prepared as described in a recent article [105]. In short, a typical starting sol has been prepared by mixing TEOS with ethanol, and then the nanoparticles have been included in the right amounts, as summarized in Table VI: the numbers indicate the % w/v of the different kind of nanoparticles included in the materials.

Table VIII Contents of nanoparticles, expressed in percent volume of TEOS, in the multifunctional coatings

Coatings	Nanoparticles		
	TiO_2	SiO_2	
		NC	MNP
C			
C_1%TiO_2	0.1%		
C_2%_TiO_2	0.2%		
C_1%Si-NC		0.1%	
C_2%Si-NC		0.2%	
C_TiO_2/Si-NC	0.05%	0.05%	
C_2_TiO_2/Si-NC	0.1%	0.1%	
C_1%_Si-MNP			0.1%
C_1%_Si-MNP			0.2%
C_TiO_2/Si-MNP	0.05%		0.05%
C_2_TiO_2/Si-MNP	0.1%		0.1%

Technical grade TiO_2 nanoparticles (by Sigma-Aldrich), with an average particle size of ~ 21 nm, have been used as photocatalytic element into the multifunctional coating, in addition to the two different SiO_2 nanocontainers (Si-NC and Si-MNP) synthetized and loaded with MBT. In order to investigate the effects of the different kind of nanoparticles on the coatings properties, we have prepared also a blank, called C in Table VIII.

The solution has been magnetically stirred for 2 h at room conditions. Afterwards, water (3.6 ml) and PDMS-OH (0.46 ml) have been added under vigorous stirring. After 2 min of magnetically stirring, the mixture has been sonicated for 10 min. Finally, n-octylamine (13 µL) has been added to each sol and the mixture has been magnetically stirred for 20 min. After completing the synthesis, 500 µL of each sol was cast in plastic petri dishes of 1,7 cm diameter and 0,7 cm in height. Dishes were covered and maintained at laboratory conditions (relative humidity of 60% and 24°C). Gel transition and spontaneous drying took place. Dried xerogels were characterized after reaching the constant weight.

At the end, the mole ratios of each mixture are 1TEOS/16EtOH/10H_2O/0.04 PDMS-OH/0.004 n-octylamine. TEOS (analytical grade reagent), n-octylamine and PDMS-OH (Mn=550) have been purchased from Sigma-Aldrich. The formulations tested have been labelled as reported in the Table VI. Fig.9 shows a summary diagram of the starting sols.

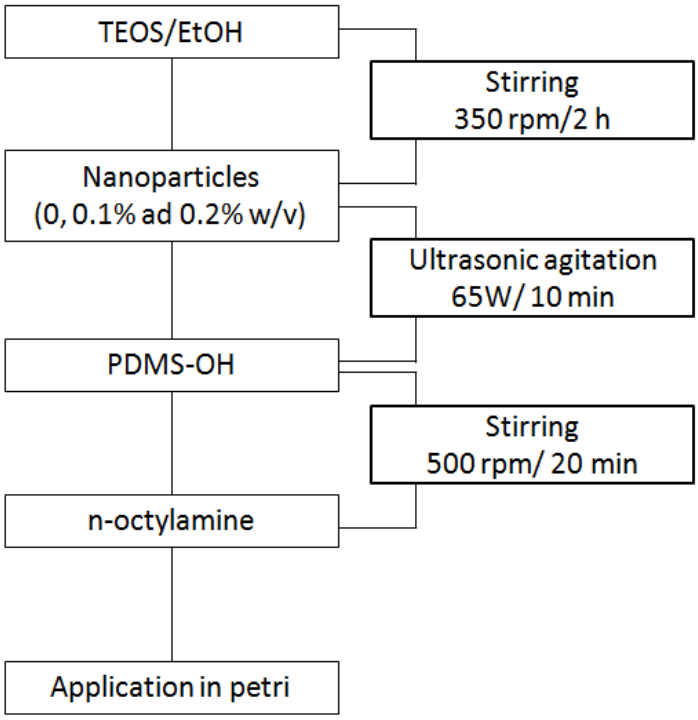

Fig.9 Summary diagram of the sols tested

2.6 Experimental procedure to characterize multifunctional coatings under study

The multifunctional coatings have been characterized as far as the optical, textural and morphological properties, by different analytical techniques, as summarized in the diagram below (Fig. 10). SEM, BET, FT-IR and Raman spectroscopy were applied on the coating after drying at constant weight, working in the same experimental condition detailed in the paragraph 1.4.

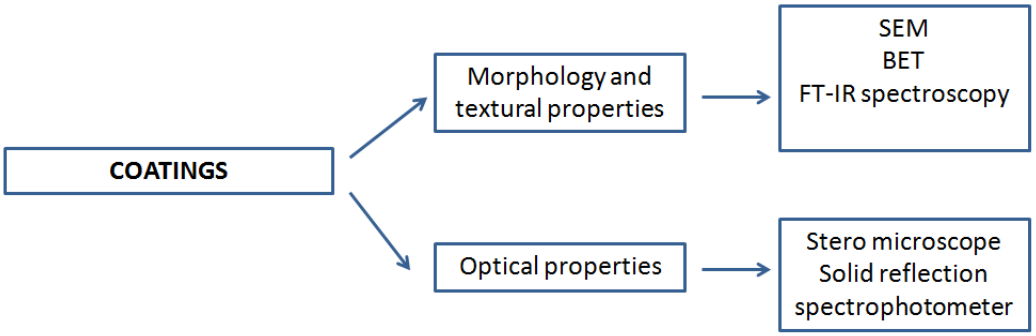

Fig.10 Diagram of the characterization techniques applied on the different coatings.

The morphology and the textural properties of the coatings were analyzed by SEM and N_2 adsorption–desorption isotherms, according the same protocol mentioned before for the study of the silica nanocontainers.

FT-IR was applied to study the chemical bonds within the coatings and to investigate the effects of the fillers on the matrix networks. FT-IR experiments were carried out on the powered samples.

Possible changes in the colour of each coating, over time, were determined by using a solid reflection spectrophotometer, Chroma-Meter CR-200 Konica Minolta. The conditions used were: illuminant D65 and observer 2°. CIE L*a*b* colour space has been used and variations in colour have been evaluated by using the parameter: total colour difference ΔE*($\Delta E^* = \sqrt{\Delta L^{*2} + \Delta a^{*2} + \Delta b^{*2}}$).

Chapter 3

Results and discussion

In this thesis, the realization of a self-cleaning coating with antifouling properties is pursued. A hybrid nanocomposite coating, containing TiO_2 nanoparticles and two different kinds of silica nanocontainers with antifouling properties, is realized, characterized and tested.

The first part of the thesis reports the synthesis and the optimization of the empty of silica nanocontainers with core-shell structure, namely nanocapsules (Si-NC). In particular, the influence of the synthesis parameters, such stirring condition and dripping methods of the silica precursor, on the size and the textural properties of the final nanocapsules is analyzed. Conversely, the synthesis protocol of mesoporous silica nanoparticles (Si-MNP) was already established [112], but the application to the *in situ* entrapment of the active compounds (e.g. biocides), to the best of our knowledge, has not been reported so far.

After the optimization and the characterization of the both empty silica nanocontainers, the encapsulation and the *in situ* entrapment of a commercial biocide (2-mercaptobenzothiazole) was explored.

Special attention was addressed to understand how the biocides molecules are confined in the two different silica nanosystems. Successively, the synthesis conditions to encapsulate two environmentally-friendly biocides (the zosteric acid sodium salt and the usnic acid) were explored. The aim was to minimize the release in the environment of low eco-compatibility compounds: on one side using the technology of the silica nanocontainers to control the release over time and to increase the efficacy of the treatment, on the other side applying the environmentally-friendly biocides.

The effects of each active compound on the two different silica nanocontainers will evaluate not only from the morphological point of view, but also from the textural and the structural point of view.
At the end, in order to evaluate the role of nanoparticles in the determination of coating properties, the addition of different amount of the two silica nanosystems and TiO_2 nanoparticles into a non commercial coating formulation were tested.

3.1 Optimization of the empty silica nanocapsules

It is well know that the synthesis parameters, such as temperature, time, concentration of the catalyst and type of surfactant influence the characteristics of the silica nanoparticles [114], in term of dimension and textural properties. Moreover, several studies have correlated the interaction between hydrolysed silica precursor and the micelles to the formation of different mesoporous silica particles [115-116]. A deeper knowledge of all the experimental conditions, that can tune the nanoparticles characteristics, could be fundamental to generate nanosystems with specific properties relevant to specific applications, such as the active compounds release.

Mesoporous materials are formed in three stages: 1) a cooperative self-assembly of inorganic/organic composites, 2) the formation of a liquid crystal-like phase of silica aggregates, and 3) a phase separation of the liquid crystal-like phase from the solution with condensation of silica species driving the growth of the solid mesostructures [117]. Dimension, shape and textural properties are strictly correlated to the second phase of the synthesis procedure.

In this work, the silica nanocapsules are produced in a one-step process through an oil-in water miniemulsion polymerization, using CTAB as template-surfactant and ethyl ether as co-solvent. These stages are schematically shown in Fig. 11. TEOS is added and polymerizes at the miniemulsion interfaces: this is an exothermic process; causing the evaporation of the volatile co-solvent from the centre of the particles (ethyl ether has a low vaporization point, 35°C). This evaporation eventually creates pores through the silica surface, with differentiated porosity from core to shell.

The formation of Si-NC, thus, is the result of a dynamic cross-coupling of two processes, namely the dynamic evaporation of the cosolvent and the stabilization process of condensation together with self-assembly driven by the CTAB [72].

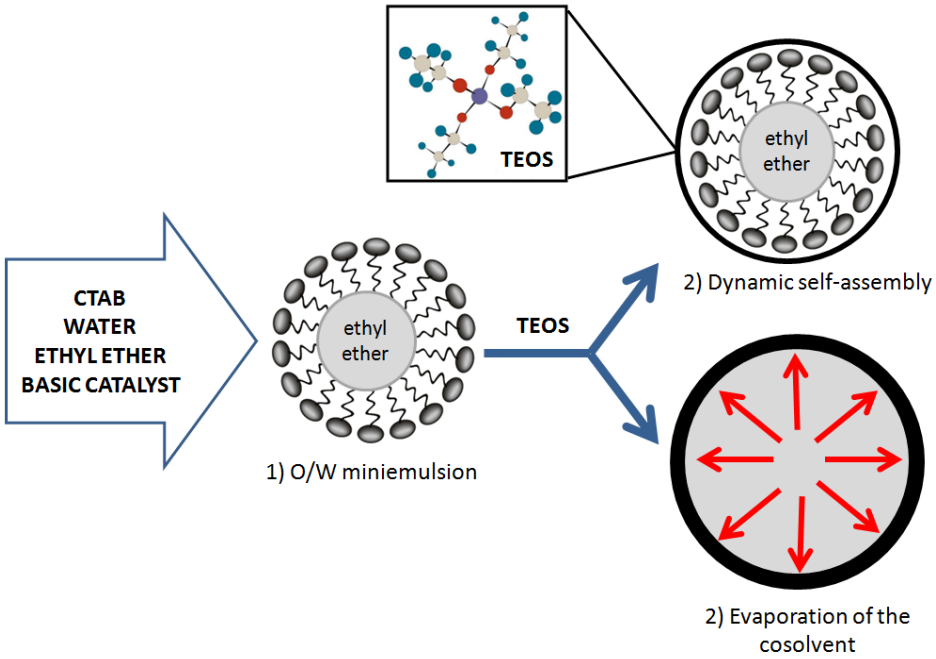

Fig.11 Illustration of the synthetic procedures of silica nanocapsules. During the dynamic self-assembly of TEOS and CTAB, cosolvent spontaneously evaporates. This determines the porosity of the nanocapsules.

According to this mechanism, the nanocapsules final shape results from competition between the free energy of mesostructural self-assembly, the colloidal surface free energy, and energy made available by other interactions, such as shear. Consequently, not only the temperature, but also the stirring rate and time during the synthesis may have an effect on the final product.

Few works explore the effects of stirring on the growth of silica nanoparticles, working or in static conditions [114] or at stirring for different times [115-116]. No reports have mentioned the effect of the stirring rate during synthesis on the morphology and on the textural properties of same silica nanocapsules investigated in this work. As will be shown, the stirring rate is not a trivial factor. It is one that can govern the structure of these silica materials and influence the uniformity of the macroscopic shape [117].

Aim of this section is to evaluate the effects on the silica nanocapsules features of both the stirring rate and of the dripping time of the silica precursor (TEOS).

Stirring has been done using a magnetic stir bar varying the rate from 450 to 350 rpm. It is well know that the addition of a compound can perturb the stability of the miniemulsion. For this reason, the addition of 1,25 ml of TEOS slowly (more than 5 minutes) and quickly (less than 2 minutes) was evaluated. TEOS has been dripped with a syringe pump for the sake of reproducibility. For this reason, the use of a burette to drip the TEOS was discarded. The different stirring rates and dripping time are listed in Table X.

The resulting silica nanocapsules were designated Si-NC-X-Y, where X indicates the stirring rate and Y indicates the dripping time of silica precursor, e.g., Si-NC-450-5 for X = 450 rpm and Y= 5 minutes.

Table X Sample nomenclature, corresponding to different stirring conditions and dripping time.

Sample	Stirring rate (RPM)	Dripping time
Si-NC-450-5	450	5’ 03” 300µl/min
Si-NC-400-5	400	5’07” 300µl/min
Si-NC-350-5	350	5’06” 300µl/min
Si-NC-450-2	450	1’47” 670µl/min
Si-NC-400-2	400	1’ 47” 670µl/min
Si-NC-350-2	350	1’ 47” 670µl/min

SEM images of the samples synthesized using different stirring rates at dripping time of ~5 minutes are shown in Fig.12, 13 and 14.

When TEOS is slowly dripped (more than 5 minutes), it is possible to clearly identify two population of spherical nanoparticles with different size. The first population of Si-NC is

characterized by smaller nanocapsules with an average particle size below 100 nm that is not influenced by the stirring rate.

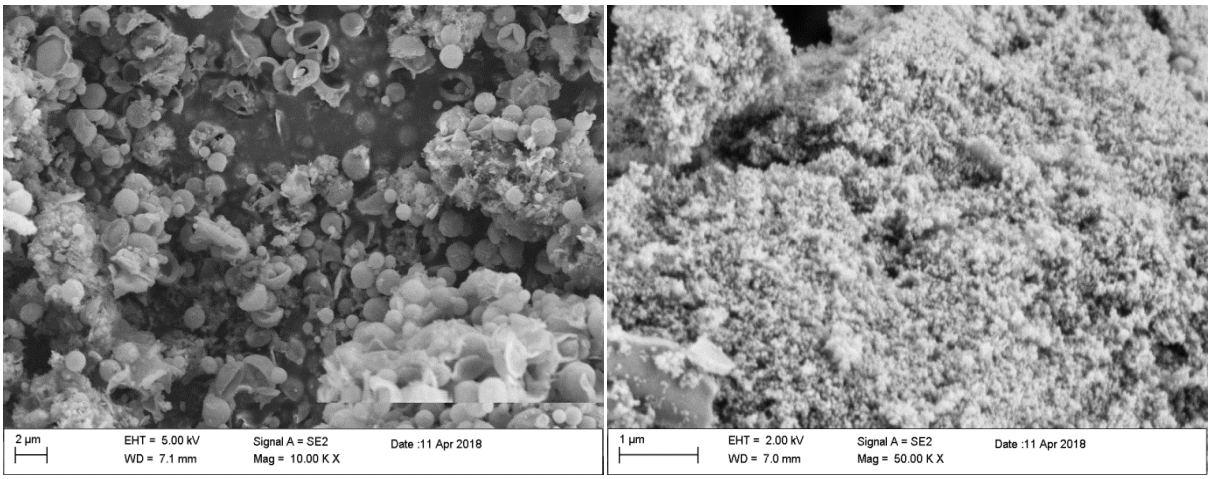

Fig.12 SEM images of Si-NC samples synthesized at 450 rpm stirring rate (a) Mag=10000 and (b) 50000.

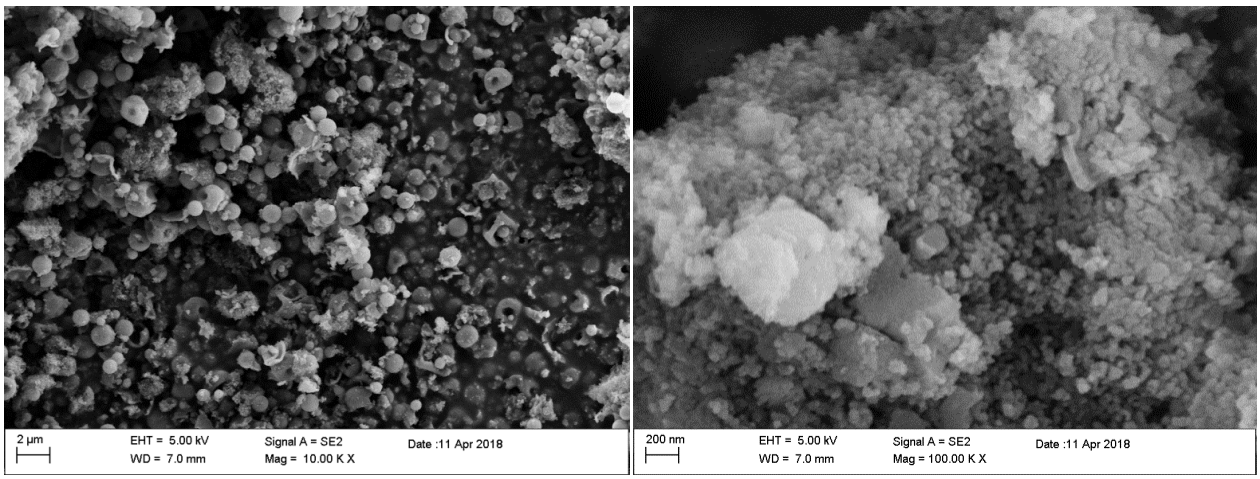

Fig.13 SEM images of Si-NC samples synthesized at 400 rpm stirring rate (a) Mag=10000 and (b) 100000.

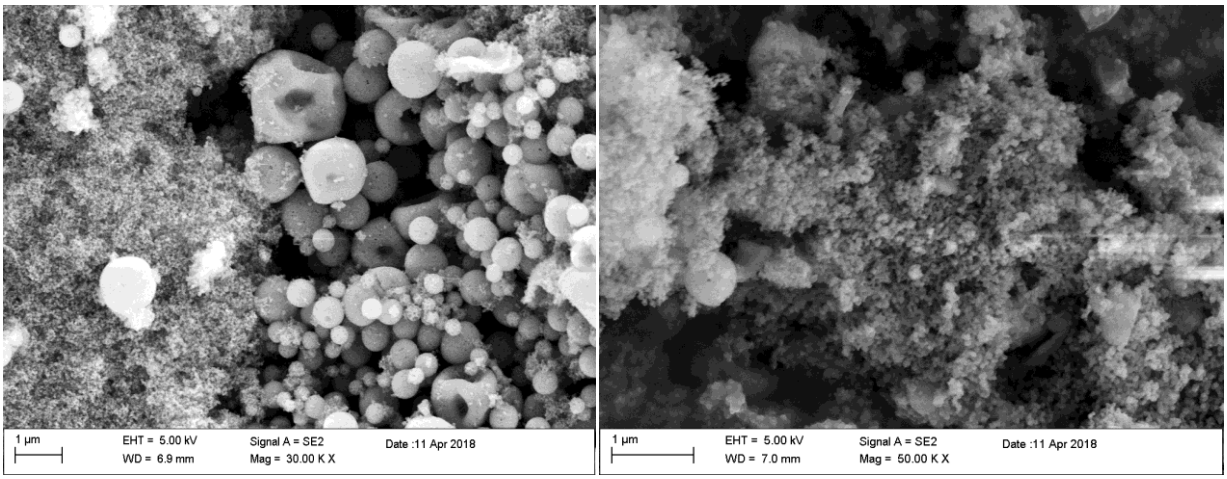

Fig.14 SEM images of Si-NC samples synthesized at 350 rpm stirring rate (a) Mag=30000and (b) 50000.

The second population shows a larger average size depending on the stirring rate, as reported in Fig. 12 a, 13 a,14 a and summarized in Table XI.

Table XI Size information about the bigger population of spherical nanocapsules

Histograms of bigger population nanocapsules size	Min	Max	Average	SD
	(nm)			
Si-NC-450-5 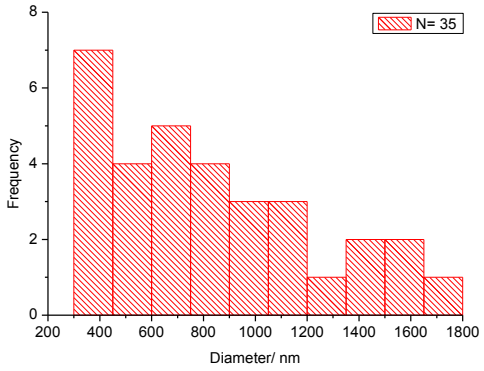	375	1650	820	70
Si-NC-400-5 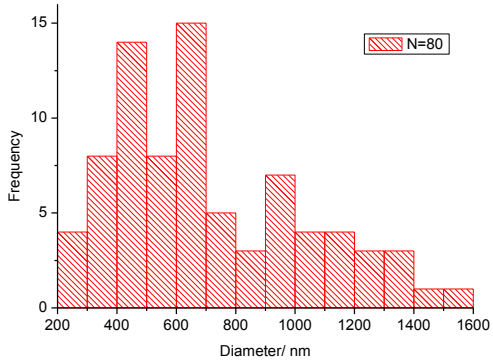	280	1550	710	35
Si-NC-350-5 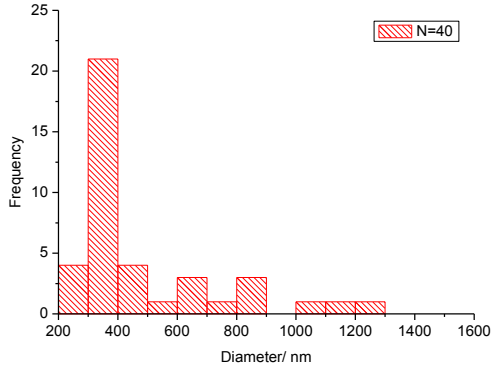	268	1204	480	40

The morphology of silica nanocapsules depends on the shape of the micelles, which is influenced by the synthesis recipe and preparation procedure. When the micelles are subject to high stirring rate (450 and 400 rpm) the coalescence is favoured and promoted by the slow dripping of the silica precursor and long stirring time, as in this synthesis procedure[3].

[3]In our synthesis procedure, samples are stirred for 24 h at room temperature.

In our conditions (slowly addition of TEOS and long stirring time), only the reduction of the stirring rate can attenuate the growth of the population of large silica nanocapsules. As reported in table XI, when the stirring rate decrease at 350 rpm, the average size drops from 820÷710 to 480 nm. When TEOS is quickly dripped (less than 2 minutes), the samples, regardless the stirring rate, show only one population with a narrow size distribution centered ~ 80 nm. In Fig.15 the morphological information of the silica nanocapsules obtained with a stirring rate of 400 rpm is reported.

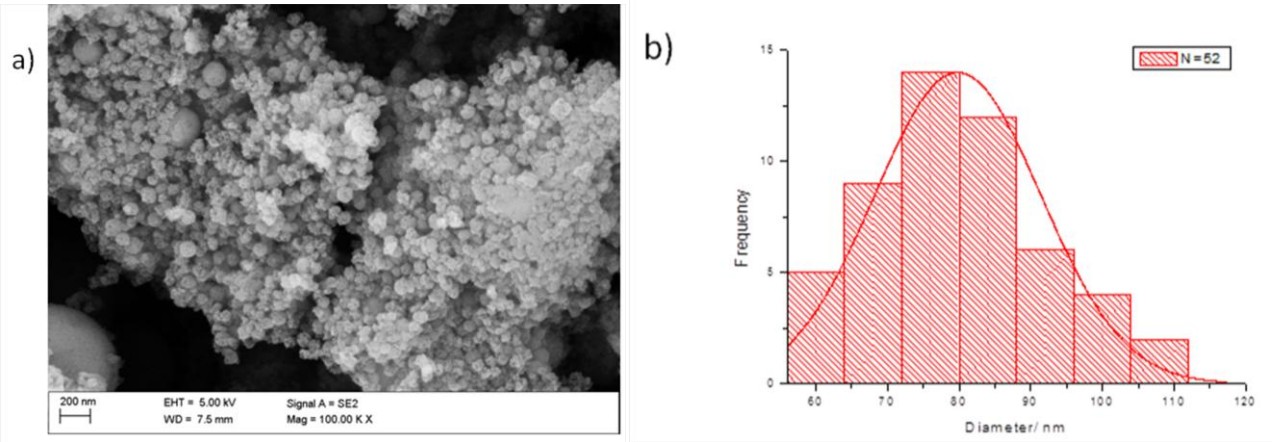

Fig.15 SEM micrograph of Si-NC-400-2 (a) and the corresponding histogram of particles size (b).

Interestingly, the size is not correlated with the textural properties of the samples, as demonstrated by the nitrogen adsorption and desorption isotherms. These results are shown in Fig. 16 and 17. BET surface area, BJH pore volume and BJH Pore size are listed in Table XII.

Very similar multilayer N_2 adsorption-desorption isotherms have been observed on all samples. The isotherms are classified, according to IUPAC, of type IV with a H1 hysteresis loop, characteristics materials having a narrow distribution of mesopores (Fig.16 a and 17 a). The isotherms show two steps of capillary condensation at high p/p^0 = 0.9 and at a low p/p^0 = 0.3, respectively, with the typical hysteresis of mesopores with cylindrical shape [118].

In detail, the specific surface area (S.A.), calculated by the BET method, ranges between 935 ÷ 1077 m^2g^{-1} and the total pore volume (BJH P.V.), calculated at P/P_0=0.98, ranges between 1.31 ÷ 1.97 cm^3g^{-1}, depending on the synthesis parameters.

Table XII Surface area (S.A.), total pore volume (BJH P.V.), and pore size (BJH P.S.) of samples

Sample	S.A. (m^2g^{-1})	BJH P.V. (cm^3g^{-1})	BJH P.S. $P/P^0 < 0.60$ (nm)
Si-NC-450-5	1042	1.67	3.9
Si-NC-400-5	1057	1.67	3.6
Si-NC-350-5	1077	1.67	3.6
Si-NC-450-2	867	1.75	3.6
Si-NC-400-2	935	1.64	3.9
Si-NC-350-2	965	1.31	3.7

The pore size distributions, calculated from the desorption branch of the N_2 isotherms, are bimodal, with a narrow peak centered between 3 – 4 nm and a broader peak centered between 80-100 nm, due to the aggregation of the nanocapsules. The average pore size (BJH P.S.), calculated in a specific P/P_0 range, is very similar among the samples (Fig.16 b and 17 b).

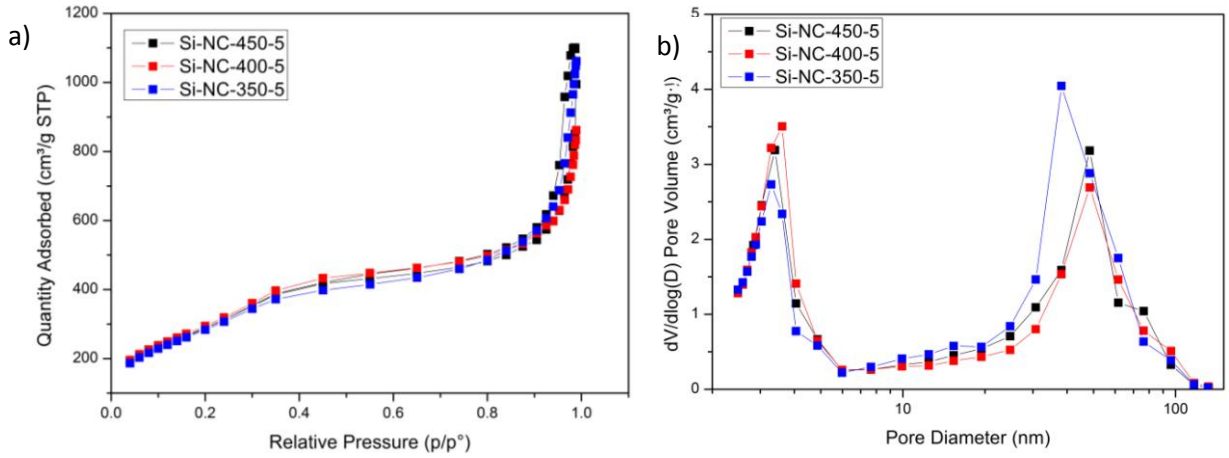

Fig. 16 Nitrogen adsorption-desorption isotherms and (b) pore size distribution of Si-NC synthesized dripping TEOS in more than 5 minutes and with different stirring rate: at 450 rpm (Black line); at 400 rpm (Red line); at 350 (Blue line).

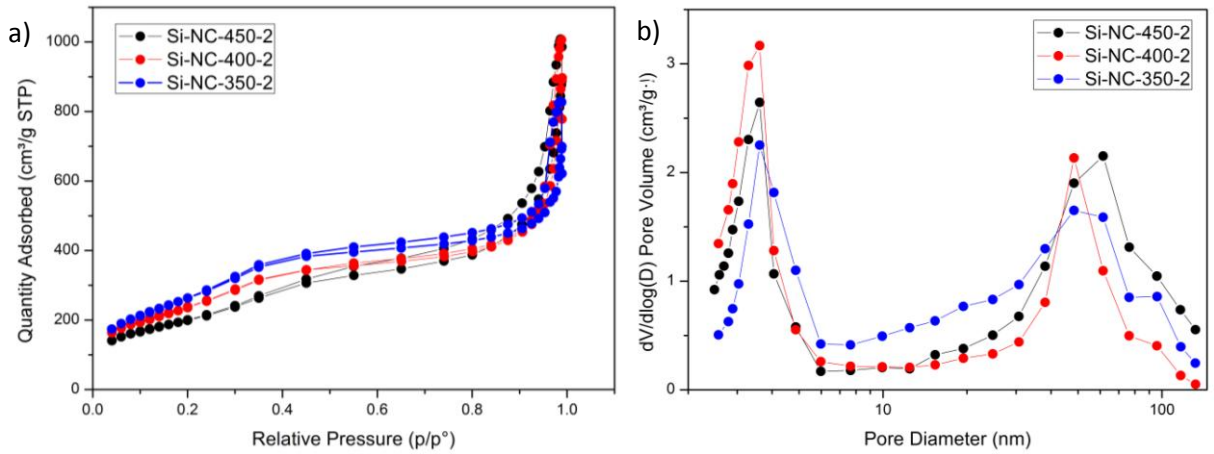

Fig. 17 Nitrogen adsorption-desorption isotherms and (b) pore size distribution of Si-NC synthesized dripping TEOS in less than 2 minutes and with different stirring rate: at 450 rpm (Black line); at 400 rpm (Red line); at 350 (Blue line).

These results show that the BET surface area increases with the decreasing the stirring rate, regardless of the TEOS dripping time.

In addition we notice that when TEOS is dripped quickly the total pore volume decreases with the stirring rate. This might be correlated with the evaporation rate of the co-solvent (ethyl ether). Indeed, as already said, the silica precursor (TEOS) condensates at the miniemulsion interface to form the inorganic silica network while the spontaneous evaporation of the ethyl ether produces the mesoporosity of the shell [30]. The latter step determines the formation of regular channels, useful for applications based on the controlled release. The low stirring slows down evaporation of the co-solvent (dynamic evaporation of the template) during cooperative self-assembly of CTAB/TEOS, determining a decrease of the total pore volume from 1.75 to 1.31 cm^3g^{-1}.

In conclusion, it is found that the stirring rate can be employed to tailor the size and the porosity of the Si-NC. When TEOS is dripped slowly, different stirring rates lead to different shear rates

that, in turn, influence the aggregation of primary particles, as well as the growth of the silica mesophase. For this reason, slower dripping time lead to two populations of spherical nanocapsules with different size; while spherical nanocapsules, with a narrow size distribution centered at 80 nm, are observed at faster dripping time. It appears that, for the synthesis of silica nanocapsules, the stirring rate has much less effect on the final particle size when the TEOS dripping time is shorter than 2 minutes, nevertheless this will affect the textural parameters such as the BJH pore volume.

This result evidences the possibility of controlling the porosity of the nanocapsules by setting the stirring and dripping parameters. Since mesoporous shell are beneficial to applications in drug delivery, not only in conservation of Cultural Heritage, this result matters because envisage the possibility of controlling the release rate over time.

For the application proposed in this study, we have selected a dripping time below 2 minutes and a stirring rate of 400 rpm for the production of empty and loaded silica nanocapsules. Indeed, for the dispersion into the coating formulation, it is desirable that the nanocapsules have a narrow size distribution and an intermediate mesoporosity to control the release rate.

Summarizing, to synthesize the core-shell nanocapsules, four reagents are required: water, a cationic surfactant, a silica precursor, and a catalyst. The silica precursor dictates the basic reaction conditions and the textural characteristics of the final product. Water, surfactant, and basic catalyst are first combined to form a homogeneous micellar solution.

In the next paragraphs, this synthesis procedure will be applied for the encapsulation of different biocides: each selected biocide is added during the synthesis using ethyl ether as cosolvent. Ethyl ether creates the oil phase in the O/W miniemulsion. The silica precursor (TEOS) condensates at miniemulsion interface to form the inorganic silica network and the spontaneous evaporation of the ethyl ether produces the mesoporosity of the shell [121]. This step is fundamental because allows the formation of regular channels for the controlled release of the biocides.

3.2 Silica nanosystems loaded with MBT

The syntheses of two silica nanosystems, namely nanocapsules (Si-NC) and nanoparticles (Si-MNP), loaded with the 2-mercaptobenzothiazole were realized, involving, at basic conditions, the hydrolysis and polycondensation of the silica precursor (TEOS) at the interface of cationic surfactant micelles (CTAB) [112].
The encapsulation of MBT into Si-NC was performed by testing different amount of biocide and of TEOS. Starting from the procedure reported by Maia et al. [122], several attempts were performed to obtain the silica nanocapsules loaded with MBT (see table XIII).

Table XIII MBT and TEOS concentrations used in the different formulations.

Sample	TEOS (ml)	MBT (g)
Si-NC_MBT (A)	1,25	0,1 g
Si-NC_MBT (B)	2	0,1g
Si-NC_MBT (C)	2	0,05g
Si-NC_MBT	2	0,01g

The first attempt has been made by adding 0.1 g of MBT in the formulation containing 1.25 ml of TEOS (see table XIII). The SEM micrograph of the Si-NC-MBT (A) obtained with this concentration is shown in Fig.18 and does not contain nanoparticles, but only irregular aggregates.

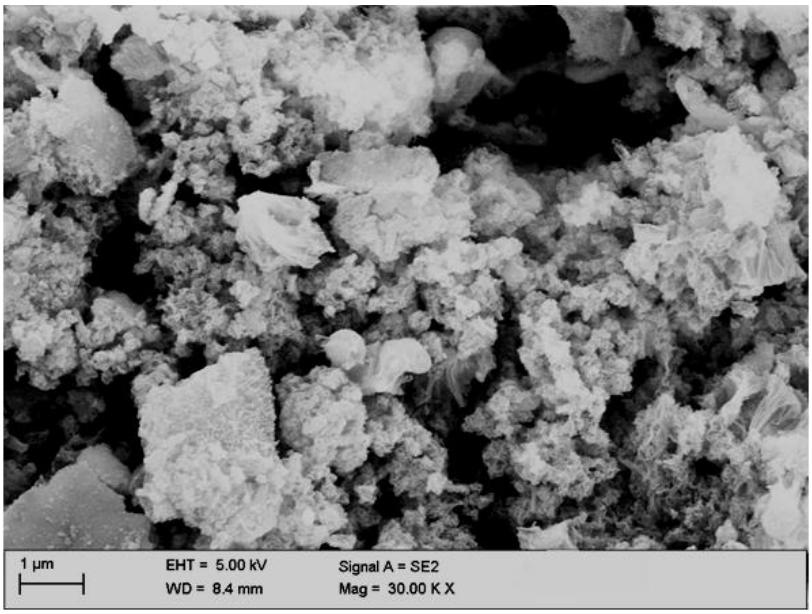

Fig. 18 SEM micrograph of the Si-NC_MBT (A).

In order to understand the reasons of this unexpected result, we have initially increased the TEOS concentration and then reduced the MBT concentration, until a sample showing only well shaped nanoparticles is obtained.

Indeed, the sample Si-NC-MBT(B) is synthesized increasing the concetration of the silica precursor from 1.25 ml to 2 ml. The amount of the biocide is the same of the previous sample. In this case the SEM micrograph shows irregular aggregates, slips and the absence of any nanoparticles, as well (Fig.19).

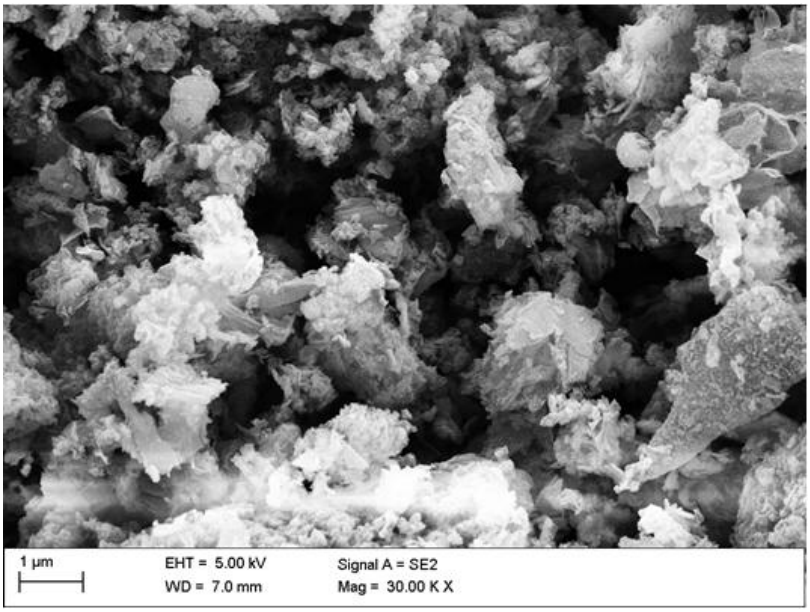

Fig. 19 SEM micrograph of the Si-NC_MBT (B)

Since the morphology of the sample is closely linked to the micellization of the cationic surfactant, a third test has been performed to verify the effect of the biocide concentration on the micellization step. For this reason, in the sample Si-NC-MBT (C) the biocide concentration was halved and the concentration of TEOS was kept constant. The SEM micrograph of this latter sample shows spheroid structure embedded into an irregular matrix (Fig.20), thus suggesting that the critical aspect is the concentration of the biocide.

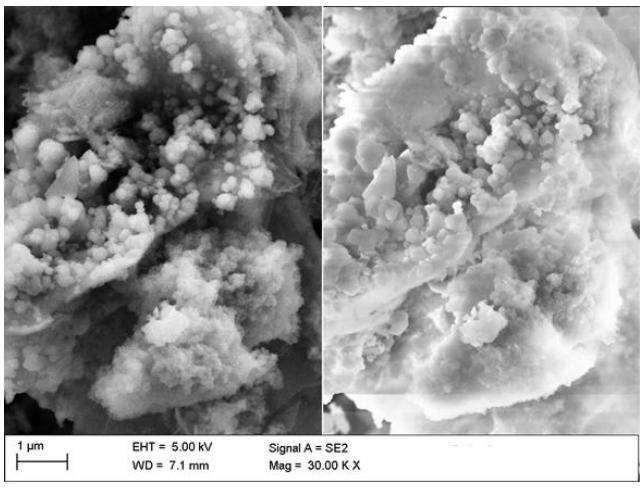

Fig. 20 SEM micrograph of the Si-NC_MBT (C)

In the light of these results, in order to stay on the safe side, for the final synthesis, the biocide concentration has been reduced, to 0.01 g per 2 ml of TEOS. Fig. 21 shows the SEM micrographs of the loaded Si-NC-MBT, along with the histogram of the particles size distribution. This shows that the loaded nanocapsules have spherical and regular shape. Nevertheless, it is worth to notice that

the average particle size (Fig. 21 b) is larger than that of the empty Si-NC. This suggests that the dimension of the biocide molecule shapes the size of the surfactant micelles and thus of the loaded Si-NC.

We stress that the larger diameter of the loaded particles, namely (128 ± 15) nm compared to (80 ± 11) nm for the empty ones, is an evidence of successful encapsulation. The red arrows in Fig. 21 a) point to two broken particles, which give evidence for the core-shell structure of the Si-NCs. Moreover the largest particles in this image clearly evidence the porosity of the surface.

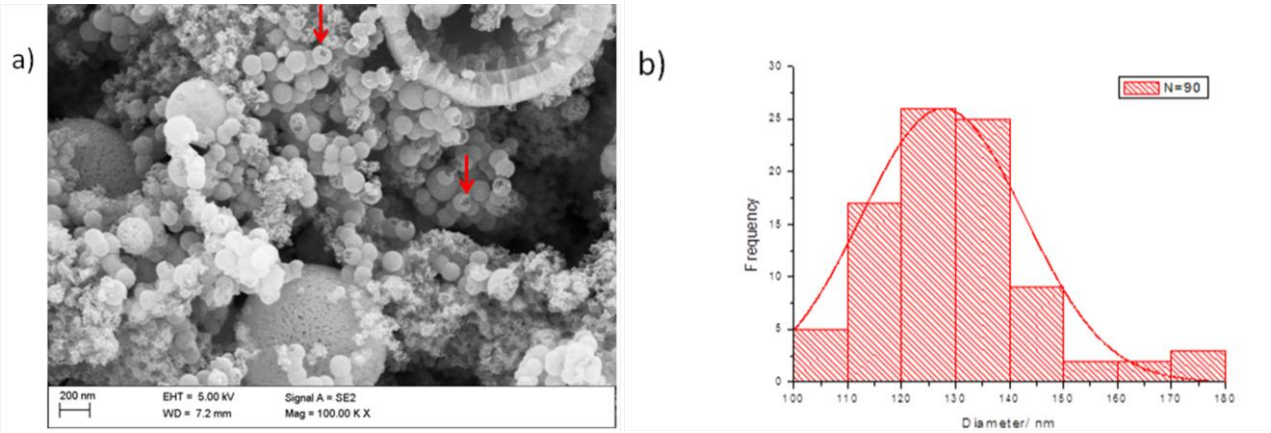

Fig.21 SEM micrograph of Si-NC-MBT (a), showing well formed spherical particles. The red arrows indicate two broken nanoparticles, evidencing the core-shell structure. (b) Histogram of particles size.

In the case of Si-MNPs the biocide is added directly into the mixture before the formation of the micellar solution without the addition of a cosolvent. Afterward, TEOS molecules hydrolyze and condensate around surfactant/biocide arrays, which play the role of template. In this case, CTAB has been used as pore-templating agent: this gives a structured tubular mesoporous matrix, hosting the MBT. Noteworthy, to the best of our knowledge, the confinement/ entrapment of MBT *in situ*, according the latter procedure, has not been reported so far.

The loaded Si-MNPs appear as spherical grains with a diameter distribution function centred at (39.0 ± 4.5) nm (see Fig.22 (a) and (b)).

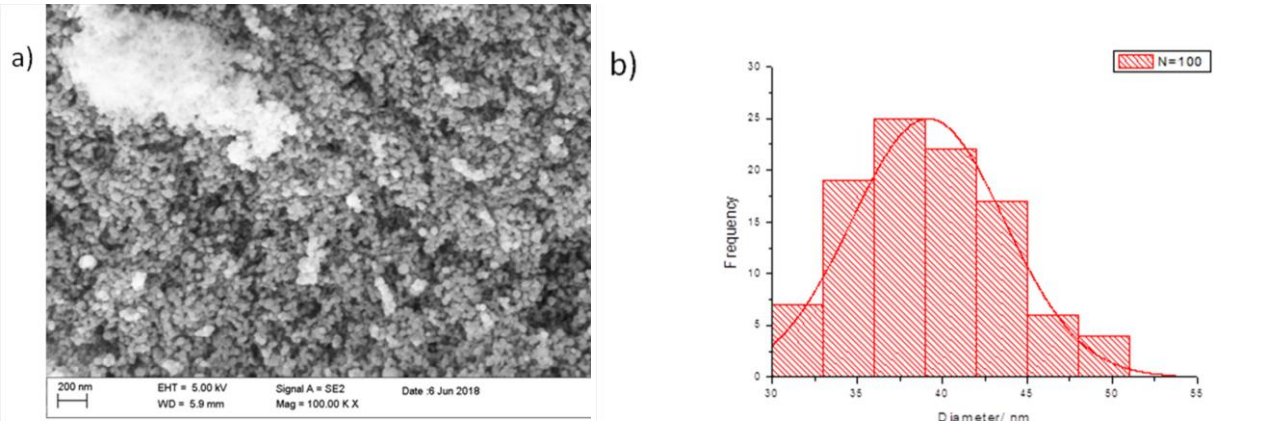

Fig.22 SEM micrograph of Si-MNP-MBT (a) and the corresponding histogram of particles size (b).

Remarkably, the average diameter of the Si-MNP-MBT is one order of magnitude smaller than that of the Si-NC-MBT ones. Such large difference in size is due to the different synthesis procedure and nature of trapping. Indeed, the dimensions of the Si-NC nanocontainers are limited by the dimensions of the oil phase containing the biocide into the cationic surfactant micelles, as reported in the scheme below (see Fig. 23). While in the synthesis procedure of Si-MNP the biocide is interpenetrated with CTAB in the micelle structures and consequently in the nanoparticle structures.

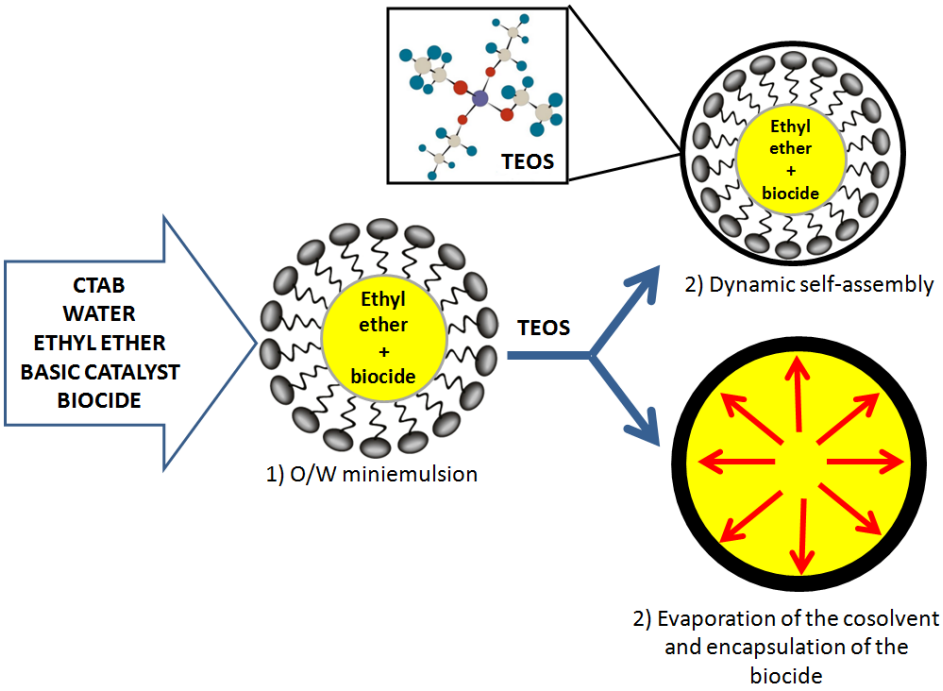

Fig. 23 Illustration of the encapsulation of the biocide into nanocapsules. During the dynamic self-assembly of TEOS and CTAB, cosolvent spontaneously evaporates and the biocide is encapsulated.

The textural properties of the silica nanosystems loaded with MBT have been evaluated by N_2 adsorption-desorption measurements and summarized in table XIV. Both nanocapsules and nanoparticles show type IV adsorption isotherms, with a hysteresis loop characteristic for materials with mesoporous structure (see Fig.24a) [123].

As already said, the Si-NC nanocontainers have a Brunauer-Emmett-Teller (BET) specific surface area of ~ 965 m^2/g with an average pore volume of ~ 1.31 cm^3/g; average BJH pore diameter of the cylinder ~ 3.6 nm. When loaded with MBT these parameters become: ~ 720 m^2/g, ~ 1.62 cm^3/g, and ~ 3.8 nm (Fig. 24 b), respectively.

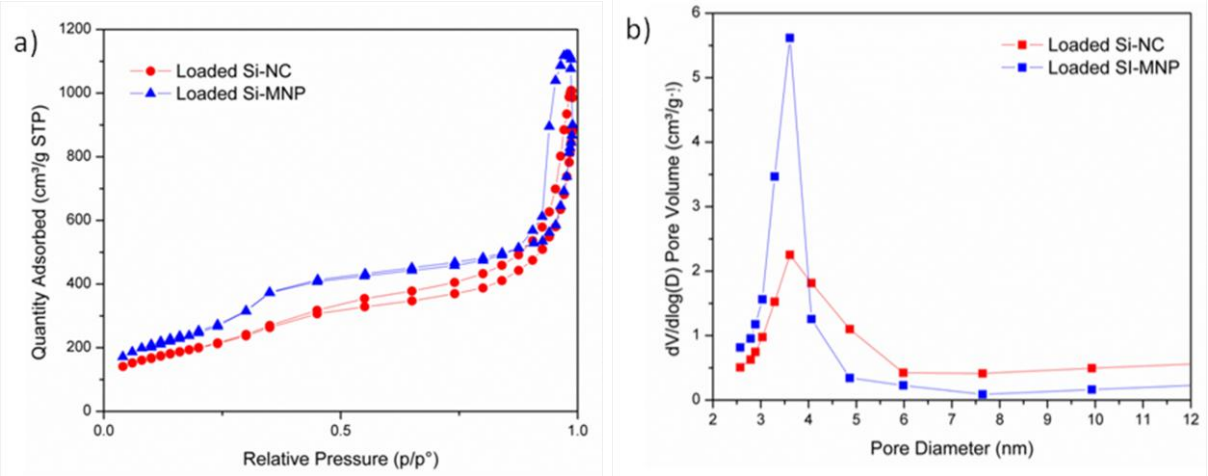

Fig.24 (a) Nitrogen adsorption-desorption isotherms and (b) pore size distribution of Si-NC-MBT and Si-MNP-MBT

In the case of the empty Si-MNPs, we remind that the surface area is ~ 960 m^2/g, the BJH average pore size is ~ 3.9 nm and the pore volume of ~ 0.71 cm^3/g. These parameters in the case of the Si-MNPs loaded with MBT become ~ 924 m^2/g, ~ 3.6 nm and ~ 1.86 cm^3/g, respectively.

In both cases, the loaded nanoparticles have a lower surface area compared to the empty ones: this is a sign of the presence of MBT inside the particles, determining also larger pore size.

The change of the surface area due to the presence of the biocide is smaller in the case of the Si-MNPs compared with Si-NCs, and reflects the different structure of the nanosystems. The increase of the pore volume after loading is instead larger for Si-MNPs, because in this case MBT interpenetrates and is entrapped in the silica matrix of the nanoparticles.

Table XIV Surface area (S.A.), total pore volume (BJH P.V.), and pore size (BJH P.S.) of samples empty (Si-NC and Si-MNP) and loaded (Si-NC-MBT and Si-MNP –MBT).

Sample	Diameter (nm)	S.A (m^2g^{-1})	BJH P.V. (cm^3g^{-1})	BJH P.S. $P/P^0 < 0.60$ (nm)
Si-NC	80	965	1.31	3.6
Si-NC-MBT	128	720	1.62	3.8
Si-MNP	-	960	0.71	3.9
Si-MNP-MBT	39	924	1.86	3.6

Both nanosystems exhibit mesoporosity: in the case of Si-NCs the pores are located on the shell and are significantly smaller than the diameter of the nanostructure; in the case the Si-MNPs the structure is similar to a sponge. The high surface area and the distribution of mesopores are very important properties for a controlled biocide release, as we will show below in the release tests.

In order to verify the presence of the MBT into both silica nanocontainers and to investigate the nature of the confinement of the biocide, FT-IR and Raman measurements were carried out. Both

these techniques are very useful to analyze the influence of the nano -structure on the molecular mobility of the guest molecules in the nanosized pores and channels.
In addition, to highlight the different confinement of the biocide in the two different silica structures ζ-potential comparative measurements are reported.

The two silica nanoreservoirs loaded with 2-mercaptobenzothiazole, along with the empty ones have analyzed by FT-IR and Raman spectroscopy. The latter samples have been used as control, to evaluate the silica bands, its network vibrations and the presence of residual cationic surfactant (CTAB) [124]

The ATR FT-IR spectra of both nanosystems (Si-NC and Si-MNP) show the characteristic bands associated with the silica shell. Silica presents a characteristic region of peaks from 1250 to 700 cm^{-1} that can provide structural characteristics of the network. Specifically, the large band centered at 1085 cm^{-1}, corresponding to the asymmetric ν(Si–O–H) stretching mode, can be deconvoluted in four components, two longitudinal (LO) and two transverse (TO) optic modes, depending on the different arrangement of siloxane rings, namely four-membered $(SiO)_4$ or six-membered $(SiO)_6$ arrangement (see Fig.25). Interestingly, literature reports that the position and relative intensities of the LO and TO modes change when chemical groups or organic molecules are added to the silica network [125-126].

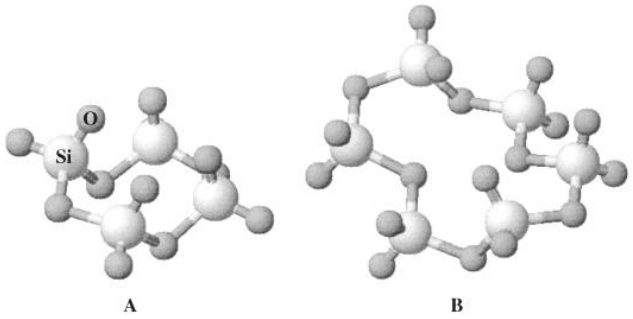

Fig. 25 Schematic diagram of the more common types of primary cyclic arrangements of the structural units, SiO_4, in xerogels: (A) four-member siloxane ring $(SiO)_4$ and (B) six-member siloxane ring $(SiO)_6$.

In the ATR FT-IR spectra of the Si-NC-MBT, we observe a peak at 754 cm^{-1} due to the C-S-stretching: confirming a successful encapsulation. Moreover, we observe a broadening and a shift of the Si-O-Si asymmetric stretching band frequency towards higher wavelengths [125-126]. The second derivative of the absorbance spectrum (Fig. 26) enhances the band shift.
These shifts are related to the network deformation needed to accommodate the MBT organic groups within the inorganic silica matrix, resulting in larger siloxane rings and greater Si–O–Si angles and longer Si–O bond lengths [127]. This may be the case for Si-NC and not for Si-MNP, where the biocide is placed in the interstitial space among silica network.
Other spectral variations are observed in the region of the C=S and C-C stretching modes of the biocide that are superimposed to the silica signal. The same applies to the peak at 1228 cm^{-1} that shifts by 10 cm^{-1} because of the strong band of the biocide at 1243 cm^{-1} attributed to the C-N stretching [128].

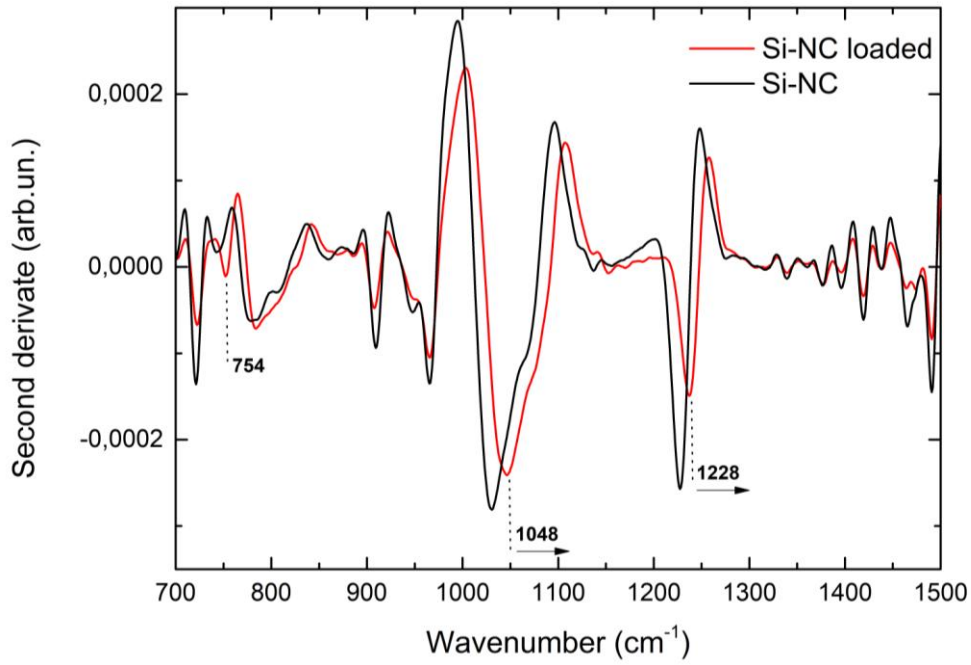

Fig.26 ATR FT-IR spectra second derivate of the Si-NC loaded (red) and empty (black).

When the biocide is entrapped in the Si-MNPs, the ATR FT- IR spectrum shows, in addition to the peak at 754 cm^{-1}, two well-defined bands at 1031 and 1074 cm^{-1}, which are associated with the C=S stretching and SH bending modes of the MBT (Fig.26). According to the literature, these data confirm the presence of the biocide in the powders under analysis and underline that the biocide molecules are subject to a different spatial confinement, compared to the Si-NC case.

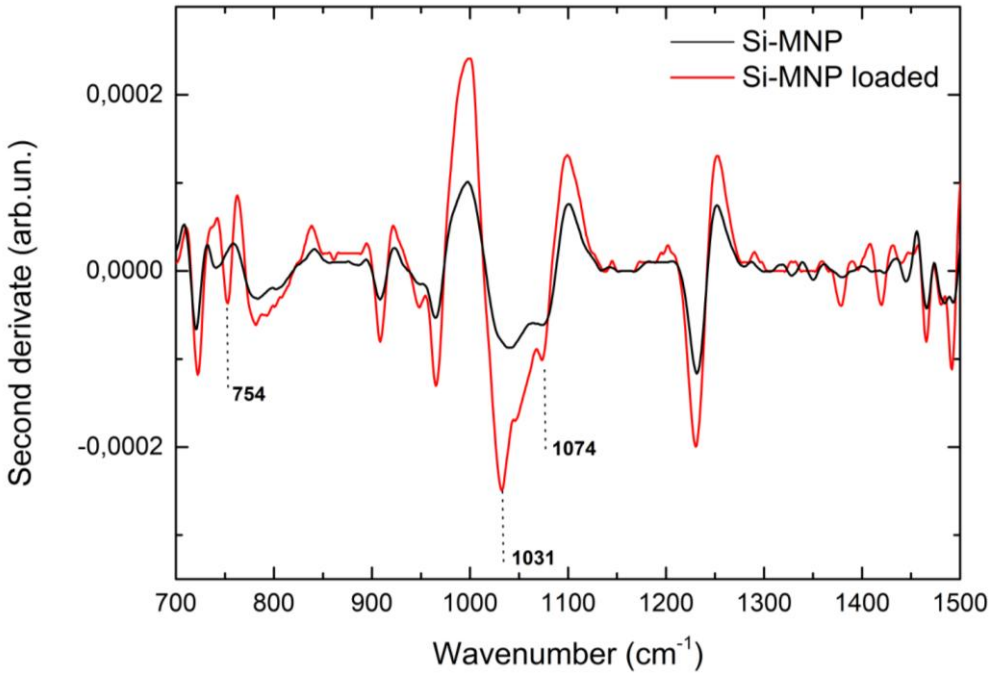

Fig.27 ATR FT-IR spectra second derivate of the Si-MNP loaded (red) and empty (black).

To better confirm the hypothesis of different interaction of the biocide with the silica structure, structural information will be provided, as well as FT-IR *in-situ* analysis to follow the structural network arrangement during the synthesis procedures.

Raman spectra of both empty and loaded nanosystems are reported in Fig. 28 and Fig. 29, respectively. Here we discuss only the 100–1.800 cm^{-1} region of the spectra: this is indeed the fingerprint region of the loaded nanosystems, which may be sensible to the presence of the biocide (MBT). The detailed assignment of all the bands of the biocide, the cationic surfactant and the silica structure reported in the literature [124,127], will guide the interpretation of the spectra of the two nanosystems.

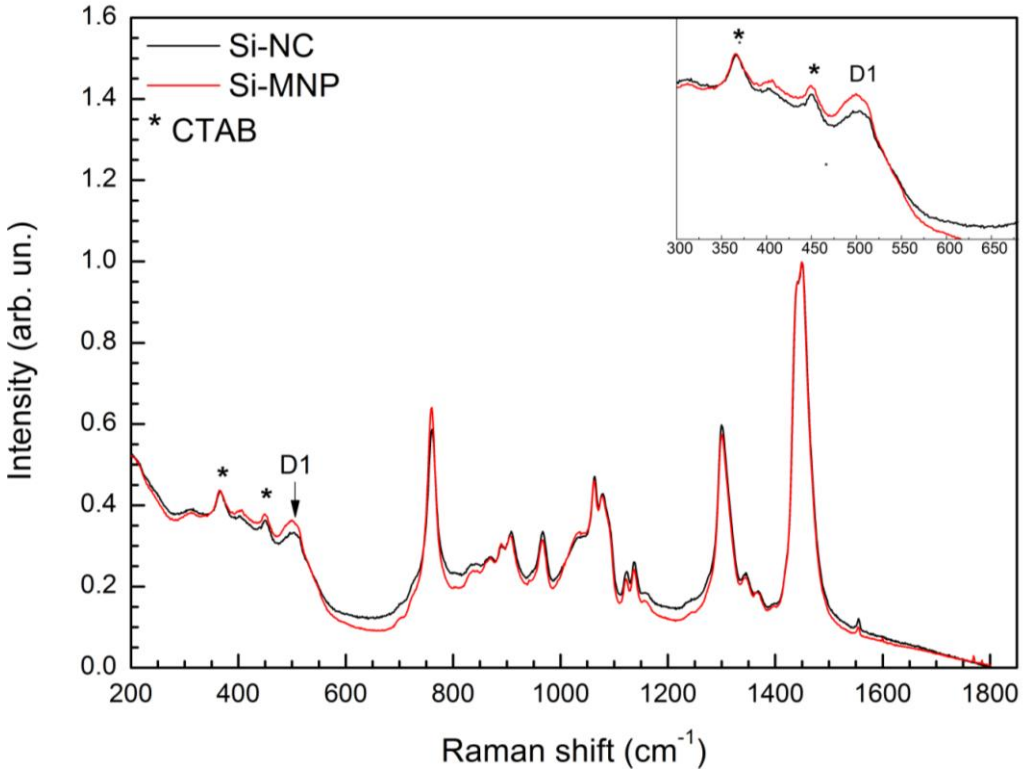

Fig 28 Raman spectra of the silica nanocapsules (black) and the silica nanoparticles (red).

In particular, the investigated region provides information on the structural characteristics of the silica nanocontainers and about the degree of polymerization of the silica precursor [127]. The Raman measurements highlight that the polymerization of the precursor is complete indeed the band associated with the stretching mode ν(Si-OH), at 945 cm^{-1}, typically assigned to the hydrophilic residual silanol group, is not visible [126-127]. In the range between 200 and 650 cm^{-1}, the only easily detectable vibrational contribution from the containers is the D1 band at 495 cm^{-1}, due to the breathing mode of the siloxane ring (with 3 or 4 SiO units). Previous studies report that the amplitude of this band gives qualitative information about the specific surface and the dimensions of the nanosystems, as it increases with the specific surface area [129-130]. In our case, the amplitude of this band is larger in Si-MNP compared to Si-NC, according to the surface area data (see inset in Fig.28). Other vibrational features ascribable to silica structure are not clearly identifiable because of the presence of the CTAB contribution.

The vibrational contributions of the CTAB enrich the spectra of the nanosystems (both empty and loaded) with many strong bands, as summarized in Table XV. CTAB plays in both syntheses the role of templating agent. Although after each synthesis, the final product was washed with water several times to remove the CTAB, yet the Raman and FT-IR spectra evidence the presence of its residues. Interestingly the ratio of CTAB/ silica seems the same for the two samples, as suggested by the intensity ratio of the CTAB peaks after the spectra normalization: this proves the good reproducibility of the synthesis protocol.
The encapsulation of the 2-mercaptobenzothiazole into the silica nanocontainers is confirmed also by the Raman measurements, reported in Fig.29.

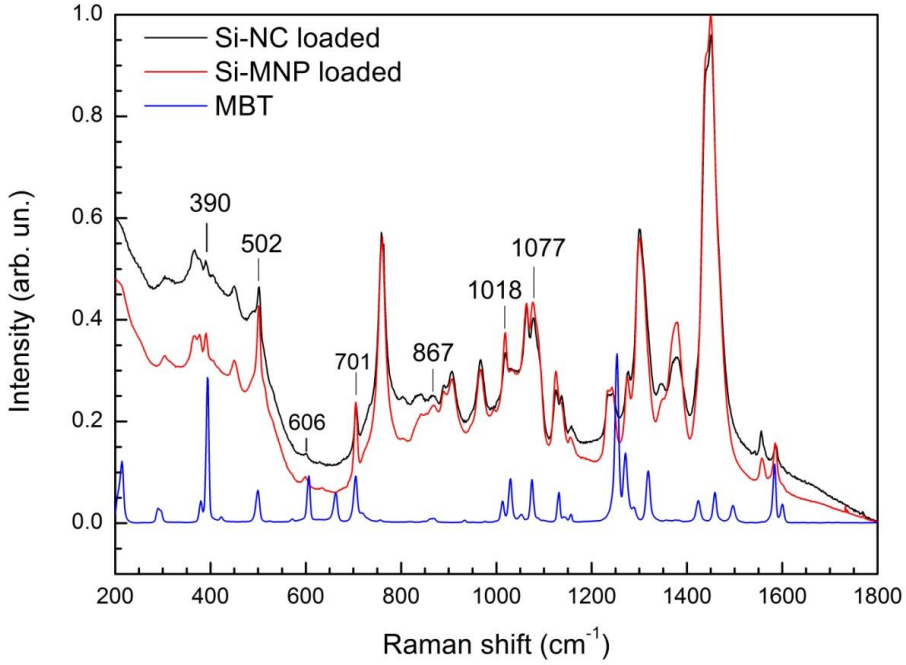

Fig.29 Raman spectra of both silica nanocontainers loaded with MBT, compared with MBT standard spectrum.

At low wavenumbers, the peaks that can be assigned to the biocide are superimposed on the spectral profile of the silica signals. The well-defined band observed at 390 cm^{-1} is ascribed to S-C=S bending vibration. The band at 502 cm^{-1} is ascribable to CCC and CCN bending. The stretching of C-S bond is evident at 606 and 701 cm^{-1}. At 867 cm^{-1} we can observe CCC bending, CC and CN stretching. In the region between 1000-1100 cm^{-1} it is possible to discriminate the vibrational contribution of the endocyclic and exocyclic sulphur atoms, respectively: the band at 1018 cm^{-1} is associated to CH bending, CS stretching in S-C-S and the band at 1077 cm^{-1} is related to CS stretching in S-C-S, CCC bending, C=S stretching [128].

Table XV reports the comparison between the vibrational wavenumbers of the Si-NC and the Si-MNP (empty and loaded) and the vibrational contributions of MBT and CTAB. Because of the very similar values of several MBT and CTAB bands, when the band is present in the loaded nanocontainers only, it is associated to the biocide, while, if it is present in the empty and loaded nanosystems as well, it is linked to the CTAB.

Table XV *Vibrational wavenumbers in cm^{-1} of silica nanocapsules (Si-NC) loaded and empty, and silica nanoparticles (Si-MNP) loaded and empty, compared with the vibrational wavenumbers of the biocide (MBT) and the cationic surfactant (CTAB). In bold the vibrational assignments related to the presence of the MBT.*

Si-NC	Si-NC loaded	Si-MNP loaded	Si-MNP	MBT	CTAB
-	**390**	**390**	**-**	**394**	-
450	450	450	450	-	450
502	502	502	500	500	500
-	**598**	**603**	-	607	-
-	**701**	**701**	-	**701**	-
761	759	759	758	756	761
837	838	840	833	-	831
-	**867**	**869**	-	**869**	867
890	890	890	890	-	887
909	907	907	907	-	905
965	965	965	966	-	960
-	**1018**	**1019**	**-**	**1013**	1011
1062	1062	1062	1063	1053	1062
-	**1079**	**1077**	-	**1074**	-

Interestingly, in addition to the above quoted bands, new bands, absent in the reference spectra, are observed in the regions between 1230-1250 cm^{-1} and 1330-1410 cm^{-1} (see Fig.30).

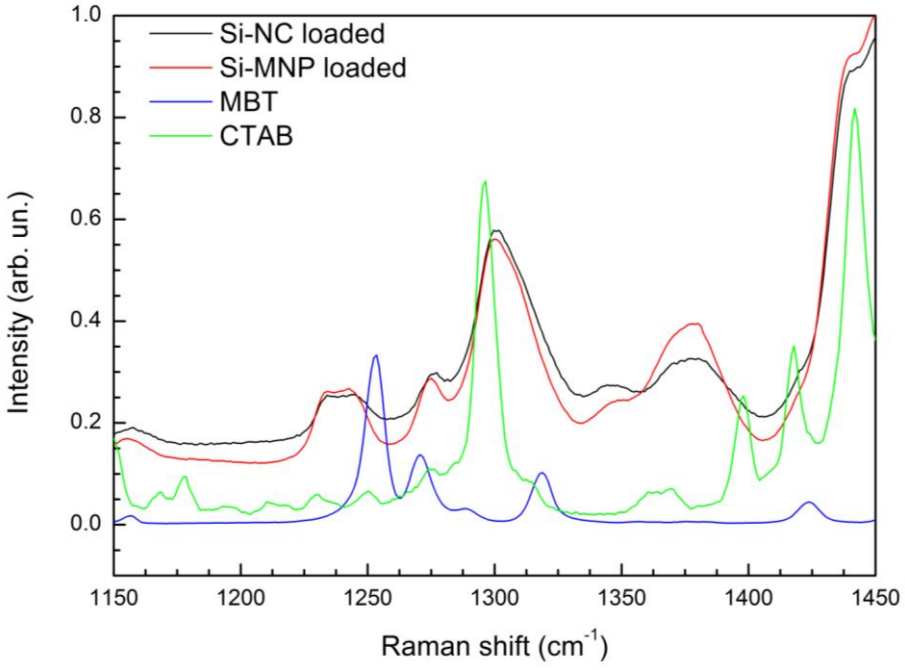

Fig. 30 Details of the Raman spectra reported in compared with the spectra of the pure MBT and CTAB powders.

The shorter wavenumber range is typically assigned to the CN stretching mode of the biocide and of CTAB, and to the CNC bending of CTAB. The spectra of the loaded nanosystems, compared to the pure compound, show a splitting of the band at 1253 and a red shift of the peak at 1270 cm^{-1}

[131-132]. These features may be the signature of a chemical reaction between CTAB and MBT [133-134].

According to the literature, the bands, observed in the longer wavenumber range (1330-1410 cm^{-1}), can be attributed to the CH and NH bending, and the CN stretching of the dimeric complex [135], formed by two molecules in thione form linked by linear N-H···S hydrogen bonds [136]. This suggests that the MBT, in both the synthesis conditions, is more stable in the dimeric conformation.

Summing up, Raman results clarify that the biocide interacts with the cationic surfactant through the nitrogen atom and tends to dimerize. These spectroscopic evidences underline how the increase of the biocide amount in the synthesis leads to the instability of the system, inhibiting the cationic surfactant micellization.

Moreover, FT-IR and Raman measurements show that the biocide contributions are more intense in the mesoporous nanoparticles (Si-MNP). This suggests that, while in Si-NC the biocide is encapsulated in the core of the silica nanocapsule, it is dispersed into the matrix of the mesoporous nanoparticles in the case of Si-MNP, thus being more easily detected.

To verify this suggestion, ζ-potential measurements as a function of time have been performed. Loaded Si-NCs and Si-MNPs have been suspended in deionised water and electrophoretic mobility has been measured as a function of time, starting from immediately after the suspension preparation (t = 0 *s*). At each time we obtained a rather narrow Gaussian distribution of ζ-potential values that is centered at about 5 mV / 7 mV for empty/loaded Si-NC and 4 mV / 5 mV for empty/loaded Si-MNP. The central values of these distributions are shown as a function of time in Figures 30 a and 30 b, for both empty and MBT loaded nanosystems. Solid and dashed lines represent the best linear fit of the experimental data and best fit parameters are reported in the legends.

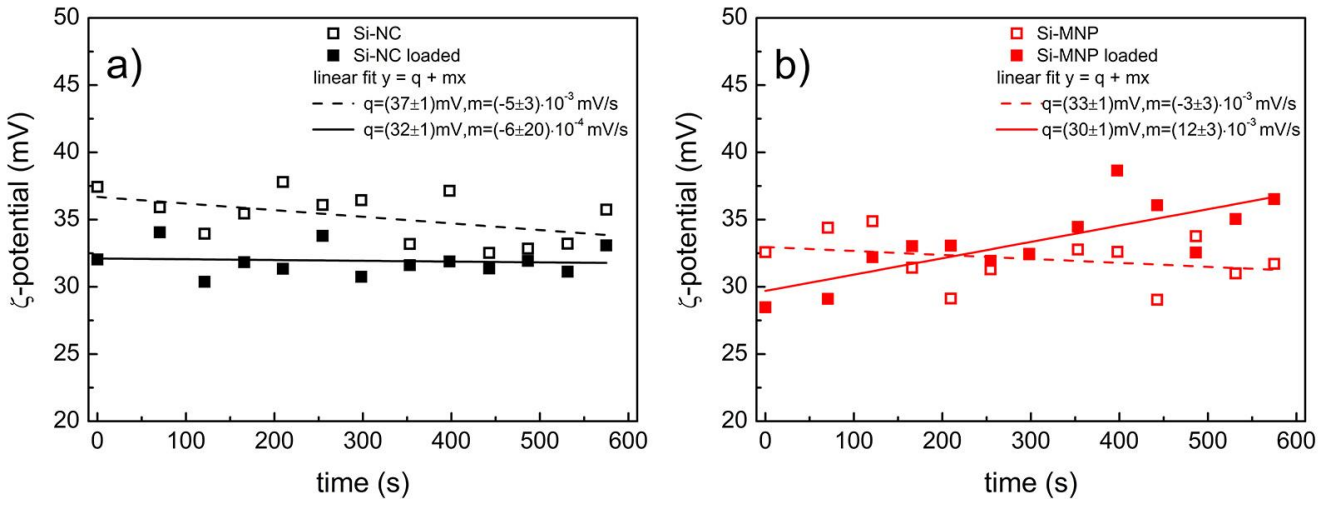

Fig. 31 Central values of the ζ-potential distributions measured as a function of time: a) empty (black open squares) and MBT loaded (black filled squares) Si-NC; b) empty (red open squares) and MBT loaded (red filled squares) Si-MNP. Best fit lines (dashed for empty and solid for loaded) and relative parameter values are reported in the two panels.

In the case of Si-NCs (Fig. 31 a) the average value of the ζ-potential distribution is roughly constant (the slope best fit values differ from zero by about 10^{-3} mV/s) for both empty and loaded samples. The intercept values, thus actually the average ζ-potential values, provide (37±1) mV and (32±1) mV for empty and loaded systems respectively. It is worth to notice that in the latter case a smaller value is measured as expected in presence of negatively charged MBT in aqueous environment.

For Si-MNPs (Fig. 31 b) we observe a similar difference between empty and loaded samples at t=0 *s* i.e. (33±1) mV and (30±1) mV respectively. While for empty Si-MNP the ζ-potential average values are basically time-independent, the loaded sample shows a slight but significant increase starting from the suspension preparation time (t = 0*s*). This behaviour is compatible with a progressive MBT release as well as with a greater exposure of MBT biocide in Si-MNP with respect to Si-NC.

ζ-potential results, although preliminary, seem to confirm the different confinement geometry and interaction of the biocide in both synthesized systems, as suggested by Raman spectroscopy.

The thermal stability of silica nanosystems and the amount of the encapsulated biocide have been determined by thermogravimetric tests. In order to take into account the possible contribution to the weight loss due to residual non-hydrolysed/condensed TEOS and cationic surfactant CTAB [127], a preliminary measurement on calcinated neat nanoparticles has been performed for systematic error subtraction.

The thermo-gravimetric curves corresponding to loaded and empty nanosystems show a similar profile in the entire temperature range, with exception of the interval 200 ÷ 300 °C, where a more pronounced weight loss of loaded nanosystems is observed and attributed to the decomposition of MBT. The amount of biocide loading is estimated as 10%w/w in the case of nanocapsules and 8.2%w/w for the nanoparticles.

3.2.1 Release tests of silica nanosystems loaded with MBT

Following previous literature [112], the controlled release of MBT from the two systems has been examined by re-dispersing the loaded nanosystems in water and analysing over the time the aqueous phase by means of HPLC. At difference with previous literature [137], all tests have been conducted under weak stirring and without buffer. The rationale behind this choice is to mimic as closely as possible the release conditions in future applications, without enhancing the biocide release through mechanical stirring, or inducing changes in the silica structure due to pH variation led by the buffer.

Practically, the aqueous phase, in which the biocide was released, is sampled with a syringe. The sample is then pressed through a syringe filter and the filtered solution, where only released active is present, is finally analyzed. This method prevents agglomeration and permits immediate determination of the concentration of the active in the entire aqueous phase [71].

Moreover, control release tests in ethanol have been performed, for a fast check of the effective release of the biocide, giving a MBT concentration of 0.6 mM at time zero and of 2.5 mM after 72 hours of extraction for the Si-NCs; and 4.9 mM at time zero and 5.5 mM after 72 hours for the Si-MNPs. The differences in the released amount of MBT confirm that the biocide are encapsulate in two different ways (Fig.32).

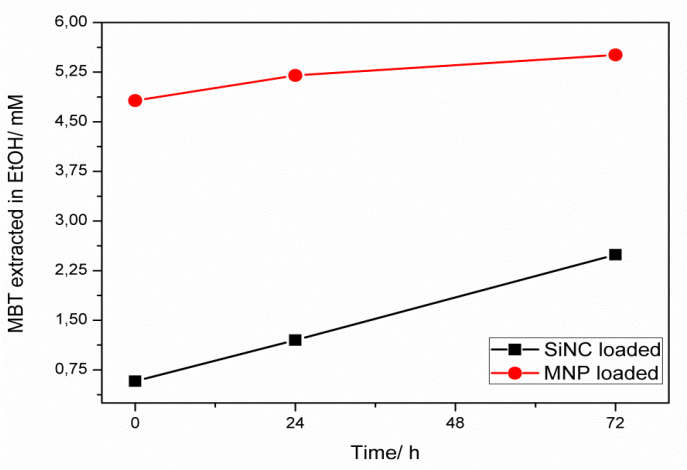

Fig.32 Release profile of MBT in ethanol from Si-NC-MBT (black curve) and Si-MNP- MBT (red curve)

The release profiles obtained in water as a function of time (from 0 to 120 days) for the two nanosystems suggest a different release rate (Fig.33). Bearing in mind that during the release experiment the solvent has not been refreshed, the total amount of biocide released after 4 months is about the same; instead, the release kinetics of the two samples is different. The loaded Si-NC-MBTs shows an almost linear and slow release during the first ≈ 70 days, followed by a much faster release regime at longer times. While the Si-MNP-MBTs shows an initial linear release, faster than in the previous system (0.00092 mM/day, to be compared with 0.00046 mM/day for the Si-NC-MBTs), followed by a saturation at about 0.12 mM.

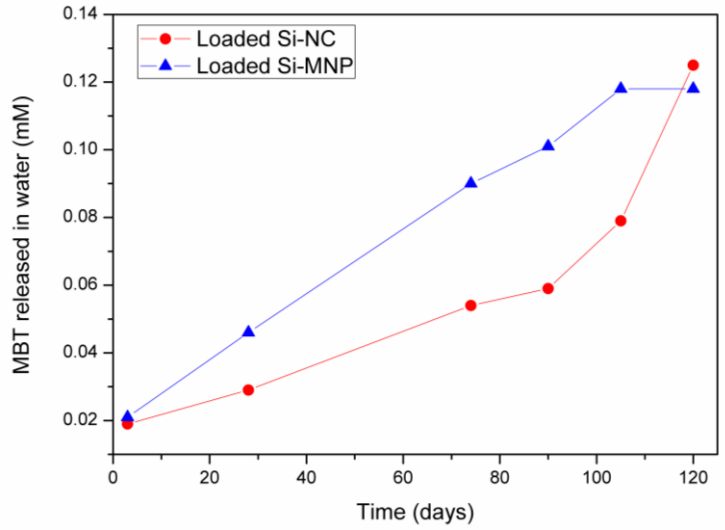

Fig.33 Profiles release of MBT in water from Si-NC-MBT (blue curve) and Si-MNP- MBT(red curve)

The faster initial release for the latter system may be ascribed to a more direct contact between the biocide and water, in particular at short time, possibly due to the textural properties (e.g. surface area and average pore volume). Indeed, the release profile of nanocapsules is conditioned by shell and inner core. The shell is obviously the barrier with the purpose of initial reduction of the release of the biocide and preventing absorption of the external medium [71]. This means that the initial permeability must be lower in the shell than in the core and this parameter influence the release profile of the Si-NC in comparison with the release profile of Si-MNP, as showed in the Fig. 33.

In order to definitively verify that the MBT is entrapped into the mesoporous silica nanoparticles, calcinated Si-MNP impregnated by MBT were tested in the same experimental release conditions. Fig.34 shows the complete release of MBT in less than five days. This results underline that the synthesis of Si-MNP leads to a confinement of the biocide into the silica matrix and not to a simple physical adsorption.

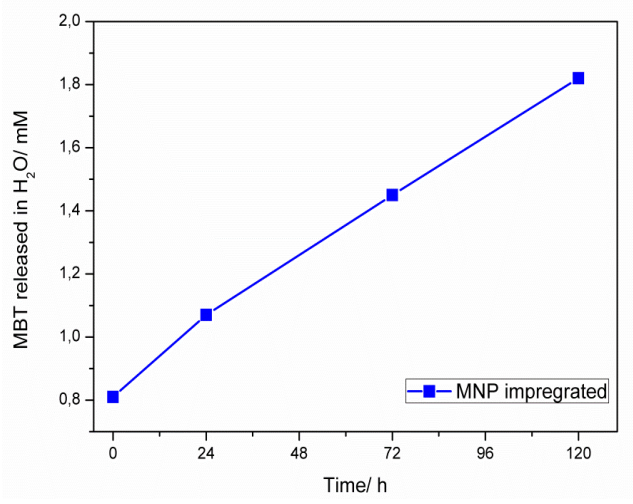

Fig.34 Release profile of MBT physically adsorbed on calcined Si-MNP

3.3 Silica nanosystems loaded with UA and ZS

The encapsulation and the *in situ* entrapment of the usnic acid and the zosteric acid sodium salt were performed working in the same experimental conditions tested for the 2-mercaptobenzothiazole. To promote the encapsulation of usnic acid, reported for the first time, small adjustments, such as the solubilization of UA in ethyl ether through sonication, were performed. While the encapsulation of ZS required, as reported in literature [113], the stabilization of the miniemulsion by the selection of a solvent compatible not only with the ZS but also with the oil phase (ethyl ether).

The *in situ* entrapment is a more versatile confinement method that does not require any adjustments based on the selected biocide, thanks to the absence of the oil phase cosolvent.

As reported for the silica nanosystems loaded with MBT, the morphology and the size are the characteristics studied by SEM analyses.

The SEM micrographs of Si-NC loaded with the environmentally-friendly biocides show their spherical and regular shape. The average particle size, as reported in the histograms of Fig. 35c and 35 d, increases when ZS is loaded during the synthesis. This suggests that the dimension of the biocide molecule shapes the size of the surfactant micelles and thus of the final loaded Si-NCs. We stress that the larger diameter of the loaded particles with ZS and UA, namely (170 ± 20) nm and (163 ± 30) nm compared to (80± 11) nm [112] for the empty ones, is an evidence of successful encapsulation. In the case of ZS encapsulation, we notice also a broadening of the size distribution; this effect, along with the larger average size of the nanocapsules, may be correlated to the use of methanol, influencing the size of the micelles during the O/W miniemulsion step [122].

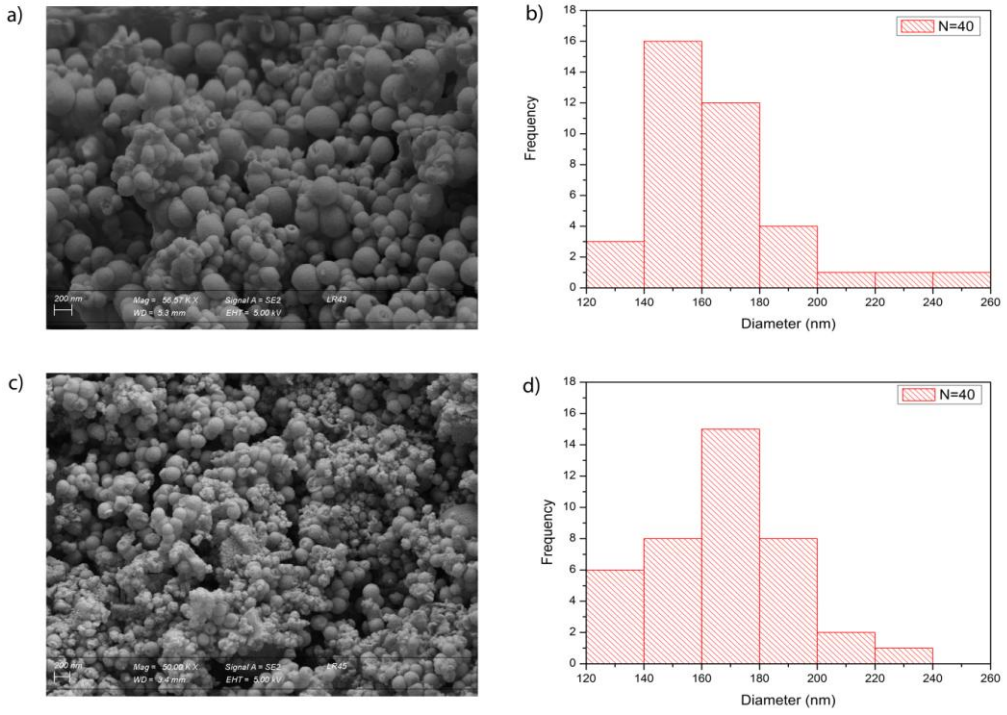

Fig.35 a) SEM micrographs of Si-NCs loaded with UA (Mag=50000); b) the corresponding histogram of particles size; c) Si-NCs loaded with ZS at the same magnifications as a); d) the corresponding histogram of the particles size.

Si-MNPs resulting from the *in situ* entrapment of UA and ZS show a different shape compared to the empty Si-MNPs obtained with the same procedure [112]. In particular, both nanoparticles are larger than the empty one by an order of magnitude and are not spherical but are predominantly hexagonal (Fig.36), being "hexagonal" the common term to describe these shapes [121]. This phenomenology is more evident in the case of mesoporous nanoparticles loaded with usnic acid.

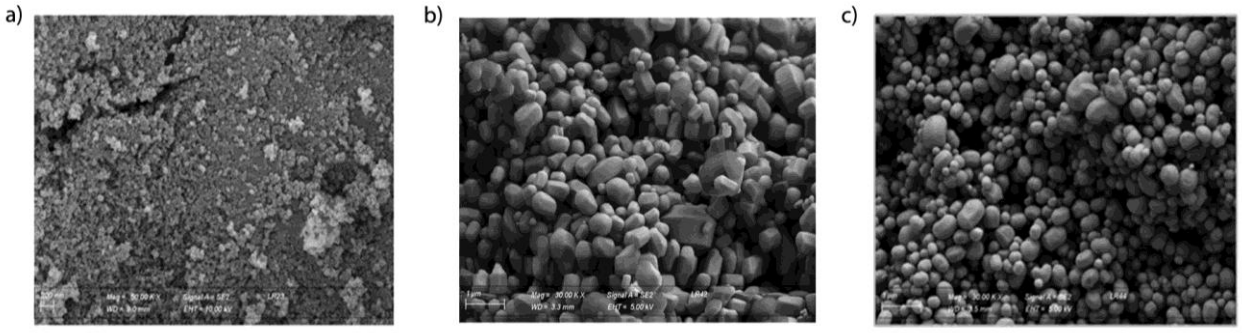

Fig.36 SEM micrographs of Si-MNPs a) empty at Mag=50000, b) loaded with UA and c) loaded with ZS at Mag=30000.

The shape of the Si-MNPs is directly correlated with the spatial array of the cationic surfactant. Once the surfactant concentration exceeds the critical micellar concentration (CMC), the micelles self-assemble in different nanostructures depending on the surfactant concentration [121].
Spherical charged micelles of CTAB (cationic) assume an elongated rod-like (prolate) structure in the presence of additives compounds (e.g. biocides), giving rise to a sphere-to-rod transition.
The packing of molecules in rod-shaped micelles shows a spherical 'end caps' (darker shade) and the cylindrical central part (lighter shade) (see Fig. 37) [138].

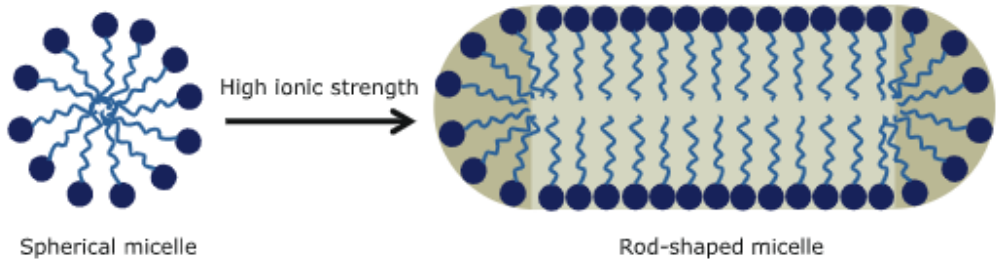

Fig. 37 A schematic representation of the sphere-to-rod transition in charged micelles induced by high ionic strength.

The sphere rod-transition is due to reduced interactions among the charged head groups because of the added compound. Moreover, the head group spacing is reduced in the cylindrical part of the rod-shaped micelle due to attenuation of charge interactions by the added compound.
In the present case, during the micellization process, the biocides act as co-surfactant, thus increasing the effective surfactant amount. This determines the modification of surfactant/biocide spatial array from spherical to rod-shaped micelles, arranged into a roughly hexagonal 3D lattice [139]. Under these conditions, the TEOS condensates around a preformed and energetically favourable hexagonal surfactant/biocide array, as reported in the diagram phase of CTAB (see Fig. 38).

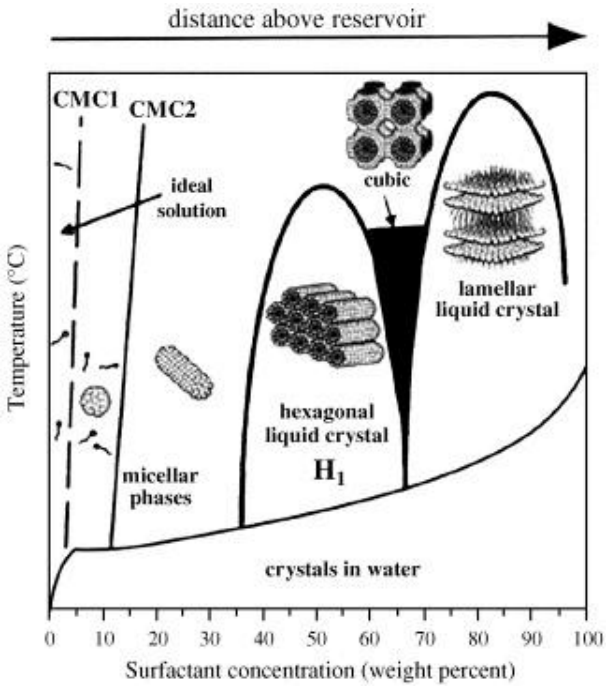

Fig. 38 CTAB phase diagram in water, containing micellar, hexagonal, lamellar, and bicontinuous cubic phases.

The structural transition of cationic micelles depends upon the nature of the additive compound [138]. Due to their greater steric hindrance, usnic acid molecules experience difficulty in fitting between the monomers of CTAB, modifying CTAB micelles more than ZS does. This implies that the usnic acid gives rise to more evident sphere-to-rod transitions than the zosteric sodium salt, at the same concentration [140].

In order to confirm the encapsulation of the biocides, FT-IR and Raman measurements have been performed on the two different silica nanoreservoirs, loaded with UA and ZS, along with the empty silica nanosystems prepared in the absence of biocides, i.e., obtained solely from TEOS and CTAB. The empty samples have been used as control, to evaluate the silica bands, its network vibrations and the presence of residual cationic surfactant (CTAB).

When the biocides are encapsulated within the two nanoreservoirs, the presence of biocides is not confirmed by specific peaks ascribable to the biocides themselves. However, in the case of the loaded Si-MNPs, we observe important shifts of the Si-O-Si asymmetric stretching bands frequency towards lower wavelengths in comparison with the empty nanosystem: from 1055 cm^{-1} to 1029 $cm^{-1}$and to 1045 cm^{-1} for the Si-MNPs loaded with UA and ZS, respectively (Fig. 39 a). Shifts to lower wavenumbers are ascribed to the network deformation needed to accommodate the biocide molecules within the inorganic silica matrix, resulting in larger siloxane rings and Si–O–Si angles along with longer Si–O bond lengths [126-127]. Both UA and ZS play a key role as co-template in cooperation with the cationic surfactant during the micellization step of the Si-MNPs synthesis, consequently, the final silica network, created after the TEOS polymerization at the micellar interfaces, is strongly influenced by their presence. This implies that the *in situ* loading of UA and ZS shapes not only the morphology, as shown above by SEM micrograph, but also the textural properties of the Si-MNPs, as suggested by the FT-IR measurements.

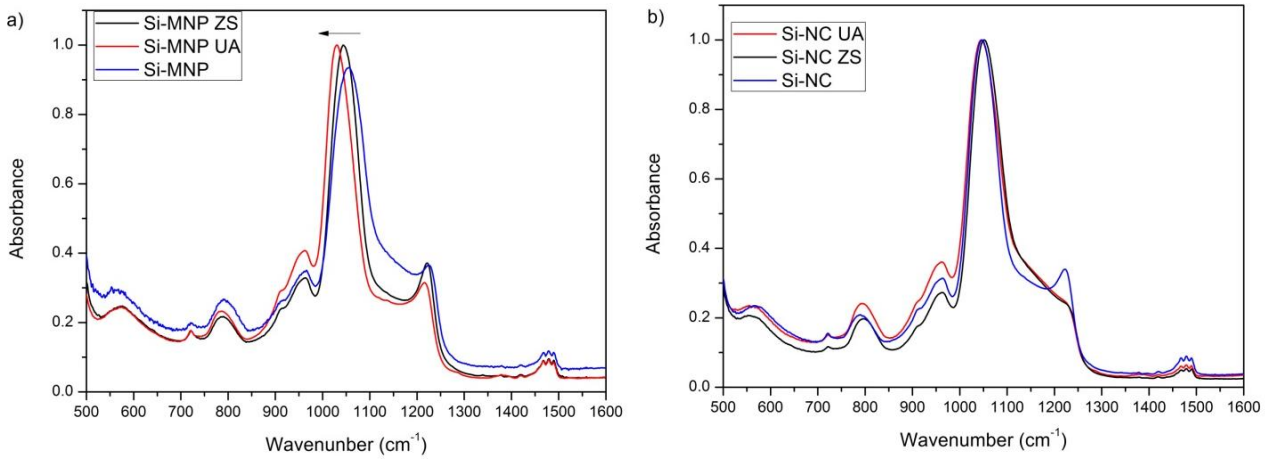

Fig.39 ATR FT-IR spectra of the Si-MNPs (a) and Si-NCs (b) loaded with UA(red),with ZS(black) and empty (blue). The arrow in (a) indicates the shift of the main Si-O-Si band upon biocide loading.

When the UA and ZS are encapsulated into the Si-NCs, no evident modifications of the FT-IR spectra (Fig. 39 b) are visible. Unlike the Si-MNPs case, the presence of the biocides does not induce any significant shift in the region between 850 and 1250 cm^{-1}. This observation suggests that *in situ* loading of different biocides does not determine structural and dynamical changes of the silica matrix of the core-shell containers obtained by evaporation-induced self-assembly procedure. Likely, the presence of diethyl ether as cosolvent minimizes the interference of the biocide molecules with the cationic surfactant during the micellization step. For this reason, the loaded Si-NCs are morphologically and structurally similar to the empty ones, as shown by SEM micrograph and by FT-IR spectra.

In order to verify if the UA and ZS interact with the other synthesis compounds, Raman spectroscopy on the sample powders has been performed. Raman spectra of the two nanosystems both empty and loaded are reported in Fig. 38 and 39, respectively. Here we discuss only the 200–1800 cm^{-1} region of the spectra: this is indeed the fingerprint region of the loaded nanosystems, which may be sensible to the presence of the biocides. The detailed assignment of all the bands of the biocides, the cationic surfactant and the silica structure reported in the literature [36-38], will guide our interpretation of the experimental spectra.

In the Raman spectra of the two nanosystems loaded with usnic acid, some bands at low wavenumber (532 and 600 cm^{-1}) are ascribable to this lichen compound and are clearly identifiable (see Fig. 40). The bands in the region between 1550 and 1700 cm^{-1} are ascribed to quadrant ring stretch of the aromatic methyl ketone and the conjugated cyclic ketone group, respectively. Here, it is possible to assign the conjugated cyclic ketone group to the 1698 cm^{-1} band. Conjugation, electron donating ring substituents and possible intra-molecular hydrogen-bonding, all contribute to the aromatic methyl ketone peak at 1624 cm^{-1}[141-142]. Moreover, Raman spectrum evidences also the presence of residual cationic surfactant (CTAB), covering some biocide bands, namely the bands at 1285 and 1321 cm^{-1}.

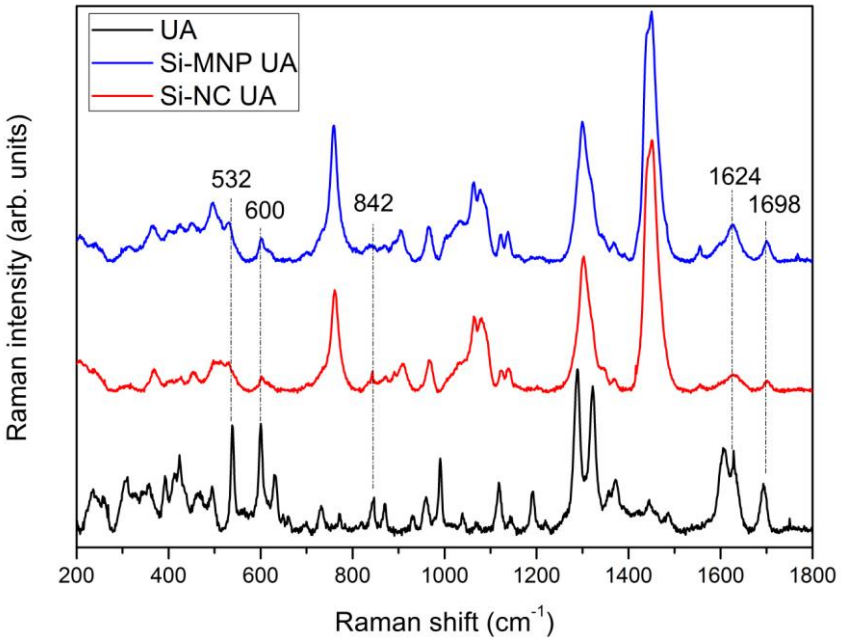

Fig.40 Raman spectra of silica nanocontainers loaded with UA compared with those of the pure biocide.

The encapsulation of the zosteric acid sodium salt is confirmed also by the Raman measurements, reported in Fig.41. The vibrational contribution of the zosteric acid sodium salt is detectable through a few bands because of the vibrational contribution of the CTAB. In details, the band at 1163 cm^{-1} is associated to the symmetric stretching vibrations of the SO_2 group and to the in-plane CH bending [143]. The strong band at 1250 cm^{-1} is related to the asymmetric stretching vibrations of SO_2 group and to C-O stretching. The C=C stretching is evident at 1604 cm^{-1}. At 1622 cm^{-1} we can observe phenyl ring deformation and C=O stretching [144-145].

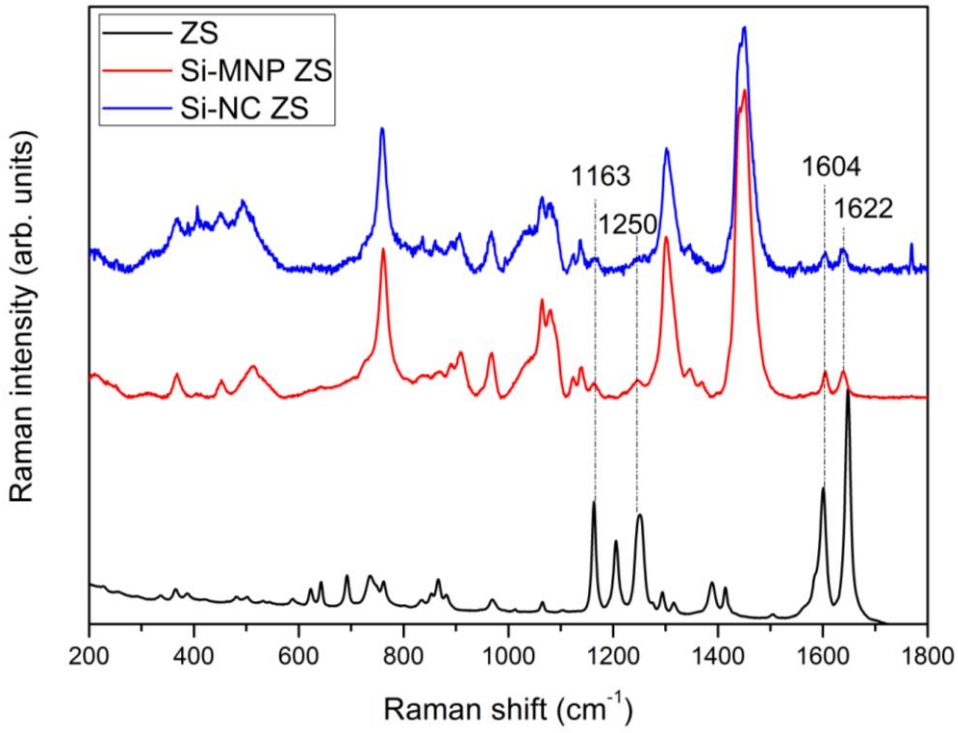

Fig.41 Raman spectra of silica nanocontainers loaded with ZS compared with those of the pure biocide.

The textural properties of empty and loaded Si-MNPs and Si-NCs, before and after calcination at 550 °C for 5 h, have been evaluated based on adsorption-desorption isotherms of N_2, as reported in Figs. 42 and 43. BET surface area, BJH pore volume and BJH Pore size are summarized in Table XVI.

Table XVI Surface area (S.A.), total pore volume (BJH P.V.), and pore size (BJH P.S.) of samples as prepared (empty), loaded or calcined.

Sample	**BET S.A.** m^2g^{-1}	**BJH P. V.** cm^3g^{-1}	**BJH P.S.** nm
Si-MNP	960	0.71	3.9
Si-MNP UA	60	0.04	3.1
Si-MNP ZS	118	0.07	3.1
Si-MNP UA CALC	1021	0.78	3.3
Si-MNP ZS CALC	1007	0.76	3.3
Si-NC	935	1.64	3.9
Si-NC UA	254	0.27	3.9
Si-NC ZS	315	0.24	3.8
Si-NC UA CALC	907	0.61	3.6
Si-NC ZS CALC	780	0.53	3.6

The N_2 adsorption and desorption isotherms of empty Si-MNPs and Si-NCs, are very similar each other (Fig 42 a and 43 a) and the corresponding BET surface areas are 960 m^2g^{-1} and 935 m^2g^{-1}, respectively. By IUPAC classification, these isotherms are classified as type IV with a H1 hysteresis loop, characteristic of mesoporous materials having a narrow distribution of uniform mesopores [146]. The isotherms show two steps of capillary condensation at high $p/p^0 = 0.9$ and at a low $p/p^0 = 0.3$, with hysteresis characteristic of mesopores with cylindrical shape [147]. The addition of UA and ZS in the Si-MNPs induces a strong decrease in the amount of adsorbed N_2, corresponding to BET surface areas of 60 and 118 m^2g^{-1}, respectively (Table XVI). The isotherms of both loaded samples, reported in Fig 42 b, are similar to the empty ones, with the two steps of capillary condensation. The encapsulation of the biocides into the Si-NCs causes a decrease of the BET surface areas from 935 m^2g^{-1} of the empty Si-NCs to 254 m^2g^{-1} and 315 m^2g^{-1} of the systems loaded with UA and ZS, respectively. The isotherms of loaded Si-NCs, reported in Fig 43 b, are very similar each other but different from those of the empty Si-NCs, and they are classified by IUPAC of type IV with a H3 hysteresis loop corresponding to wedge-shaped pores formed by the stacking of flaky particles [148].

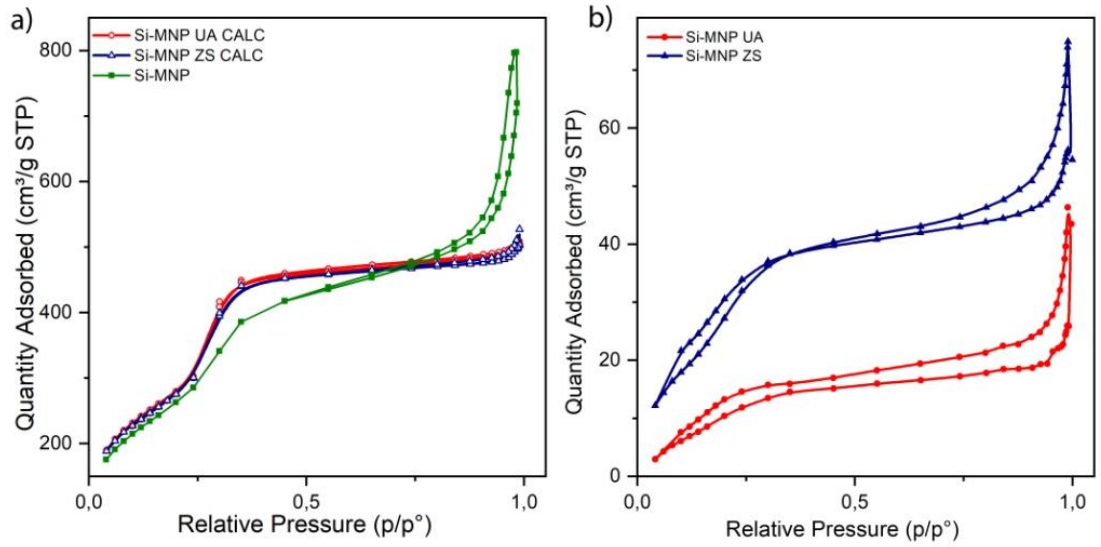

Fig.42 Nitrogen adsorption-desorption isotherms of: a) empty and loaded Si-MNPs after the calcination; b) loaded Si-MNPs.

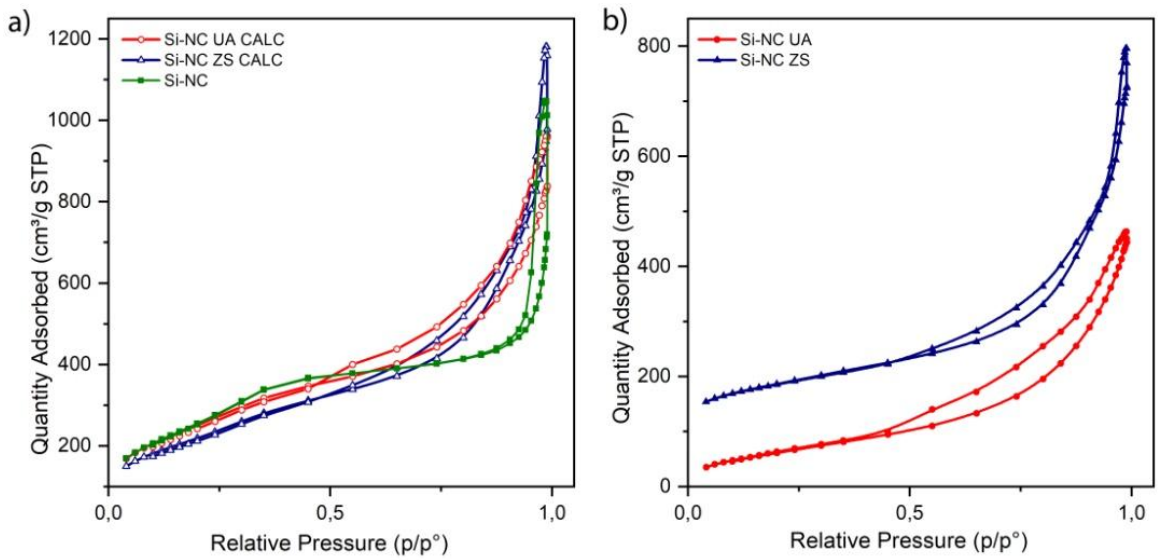

Fig.43 Nitrogen adsorption-desorption isotherms of a) empty and loaded Si-NCs after the calcination; b) loaded Si-NCs.

In order to evaluate if the thermic pre-treatment with He affects the BET measurements, we have analysed both loaded nanosystems after calcination. The isotherms of the loaded Si-MNPs, after the calcinations, are similar to the empty one, as reported in the Fig.42 a. The BET surface area and total pore volume increase in comparison with the empty Si-MNPs, as reported in Table XVI. The BJH pore size distributions of both calcined Si-MNPs show a monomodal profile with a very narrow peak centered at 3.3 nm (Fig. 43 a). These results indicate that the UA and ZS addition induces a weak modification on the textural properties of mesoporous silica nanoparticles.

After calcination, the isotherms of loaded Si-NCs maintain the type IV profile with the H3 hysteresis (Fig. 42 a). The encapsulation of the ZS induces a higher decrease of the BET surface area in comparison with the UA. ZS encapsulation induces also a decrease of total pore volume. The biocide nature does not affect the BJH pore size distribution that is similar for the two loaded

Si-NCs: in the range 2-20 nm with two maxima at 3 nm and 5 nm (Fig. 44 b). These results suggest that the *in situ* encapsulation of biocides promotes an increase in the number of pores and a decrease in their size, keeping constant the surface area values.

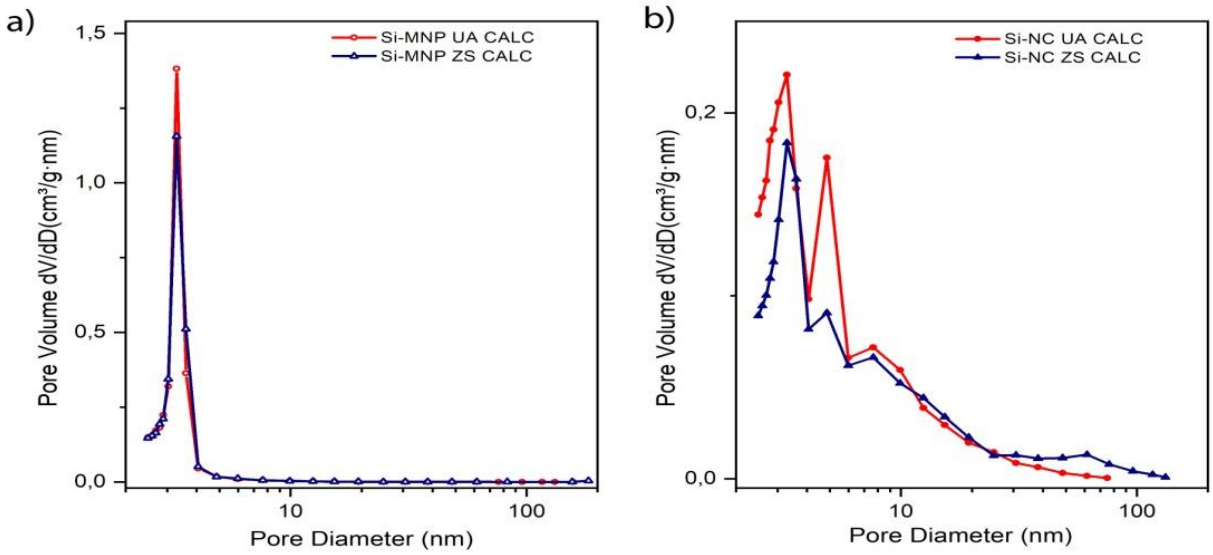

Fig.44 Pore size distribution of calcined Si-MNPs (a) and Si-NCs (b) nanocontainers..

To verify the thermal stability of the silica nanocontainers and to quantify the amount of the encapsulated biocides, thermogravimetric tests have been carried out. The curves (data not shown) corresponding to both silica nanoreservoirs loaded with UA or ZS show a similar weight loss (%) profile in function of temperature as the empty ones, except for the mass reduction around 200 and 300 °C. In this temperature range the weight lost is more pronounced and is attributed to desorption of temperature degradated biocides. It is interesting to use the difference of mass loss between the loaded and empty Si-MNPs to estimate the amount of biocide loading: these amounts to 6.7% and 7.8% for the Si-MNPs loaded with UA and ZS, respectively. In the case of Si-NCs the loading capability is lower compared to the mesoporous nanoparticles, and we find 1,2 % and 2,1 % for in the case of UA and ZS, respectively.

3.3.1 Antifouling efficacy tests

This PhD thesis is part of the project SUPERARE[4], financed by the Lazio region, focused on the development of a multifunctional coating, as well as on the *in situ* test of the multifunctional coatings performance (durability, self-cleaning and antifouling efficacy).
For this reason, before starting with the antifouling efficacy tests of the coating, the nanocontainers were *in vitro* tested.
Antifouling efficacy of developed silica nanosystems was assessed against biodeteriogens growing on outdoor surfaces of roman monuments. The biological patina was collected from Aurelian Walls (Rome, Italy), selecting an area where biological patinas, representative of the most common biodeterioration patterns, were widely spread (Fig.45). The material for the tests was obtained by gently brushing the blackish biofilm covering the bricks in North expositions by means of a sterile scalpel. Such material was then stored in sterile flasks and observed by optical microscopy with an immersion objective at 100-magnification (Olympus BX41), following the procedures in UNI 10923 [148]. The characterization of the photoautotrophic microorganisms was carried out at genus level using the analytic keys of Guiry and Guiry [149].

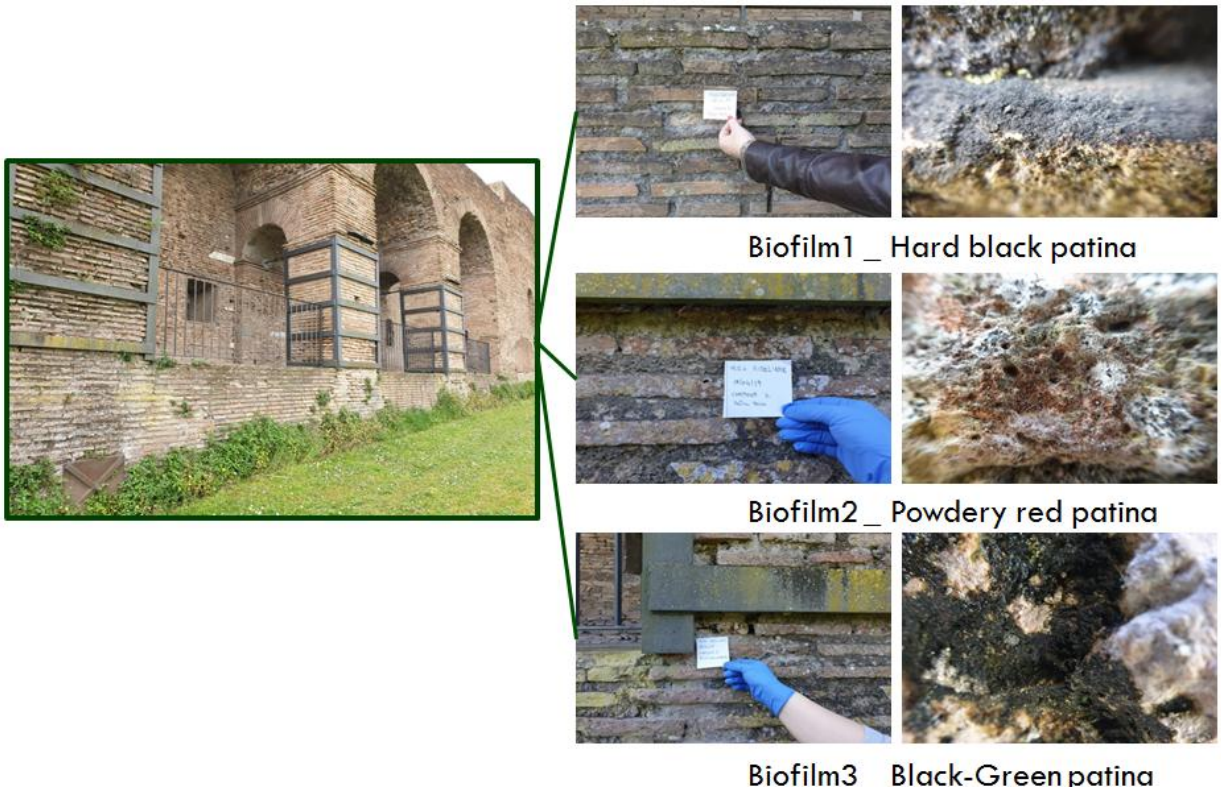

Fig. 45 Sampling of biofilm present in situ (Aurelian Walls, Rome, Italy)

The biopatina, sampled from the Aurelian walls in Rome, was mainly composed by the filamentous and coccoids cyanobacteria of the genera, *Gloeocapsa* and *Chroococcus*, and in a lesser extent by green algae and meristematic fungi (Fig.46).

[4] Super-particelle per rivestimenti autopulenti e antivegetativi a rilascio lento

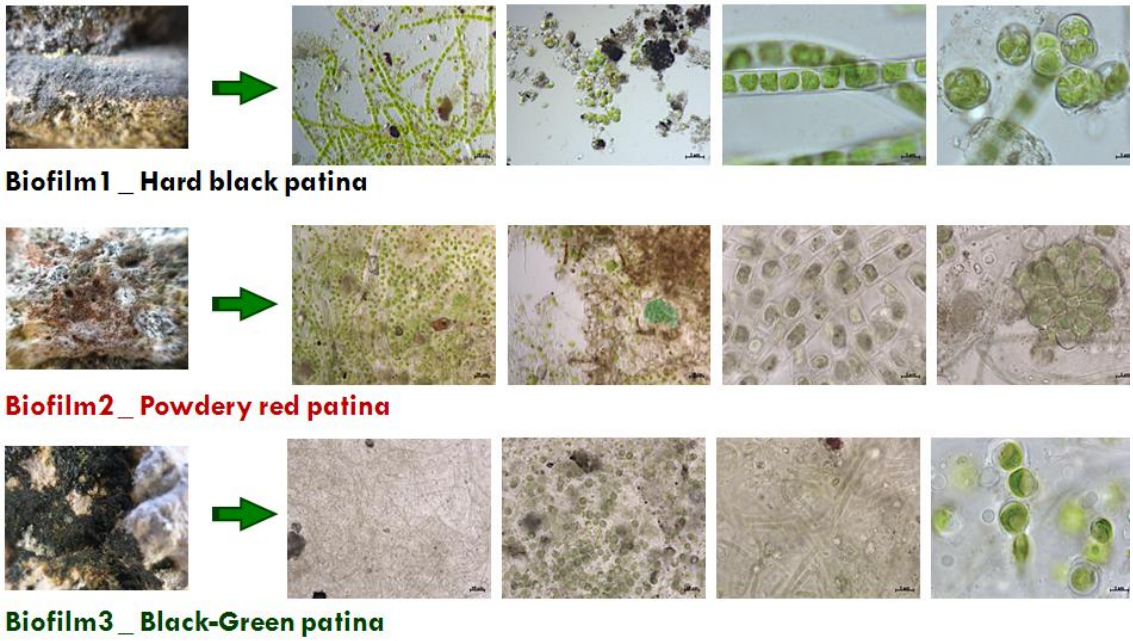

Fig. 46 Identification and characterization of the biological communities

Adapting the experimental protocol from Gazzano *et al*. [151], the organisms were cultured in BG-11 [5]liquid medium (Sigma-Aldrich) at 25°C in conditions of natural sunlight. Twelve tests were then carried out, preparing for each biocides (MBT, ZS and UA) and for each nanosystems (Si-NC and Si-MNP), a culture in triplicate with 3 mg of nanocontainers loaded with the biocide, added to 1 ml of BG-11 liquid culture. The amount of encapsulated biocide was of 0.01 mg/ml.

The effectiveness of the antifouling powder was evaluated after 90 days, by optical microscopy observations. The control and the treated cultures were observed under visible light and in autofluorescence. The fluorescence was detected under an Axio-Imager M1 (Zeiss, Jena, Germany), equipped with a filter at 480-426 nm.

In vitro cultures exposed to the nanoparticles, after 90 days, show a high antifouling activity associated with a slight biocidal activity. This is confirmed by direct observations under stereomicroscope of the treated cultures, which highlighted the absence of microbial growth after 90 days (Fig. 47 a).

Moreover, the optical microscopy observations under visible light, shows a decrease in the production of photosynthetic pigments, related to the reduced vitality of the photosynthetic microrganisms (Fig. 47 b). At last, a reduction of the autofluorescence of the treated photosynthetic organisms has been detected (Fig. 47 c-d) [152-153].

The fluorescence images of treated organisms highlight also the death of some cells through the loss of fluorescence (Fig.47 d). Our preliminary results show that the antifouling nanosystems are effective against photosynthetic microrganisms, such as algae and cyanobacteria, while meristematic fungi, which are really resistant to biocidal treatment, are not affected.

[5] $NaNO_3$1.5 g; $K_2HPO_4$0.04 g; $MgSO_4 \cdot 7H_2O$0.075 g; $CaCl_2 \cdot 2H_2O$0.036 g; Citric acid0.006 g; Ferric ammonium citrate0.006 g; EDTA (disodium salt)0.001 g; $Na_2CO_3$0.02 g; Trace metal mix A51.0 ml; Agar 10.0 g; Distilled water1.0 L

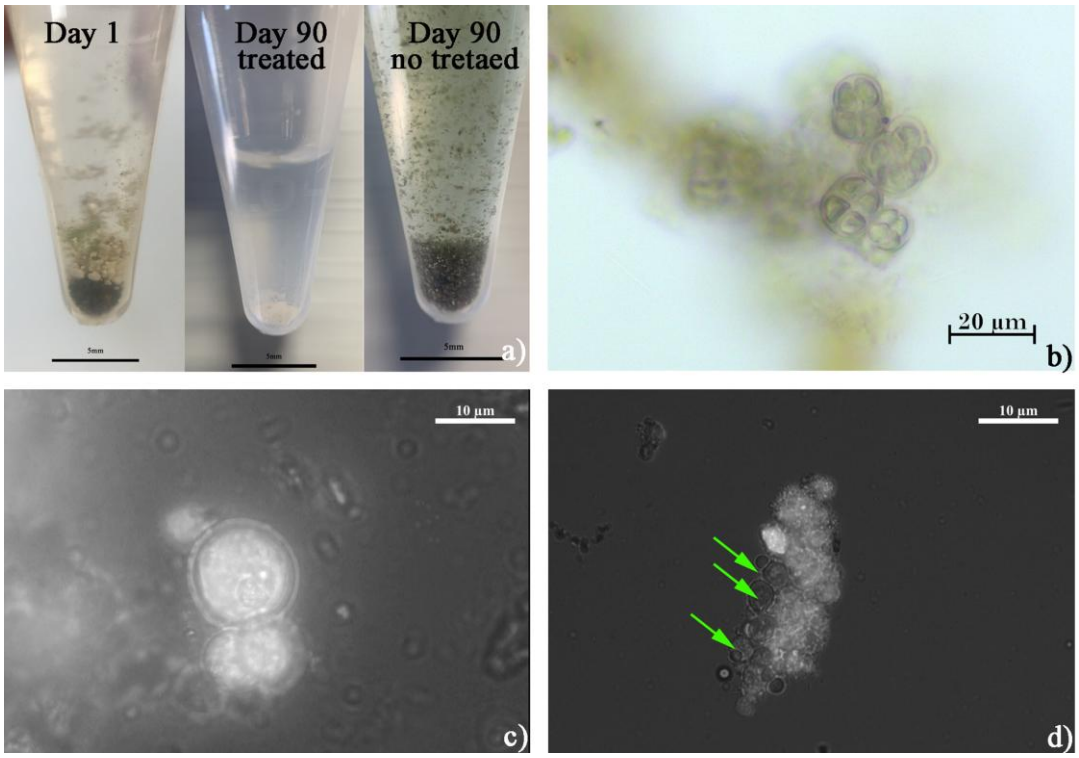

Fig. 47 Antifouling in vitro tests. a) Stereomicroscope images of treated culture on day 1 and after 90 days; b) Optical microscope image under visible light of treated Gloeocapsa cells, showing the lost of photosynthetic pigments; c), Evident autofluorescence image under optical microscope of untreated culture d) Decrease of fluorescence in treated culture (see arrows).

3.4 Multifunctional coatings

The multifunctional coatings were synthesized following a sol-gel process in which the hydrolysis and polycondensation of TEOS is involved.

Even if TEOS-based coatings are widely applied for the consolidation of decaying stone heritage, it is well know that these materials suffer practical drawbacks, such as crack formation of the gel during the drying phase [99-105]. In order to overcome the known drawbacks of conventional TEOS-based materials, the proposed multifunction coatings have been synthesized combining three different strategies:

1) the addition of nanoparticles,
2) the addition of an non-ionic surfactant (n-octylamina),
3) the modification of the elastic properties of the gel with flexible linear segments of Poly(dimethylsiloxane) hydroxy terminated (PDMS-OH).

Different authors tested the effects of addition of oxide nanoparticles. To quote a few of them, we mention that Miliani et al. [99] have proposed the use of inorganic composites, obtained by loading TEOS-based consolidants with colloidal silica particle. Kim et al. [154] and Mosquera's group have also shown that cracking of the gel network during the drying phase is avoided by the addition of nanoparticles. In this contest, in order to give the antifouling and self-cleaning properties to the TEOS-based coating, two different kinds of nanoparticles were added to the TEOS matrix as filler: the commercial nanoparticles of TiO_2 and, for the first time, the silica nanocontainers (Si-NC and Si-MNP) loaded with MBT (described in the paragraph 2.2). Moreover the n-octylamina was added in order to prevent cracking of the gel; this is achieved by two factors [155]: (1) coarsening of the gel network, which reduces the capillary pressure; and (2) decreasing surface tension, which also reduces capillary pressure [156].

At the moment of writing, the nanosystems loaded with the environmentally-friendly biocides (UA and ZS) were not used as filler into the coating formulations because their antifouling properties are still object of active research.

Moreover, the introduction of PDMS-OH into the coating formulation gives to the TEOS network the capability to resist the stress imposed by capillary pressure. The rubbery behaviour was attributed to the ability of PDMS chains to curl and uncurl in the presence of external stresses since the Si–O–Si angle is between 140° and 160° the two methyl groups on each Si are not-bridging [157].

Summing up, a series of coatings were prepared by mixing TEOS, ethanol, water, n-octylamina and PDMS-OH, with the addition of silica nanocontainers (Si-NC and Si-MNP loaded with MBT) and/or TiO_2 in the starting sols.

The coatings have been painted on plastic Petri dishes and examined after drying. Within the series shown in Table XVII, dry coating (C) without nanoparticles is colourless and transparent. The incorporation of nanoparticles into the sol changes the chromaticity of final coatings: we notice

whitening of the charged coatings, of intensity depending on the type of nanoparticle and their concentration. In particular, the addition of TiO_2 nanoparticles induces a whitening of the coatings with a decrease of transparency (first raw of Table XVII). The coatings with Si-MNP maintain a good level of transparency with poor cracks. From the optical point of view, the reasonable amount of nanoparticles is 0.1% (w/v) and the best systems seem to be the coatings added with Si-MNP. The smaller size of Si-MNP in comparison with Si-NC allows the dispersion of these nanocontainers into the coating matrix, reducing the optical effects correlated with the formation of aggregates.

Table XVII Hybrid coatings after drying under laboratory conditions for different concentration of Si-NC/Si-MNP and TiO_2

C	**C_1%TiO_2**	**C_2%TiO_2**
	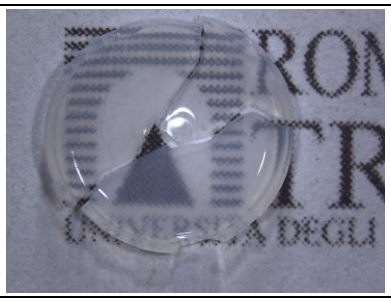	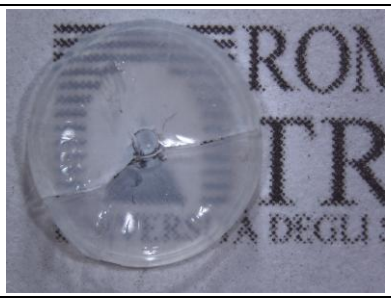
C	**C_1%Si-NC**	**C_2%Si-NC**
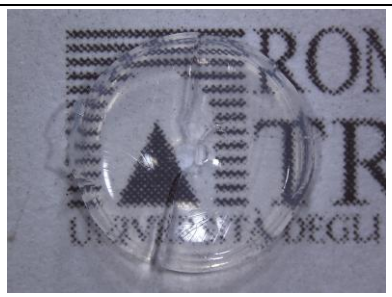		
C	**C_TiO_2/Si-NC**	**C_2_TiO_2/Si-NC**
		
C	**C_1%Si-MNP**	**C_2%Si-MNP**
		

C	C_TiO_2/Si-MNP	C_2_TiO_2/Si-MNP
	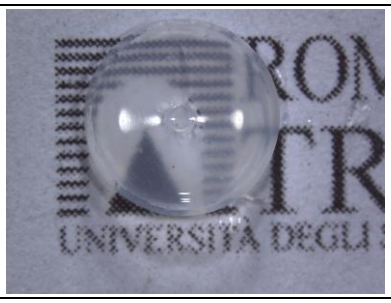	

In order to estimate the effect of the nanoparticles on the drying time of the gel, the weight loss of each sample has been measured. Figure 48 a and b show the weight loss for the sols obtained by the addition of 0.1 % and of 0.2% of nanoparticles, respectively. The weight loss profiles as a function of time (from 0 to 180 hours) for the four multifunctional coatings suggest different drying rates.

The sample without nanoparticles show the faster drying rate: their weight reaches a plateau after 145 h. Generally, the addiction of the nanoparticles induce an increase of the drying rate, keeping the time constant, indeed the coatings with 0.2% of fillers show a lower weight loss than the coatings with 0.1% of fillers. These trends suggest that the nanoparticles interfere in the sol-gel processes.

Indeed, the sol weight loss is attributed to the evaporation of the solvents and the co-products of the hydrolysis and condensation process. When evaporation is not limited by the external conditions (e.g. gas flow and vapor concentration), the concentrations of evaporating reactants and products vary with depth in the coating thickness. Usually the reactants become more concentrated near the drying surface than in the bulk of the coating. Consequently, the reactions accelerate near the drying surface, and the mean molecular weight of polymeric products near the drying surface rises faster than deeper within the coating [158]. Eventually this leads to gelation of solution near the drying surface before gelation of the deeper strates of the solution.

Even visually, the Si-NCs tend to deposit on the bottom of the coating. The method of application, the low initial density of the coating, the size of the Si-NCs lead to the precipitation of Si-NC on the bottom of the coating with limited effect on the drying rate. While the TiO_2 and/or Si-MNP, characterized by a smaller size than the Si-NC, seem to be more homogenously dispersed in the coatings. This implies a slowing of the evaporation of the solvent and consequently of the drying time of the coating. These observations show that the most promising system seems to be once again the C_TiO_2/Si-MNP. The possible application of this material as a consolidating agent requires that the drying time is not too fast, so to allow penetration of the material inside the stone.

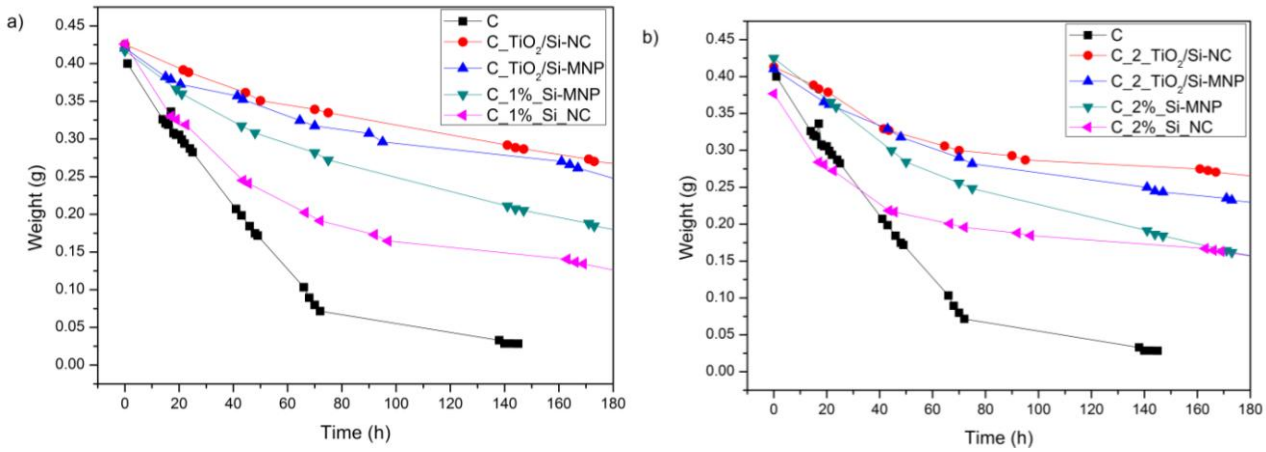

Fig.42 Weight loss during the sol-gel process for the coating with 0.1% (a) and 0.2% (b) of fillers, respectively.

SEM micrographs, collected with InLens detector on the upper surface of the coating, are compared in Table XVIII. All the coatings show a uniform morphology, consisting of microstructured folds, formed by a park of uniform spheres with a size around 13-15 nm. These microstructures do not reflect the morphology and the size of the added nanoparticles. Likely because the TEOS-based matrix and the PDMS are deposited on the nanoparticles covering them.

However, these micrographs show a variation of the roughness of the coating as a function of the type of added nanoparticles. It is possible to correlate the drying rate, quoted above, with the roughness of the coatings: coatings with lower drying rate show less and deeper folds. The rate of evaporation of the solvent, quoted above, shapes the roughness of the coatings surface.

Table XVIII SEM micrographs at different magnification of the samples added with silica nanoparticles and silica nanoparticles and TiO_2

Sample	100 KX	220 KX
C_1%_Si-NC	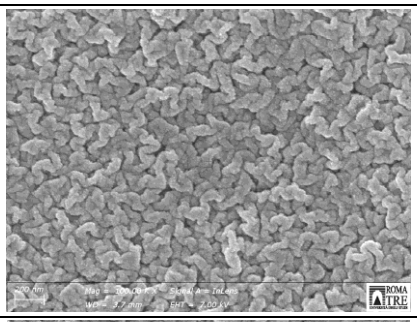	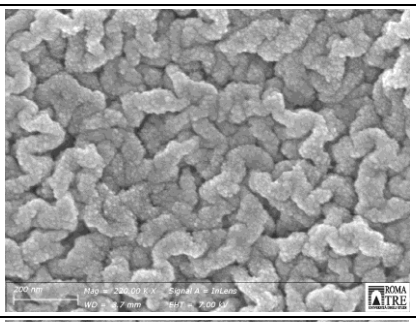
C_2%_Si-NC	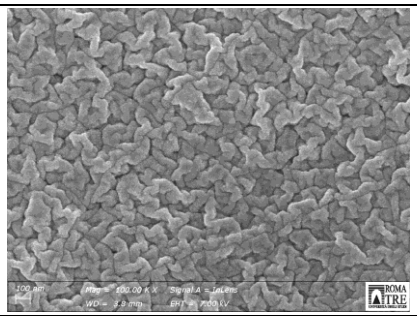	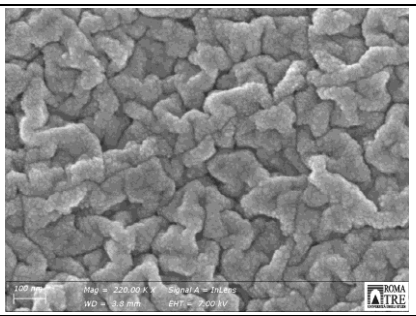

C_TiO_2/Si-NC	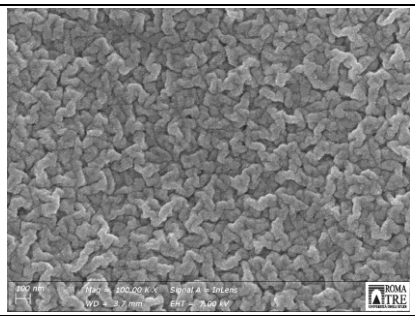	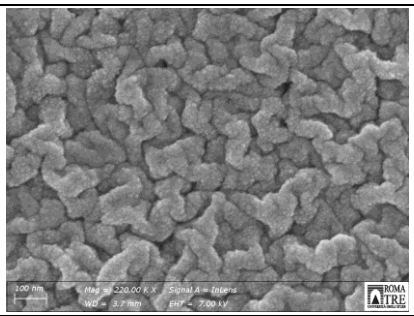
C_2_TiO_2/Si-NC	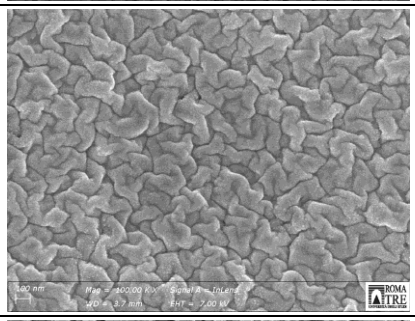	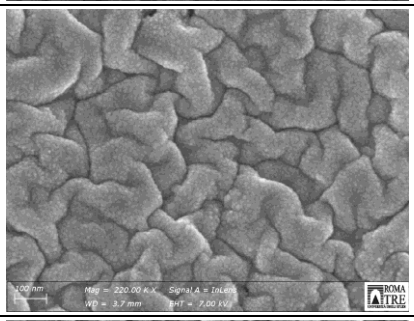
C_1%_Si-MNP	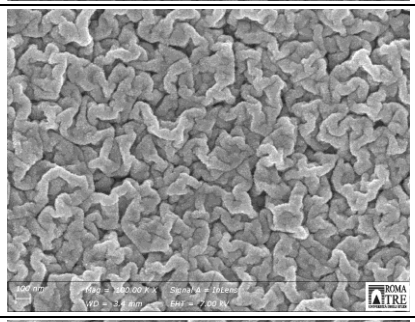	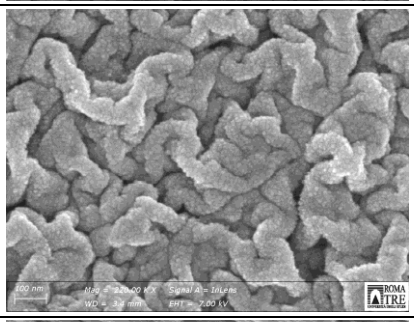
C_2%_Si-MNP	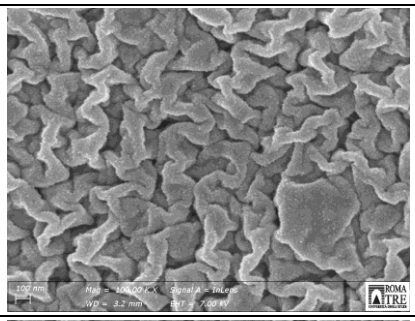	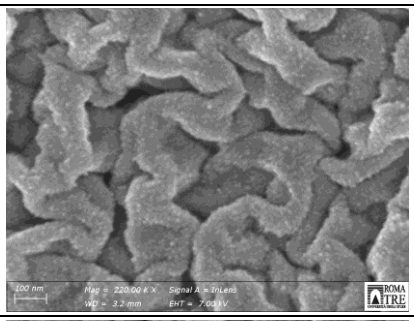
C_TiO_2/Si-MNP	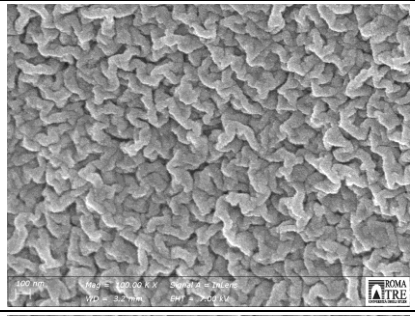	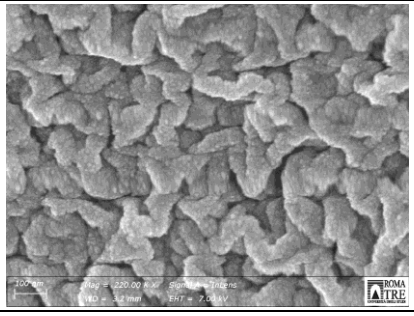
C_2_TiO_2/Si-MNP	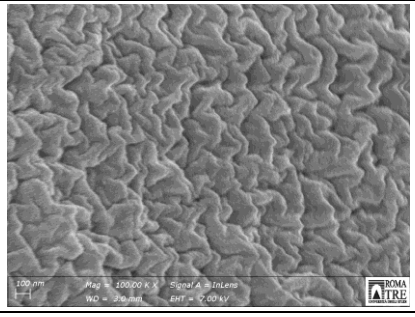	-

In order to investigate the textural properties of the hybrid coatings, N_2 adsorption-desorption isotherms were obtained for the samples added with 0.1% of nanoparticles because these samples show promising optical properties and interesting drying rates. The corresponding textural data obtained are given in Table XIX.

All analyzed coatings show type IV adsorption isotherms, with a H1 hysteresis loop with parallel and nearly vertical branches (see Fig.49 a). This hysteresis is typically ascribable to materials consisting of agglomerated particles or compacted clusters of spherical particles. This loop is more evident for the coatings loaded with TiO_2 nanoparticles. These isotherm profiles suggest that the proposed coatings are a network of silica nanoparticles and that the fillers (Si-NC/Si-MNP and TiO_2) are embedded and integrated in the porous structures [159].

Table XIX Surface area (S.A.), total pore volume (BJH P.V.), and pore size (BJH P.S.) of samples added with 0.1% of nanoparticles.

Sample	S.A (m^2g^{-1})	BJH P.V. (cm^3g^{-1})	BJH P.S. $P/P^0 < 0.60$ (nm)
C	440	0.70	8.4
C_1%Si-NC	481	0.75	5.9
C_1%_Si-MNP	475	0.76	6.4
C_1%_TiO_2/Si-NC	489	0.67	6.3
C_1%_TiO_2/Si-MNP	488	0.76	5.8

The BET surface area of empty coating is 440 m^2g^{-1}, whereas for all sample with the addition of silica nanodevices and/or TiO_2 nanoparticles, the BET surface area is around 480 m^2g^{-1}. In fig. 49 b the peak of sample C is narrow in the range between 9-10.5 nm and shows a peak centered at 8.4 nm. The addiction of Si-NC/Si-MNP and/or TiO_2 reduces the pore size from 8.4 nm to 5.9 nm. The addition of the nanoparticles modifies the pores size of the silica network (coatings). Moreover, the average of total pore volume is unchanged and remains in the range 0.67-0.76 cm^3g^{-1}. These results suggests that the nanoparticles are integrated into the coating matrix, inducing a reduction of BET surface area of about 10 % and of the pore size of about 30 % in comparison with the empty coating. The diameters of the two different silica fillers determine the properties of the coatings. When the TiO_2 nanoparticles are added in to the coating formulations, the differences in the textural properties between the coating loaded with Si-NC and Si-MNP are reduced. TiO_2 nanoparticles induce an increase in the total pore volume in the coating loaded with Si-NC. This implies that the TiO_2 nanoparticles work in synergy with the Si-NC, improving the textural properties of the final product. On the contrary, the total pore volume values are unaffected because the amount of mesopores increases [160].

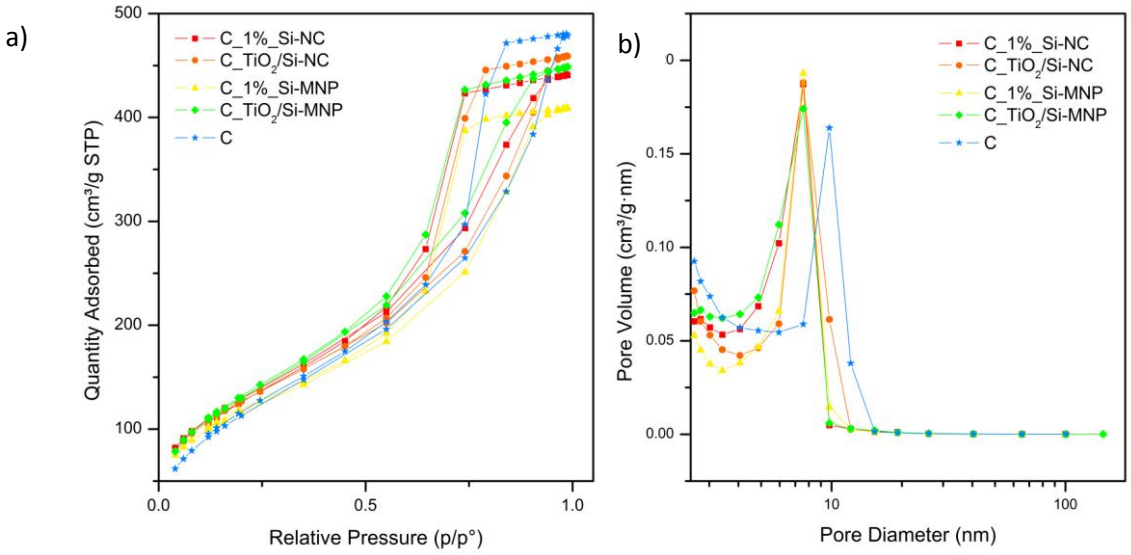

Fig.49 a) Nitrogen adsorption-desorption isotherms and b) BJH pore size distribution for the hybrid coatings under study.

Structural characterization of dried coatings has been carried out by means of Fourier Transformed Infrared Spectroscopy. FTIR spectra of the coatings under study are shown in Figs. 50, 51, 52.

The infrared spectra have been normalized to the band corresponding to the vibration of Si–O–Si (~1050 cm^{-1}), the most intense band for each spectrum. The spectra show a few bands that are unequivocally assigned to the organic fraction in the high frequency range, namely PDMS-OH. Especially, the band at 2907 cm^{-1} corresponds to the symmetric stretching vibration of the C-H bonds whereas the bands at 2929 cm^{-1} and 2964 cm^{-1} are assigned to the asymmetric stretching vibration of the C-H bonds in CH_2 and CH_3 groups, respectively [161].

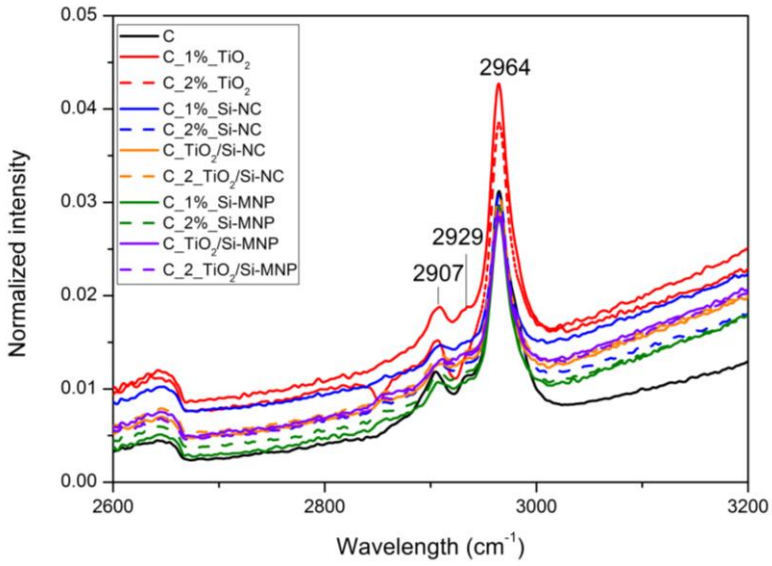

Fig.50 Infrared spectra of all the samples in the range between 2600 and 3200 cm^{-1}

The symmetric bending vibration of CH_3 groups in PDMS-OH contributes to an sharp band centered around 1260 cm^{-1} [162-163]. The band at ~798 cm^{-1} is assigned to the rocking modes of methyl groups (Si-(CH3)) bonded to oxygen and to a silicon atom (Fig. 51).
The band at 850 cm^{-1} is assigned to the copolymerization reaction between Si–OH groups of hydrolyzed TEOS and Si–OH groups of PDMS molecules [164] (Fig. 45). This shows that PDMS is covalently bonded to silica particles, confirming that the copolymerization of PDMS and TEOS is effective and homogeneous organic–inorganic hybrid coatings are created.

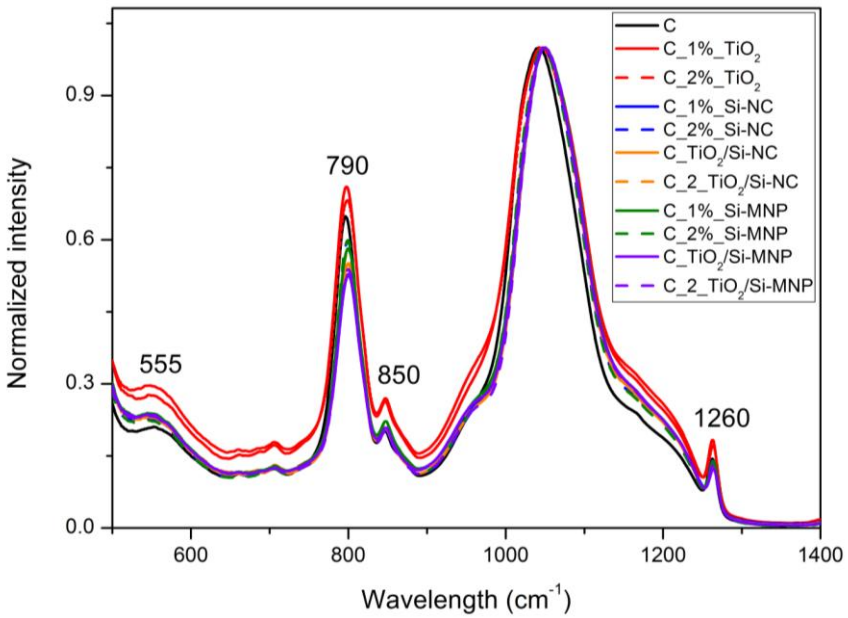

Fig.51 Infrared spectra of all the samples in the range between 500 and 1400 cm^{-1}

The most intense band of the infrared spectra is composed by the contribution of several vibration modes of siloxane bonds, with the main bands between 1000 and 1250 cm^{-1} associated with the sequential Si-O stretching mode of the Si-O-Si network. The deconvolution of the large band centered at 1050 allows to distinguish the 1020 cm^{-1} band corresponding to well known ν(Si–O–Si) vibration of PDMS chains, the asymmetric vibration of 6-fold rings of silica network at 1040 $cm^{-1}$and longitudinal and transversal optical vibration modes of the hybrid network. The band that appears at higher wavenumbers (1050 cm^{-1}) corresponds to the vibration of the network more similar to pure silica while LO mode of the hybrid network is slightly displaced to higher frequencies when organic character increases.
In this contest, a shift of the Si-O-Si asymmetric stretching bands frequency towards higher wavelengths in comparison with the empty coating is observed: from 1042 cm^{-1} to ~1050 cm^{-1} (Fig. 52). These shifts are ascribed to the network deformation needed to accommodate the nanoparticles within the hybrid coating matrix, as reported in table XX. This phenomenology is a good indication that the long-range Coulomb interactions are increased, probably due to a closer distance between interacting species, associated with a lower porosity, as suggested by N_2 adsorption- desorption measurements [165].

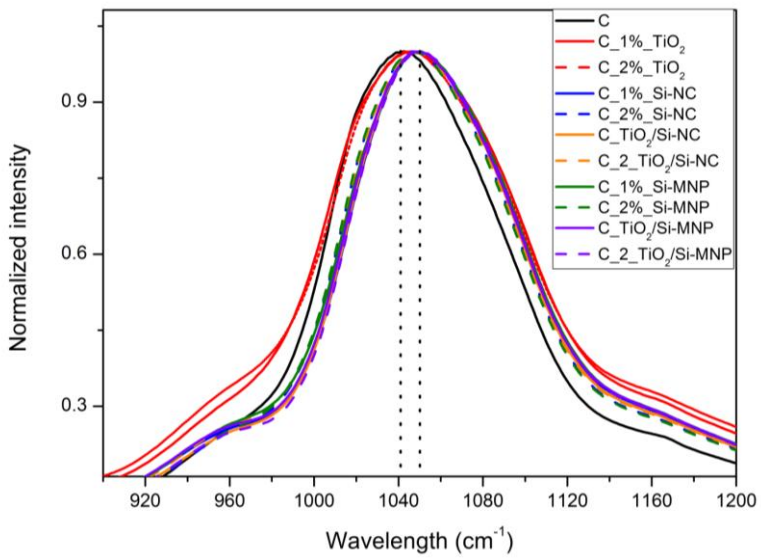

Fig. 52 Detail of the Si-O-Si infrared band for the all coatings. The dot lines highlight the shift of the principal component from the empty coating to the coating with nanoparticles.

As reported in table XX, the position of the band at ~555 cm^{-1}, assigned to a coupled mode in four-member siloxane rings, $(SiO)_4$ changes from a maximum of 555 to a minimum of 543 cm^{-1}. This variation provides a qualitative indication that the proportion of these units changes with the type and the amount of added nanoparticles [166].

Table XX Shift and assignments of the bands observed in the spectra of the coatings.

Sample	**δ Si-O-Si** in SiO_4 (nm)	**ν_{as} Si-O-Si** in SiO_4 and SiO_6 (nm)
C	555	1042
C_1%_TiO2	550	1046
C_2%_TiO2	552	1047
C_1%_Si-NC	550	1046
C_2%_Si-NC	550	1050
C_TiO2/Si-NC	543	1050
C_2_TiO2/Si-NC	549	1050
C_1%_Si-MNP	550	1046
C_2%_Si-MNP	552	1050
C_TiO2/Si-MNP	550	1048
C_2_TiO2/Si-MNP	552	1051

In order to evaluate the chromatic stability of the coating over time, the total colour variation (ΔE^*) of the samples has been measured at 0 time[6] and after 20, 40 and 60 days.

[6] It has been considered as time 0, when the coating reached constant weight.

All the coatings show a ΔE^* below the perceived threshold. The chromatic feature of the coating does not change during time, regardless the type and quantity of nanoparticles added as filler. The absence of any aesthetic changes, such as chromatic variation, is one of the main prerequisites needed for the application of these coatings on stones treatments.

The chromatic feature of the coating does not change during time regardless the nanoparticles added as filler. The absence of any aesthetic changes, such as chromatic variation, is one of the main prerequisite needed for the application of these coatings on stones treatments

Chapter 4

Conclusion and future prospective

This research project presents the synthesis and characterization of innovative antifouling nanodevices for the development of a self-cleaning multifunctional coating for the conservation of cultural heritage stone materials.

Two synthesis procedures have been developed and optimized, working on sol-gel method coupled with the miniemulsion polymerization, in order to exploit the complementary release properties provided by the silica nanocapsules (Si-NC) and the mesoporous nanoparticles (Si-MNP) loaded with three different biocides. In particular, a commercial biocide used in several different applications (2-mercaptobenzothiazole (MBT)) and two "green" products, namely zosteric acid sodium salt and usnic acid were encapsulated and *in situ* entrapped. These latter two have been tested in accordance to the pro-ecological trends and EU regulations, as environmentally-friendly biocides.

Both Si-NC and Si-MNP loaded with the MBT have regular and spherical morphology, with a different mesoporosity. Size and textural properties of the two nanodevices are influenced by the synthesis procedure (e.g. presence of co-solvent, and MBT loading). In particular, the two nanoparticles have different size, with a factor ~4 between their diameters. The MBT content of the final products is similar, but the release in water within the first 3 months is slower for the Si-NC system. The different size and release properties of the nanosystems are particularly fit to applications as part of protective antifouling coatings for outdoor artefacts. First of all, the size of both nanoparticles is small enough to avoid light diffusion which could change the look of the artefact. Moreover the observed differences in the release rate may be functional to the production of tailored coating products.

In order to check the versatility of the synthesis procedures and to produce a environmentally-friendly fillers for the multifunctional coating, for the first time two innovative environmentally-friendly biocides have been successfully encapsulated and *in situ* entrapped.

Si-NC loaded with both UA and ZS have regular and spherical morphology, although with different mesoporosity. On the contrary, the loading of UA and ZS in the synthesis procedure of Si-MNPs changes the shape of the nanocontainers from spherical to hexagonal. The loading capability is higher in the mesoporous system than in the core-shell system; in addition, the zosteric acid sodium salt seems to be loaded more efficiently than UA. The Si-NCs synthesis protocol seems to be the more versatile, as it does not show correlation between the shape of the final product and the selected biocide. In the case of Si-MNPs synthesis procedure, the loading capability is not affected by the biocides; on the contrary, the morphology and the dimensions of the final product are strongly dependent on the loaded biocide.

In vitro antifouling tests of MBT, UA and ZS confined into silica nanodevices have demonstrated the efficacy and the applicability of these materials to realize innovative environmentally-friendly nanodevices.

The developed synthesis procedures represent a first fundamental approach in the achievement of a multifunctional coating for the anti-vegetative treatment of stone materials.

The proposed biocide encapsulation in nanodevices overcomes the drawbacks of the direct application of the biocides into the coating, as for instance premature release and washing out of the active compound. Indeed, the storage of the biocide into silica nanodevices allows the controlled release over time, the reduction of the total amount of the biocide, the longer durability of the treatment and the reduction of the environmental impact. For these reasons, the addition of nanodevices into the coating formulation instead of the present methods is beneficial and can play a significant role in anti-vegetative frontiers. In order to confer to the TEOS-based coating also self-cleaning properties, we have added commercial TiO_2 nanoparticles to the Si-NC-MBT and Si-MNP-MBT formulations.

In order to improve the mechanical and adhesion properties to the coating we have tested two strategies: 1) the addition of an elasticizer (PDMS-OH) and 2) a non-ionic surfactant (n-octylamine). The elasticizer works in synergy with the nanoparticles to reduce internal tensions and cracking during the sol-gel transition of TEOS. While, n-octylamine enhances the compatibility of the TEOS-based coating with the carbonatic litotype, increasing the versatility of the final multifunctional coatings.

The best results as far as the optical properties (e.g. visual aspect and transparency), the porosity and the absence of cracking are obtained with the following nanoparticles concentrations: 0.05 % w/v of TiO_2 and 0.05 % w/v of Si-MNP-MBT or Si-NC-MBT. The release properties have been tested also within the coating. Overall, this work has demonstrated the capability of innovative multifunctional coating and the versatility of the synthetic procedure in the encapsulation/entrapment of three different biocides.

This study will be completed by testing both the efficacy of the multifunctional coating with the nanodevices loaded with the two “green” biocides and the different litotypes (e.g. bricks, marble and travertine). Future plans also include investigating the photocatalytic activity of the commercial TiO_2 nanoparticles added to the coating and the photocatalytic degradative action on the organic substances contained into the developed product (e.g. n-octylamina and the biocides).

In addition, the application of the multifunctional coatings on the stone materials will be fundamental to study the changes of stone properties after the treatment (e.g. colour changes, porosity and permeability).

Publications

Publications included in this PhD thesis

Papers

1. Ludovica Ruggiero, Laura Crociani, Elisabetta Zendri, Naida El Habra, Paolo Guerriero, *Incorporation of the zosteric sodium salt in silica nanocapsules: synthesis and characterization of new fillers for antifouling coatings, Applied Surface Science* 439 (2018) 705–711.

2. Ludovica Ruggiero, Elisabetta Di Bartolomeo, Tecla Gasperi, Igor Luisetto, Alessandro Talone, Francesca Zurlo, Davide Peddis, Maria Antonietta Ricci, Armida Sodo, *Silica nanosystems for active antifouling protection: nanocapsules and mesoporous nanoparticles in controlled release applications*, *Journal of Alloys and Compounds* 798 (2019) 144-148.

3. Ludovica Ruggiero, Armida Sodo, Mariangela Cestelli-Guidi, Martina Romani, Angelo Sarra, Paolo Postorino, Maria Antonietta Ricci, *Raman and ATR FT-IR investigations of innovative silica nanocontaniers loaded with biocide for stone conservation treatments, Microchemical Journal (2019),* under review.

4. Ludovica Ruggiero, Flavia Bartoli, Maria Rosaria Fidanza, Giulia Caneva, Maria Antonietta Ricci, A. Sodo, *An innovative self-cleaning multifunctional coating with antifouling properties for preserving architectural stone surface, Frontiers*, under review.

5. Ludovica Ruggiero, Flavia Bartoli, Maria Rosaria Fidanza, Eleonora Marconi, Francesca Zurlo, Giulia Caneva, Simonetta Tuti, Elisabetta Di Bartolomeo, Tecla Gasperi, Maria Antonietta Ricci, Armida Sodo, *Encapsulation of environmentally-friendly biocides in silica nanosystems for multifunctional coatings, Applied Surface Science,* under review.

Publication not included in this PhD thesis

Papers

6. Ludovica Ruggiero, Armida Sodo, Fabio Bruni, Maria Antonietta Ricci, *Hydration of monosaccharides studied by Raman scattering*, *J. Raman Spectrosc.* 49 (6) (2018) 1066-1075.

7. Armida Sodo, Ludovica Ruggiero, Stefano Ridolfi, Elisabeth Savage, Luca Valbonetti, Maria Antonietta Ricci*, Dating of a unique six-colour relief print by historical and archaeometric methods,* European Physical Journal Plus 134 (6) (2019) 276.

8. G. Germinario, A. Ciccola, I. Serafini, L. Ruggiero, M. Sbroscia, F. Vincenti, C. Fasolato, R. Curini, M. Ioele, P. Postorino, A. Sodo, *Gel substrates and ammonia-EDTA extraction solution: a non-invasive combined approach for the identification of anthraquinone dyes from wool textiles*, *Microchemical Journal (2019),* under review.

9. Alessandro Talone, Ludovica Ruggiero, Francesca Zurlo, Elisabetta Di Bartolomeo, Davide Peddis, Maria Antonietta Ricci, Armida Sodo**,** *Green silica-coated magnetic nanoparticles for biomedical applications***,** *Applied Surface Science,* under review.

Chapter in book

10. Laura Crociani, Ludovica Ruggiero, *Methods for synthesis of nanocontainers*, in Smart Nanocontainers, Elsevier 2019

List of Tables

List of Figures

Bibliography

[1] G. Torraca, Lectures on Materials Science for Architectural Conservation. Los Angeles: Getty Conservation Institute (2009).

[2] M. D. Jackson, F. Marra, R. L. Hay, C. Cawood, E. M. Winkler. The judicious selection and preservation of tuff and travertine building stone in ancient Rome, Archaeometry, 47 (3) (2005) 485–510.

[3] A. Bourges, K. T. Fehr, S. Simon, R. Snethlage, Correlation between the micro-structure and the macroscopic behaviour of sandstones, Restoration of Buildings and Monuments: An International Journal, 14 (3) (2008) 157–66.

[4] E. Doehne, A. Price Clifford, Stone conservation: An overview of current research. Technical Report. Getty Conservation Institute, Los Angeles (2010)

[5] C.J. McNamara, R. Mitchell, Microbial deterioration of historic stone, Front Ecol Environ, 3(8) (2005) 445–451.

[6] A. Webster, E. May, Bioremediation of weathered-building stone surfaces, TRENDS in Biotechnology 24 (6) (2006) 255-260.

[7] S. Scheerer, O. O. Morales, C. Gaylarde, Chapter 5: microbial deterioration of stone monuments—an updated overview. In: Advances in applied microbiology, Academic Washington, DC, (2009) 97–139.

[8] S. Siegesmund, T. Weiss, A. Vollbrecht, Natural stone, weathering phenomena, conservation strategies and case studies: introduction, Geological Society, London, Special Publications, 205, 1 (2002) 1-7.

[9] A.Z. Miller, P. Sanmartín, L. Pereira-Pardo, A. Dionísio, C. Saiz-Jimenez, M.F. Macedo, B. Prieto, Bioreceptivity of building stones: A review, Science of The Total Environment, 426 (2012) 1-12.

[10] C. C. Gaylarde, L H G. Morton, Deteriogenic biofilms on buildings and their control: A review, Biofouling, 14 (1) (1999) 59-74.

[11] C. J McNamara and R. Mitchell Front, Microbial deterioration of historic stone, Ecol Environ, 3(8) (2005) 445–451.

[12] S. Molin, T. Tolker-Nielsen, Gene transfer occurs with enhanced efficiency in biofilms and induces enhanced stabilisation of the biofilm structure, Curr. Opin. Biotechnol., 14(3) (2003) 255-261.

[13] P.S. Stewart, M.J. Franklin, Physiological heterogeneity in biofilms, Nat. Rev. Microbiol., 6(3) (2008) 199-210.

[14] P. D. Martino, What About Biofilms on the Surface of Stone Monuments?, The Open Conference Proceedings Journal, 7 (Suppl 1: M2) (2016) 14-28.

[15] G. O'Toole, H.B.Kaplan, R. Kolter, Biofilm formation as microbial development, Annu. Rev. Microbiol., 54 (2000) 49-79.

[16] P. Sanmartín, N. Aira, R. Devesa-Rey, B. Silva, B. Prieto, Relationship between color and pigment production in two stone biofilm-forming cyanobacteria (Nostoc sp. PCC 9104 and Nostoc sp. PCC 9025), Biofouling, 26 (2010) 499–509.

[17] S. Golubic, E.I. Friedmann, J.Schneider, The lithobiontic ecological niche, with special reference to microorganisms, J. Sediment. Petrol., 51 (1981) 5-478.

[18] C.A Crispim, P.M. Gaylarde, C.C. Gaylarde, Algal and cyanobacterial biofilms on calcareous historic buildings, Curr. Microbiol, 46(2) (2003) 79-82.

[19] N.A. Cutler, H.A. Viles, S.Ahmad, S.McCabe, B.J. Smith, Algal 'greening' and the conservation of stone heritage structures. Sci. Total Environ., 442 (2013) 152-164

[20] J.J. Ortega-Calvo, M. Hernandez-Marine, C. Saiz-Jimenez, Biodeterioration of building materials by cyanobacteria and algae, Int. Biodeterior, 28 (1991) 165-185.

[21] Mottershead, D.; Lucas, G. The role of lichens in inhibiting erosion of a soluble rock, Lichenologist 32(6) (2000) 601-609

[22] M.A. Coombes, L.A. Naylor, H.A. Viles, R.C. Thompson, Bioprotection and disturbance: Seaweed, microclimatic stability and conditions for mechanical weathering in the intertidal zone, Geomorphology, 202 (2013) 4-14.

[23] A.Z. Miller, P. Sanmartín, L. Pereira-Pardo, A. Dionísio, C. Saiz-Jimenez, M.F. Macedo, B. Prieto, Bioreceptivity of building stones: A review, Science of the Total Environment 426 (2012) 1–12.

[24] G. Caneva, M.P. Nugari, O. Salvadori, Plant biology for cultural heritage: biodeterioration and conservation. Getty Conservation Institute, Los Angeles (2008).

[25] F. Borderie, B. Alaoui-Sossé, L. Aleya, Heritage materials and biofouling mitigation through UV-C irradiation in show caves: state-of-the-art practices and future challenges, Environ Sci Pollut Res, 22 (6) (2015) 4144-72.

[26] C.A. Crispim and C.C. Gaylarde, Cyanobacteria and Biodeterioration of Cultural Heritage: A Review, Microbial ecology, 49 (2005)1–9.

[27] L. Tomaselli, G. Lamenti, M. Bosco, P. Tiano, Biodiversity of photosynthetic microorganisms dwelling on stone monuments, Int.Biodeterior. Biodegradation, 46 (2000) 251-258.

[28] C.C Gaylarde, P.M. Gaylarde, A comparative study of the major microbial biomass of biofilms on exteriors of buildings in Europe and Latin America, Int. Biodeterior. Biodegradation, 55 (2005) 131-139.

[29] D. Pinna Coping with Biological Growth on Stone Heritage Objects: Methods, Products, Applications, and Perspectives, Apple Academic Press (2017).

[30] Biocides Market Report: Global Industry Analysis, 2024". Ceresana. 2018. Retrieved 21 October 2018.

[31] Guidance on biocides legislation - ECHA". echa.europa.eu. Retrieved 13 April 2018

[32] D. Vázquez-Nion, P. Sanmartín, B. Silva, B. Prieto, Reliability of Colour Measurements for Monitoring Pigment Content in a Biofilm-Forming Cyanobacterium, Int. Biodeteriorat. Biodegradat., 84 (2013) 220–226.

[33] S. P. Denyer Mechanisms of action of antibacterial biocides, Int Biodeterior Biodegr., 36 (1996) 227-240.

[34] R. J. Larson, R.M. Ventullo, Acclimation and biodegradation response of natural microbial communities to surfactants. In: Rossmoore H W (ed) Biodeterioration Biodegradation 8. Elsevier Applied Science, New York (1991) 373-374.

[35] M.E. Young, HL. Alakomi, I. Fortune, A. A. Gorbushina, W. E. Krumbein, I. Maxwell, C. McCullagh, P. Robertson, M. Saarela, J. Valero, M. Vendrell, Development of a biocidal treatment regime to inhibit biological growths on cultural heritage: BIODAM, Environ Geol 56 (2008) 631.

[36] R. J. Koestler, O. Salvadori, Methods of Evaluating Biocides for the Conservation of Porous Building Materials,Sci. Technol. Cult. Heritage, 5(1) (1996) 63–68.

[37] J. Walentowska, J. Foksowicz-Flaczyk, Thyme essential oil for antimicrobial protection of natural textiles, Int. Biodeter. Biodegrad., 84 (2013) 407–411.

[38] M.P. Nugari, M.S. D'Urbano, O. Salvadori, Test Methods for Comparative Evaluation of Biocide Treatments, Proceedings of the International RILEM/UNESCO Congress on Conservation of Stone and Other Materials. Ed. M.J. Thiel. UNESCO, Paris, Vol. 2, SPON London, (1993) 565-572.

[39] M. R. Fidanza, G. Caneva, Natural biocides for the conservation of stone cultural heritage: A review, Journal of Cultural Heritage, 38 (2019) 271-286.

[40] S. Lisi, A.M. Ricco, M., Zagari, C. Urzi, On the Efficiency of Biocides against Biodegradative Fungal Strains Isolated from Rock using the Contact Time Technique. In: Proceedings of the 7th International Congress on Deterioration and Conservation of Stone. Ed. J. Delgado Rodrigues; Fernando Henriques and F. Telmo Jeremias. Lisbon, Portugal, Laboratorio Nacional de Engenharia Civil, 453-457.

[41] O. Salvadori, A.E. Charola, Methods to prevent biocolonization and recolonization: An overview of current research for architectural and archaeological heritage, in: A.E. Charola, C. McNamara, R.J. Koestler (Eds.), Biocolonization of Stone: Control and Preventive Methods – Proceedings from the MCI Workshop Series, 2, Smithsonian Institution Scholarly Press, Washington, DC (2011) 37–50.

[42] D. Slaton, K. C. Normandin, Masonry Cleaning Technologies, J. Architect. Conserv, 11(3) (2005) 7–31.

[43] V. B. Rodin, S. K. Zhigletsova, V. S Kobelev, N. A. Akimova, V. P. Kholodenko, Efficacy of Individual Biocides and Synergistic Combinations, Int. Biodeteriorat. Biodegradat, 55 (2005) 253–259.

[44] R. Carrillo-González, M. Araceli Martínez-Gómez, M.C.A. González-Chávez, J.C. Mendoza Hernández, Inhibition of microorganisms involved in deterioration of an archaeological site by silver nanoparticles produced by a green synthesis method, Sci. Total Environ., 565 (2016) 872–881.

[45] J. Walentowska, J. Foksowicz-Flaczyk, Thyme essential oil for antimicrobial protection of natural textiles, Int. Biodeter. Biodegrad., 84 (2013) 407–411.

[46] A.P. Fraise, Historical Introduction. In Russel, Hugo & Ayliffe's Priciples and Pratice of Disinfection, Preservation and Sterilization, Wiley-Blackwell: Hoboken, New Jersey, (2013) 1–4.

[47] B. R. Ranković, Lichen Secondary Metabolites: Bioactive Properties and Pharmaceutical Potential, Springer International Publishing, 2015.

[48] S. Huneck, I. Yoshimura, Identification of Lichen Substances. Springer, Berlin. Ingólfsdóttir, K., 2002. Usnic acid, Phytochemistry, 61 (1996) 729-736.

[49] J.A. Elix, E. Stocker- Wörgötter, Biochemistry and secondary metabolites. In: Nash III, T.H. (Ed.), Lichen Biology, second ed. Cambridge University Press, Cambridge, (2008) 104-133.

[50] I. Oksanen, Ecological and biotechnological aspects of lichens, Applied Microbiology and Biotechnology, 73 (2006) 723-734.

[51] T. Mitrović, S. Stamenković, V. Cvetković, S. Tošić, M. Stanković, I. Radojević, I. Stefanović, L. Čomić, D. Đačić, M. Ćurčić, S.Marković, Antioxidant, antimicrobial and antiproliferative activities of five lichen species, International Journal of Molecular Sciences, 12 (2011) 5428-5448.

[52] K. Molnár, E. Farkas, Current results on biological activities of lichen secondary metabolites: a review, Zeitschrift fur Naturforschung. Section C -Journal of Biosciences, 65 (2010) 157-173.

[53] P. Halama, C. Van Haluwin, Antifungal activity of lichen extracts and lichenic acids, BioControl, 49 (2004) 95-107

[54] T. V. Raveendran and V. P. Limna Mol, Natural product antifoulants, Current Science 97 (4) (2009)

[55] Turk Robert, T. F. and Sepcic, K., Mechanisms of toxicity of 3- alkylpyridinium polymers from marine sponge Reniera sarai., Mar. Drugs, 2007, 5, 157–167.

[56] T. Geiger, P. Delavy, R. Hany, J. Schleuniger, M. Zinn, Encapsulated zosteric acid embedded in poly[3-hydroxyalkanoate] coatings – protection against, Biofoul. Polym. Bull., 52 (2004) 65–72.

[57] Dan Rittschof, Natural product antifoulants: One perspective on the challenges related to coatings development, Biofouling, 15 1-3 (2000) 119-127.

[58] M. Boopalan, A. Sasikumar, Studies on biocide free and biocide loaded zeolite hybrid polymer coatings on zinc phosphated mild steel for the protection of ships hulls from biofouling and corrosion, Silicon, 3 (2011) 207–214.

[59] M.H. Fletcher, M.C. Jennings, W.M. Wuest, Draining the moat: disrupting bacterial biofilms with natural products, Tetrahedron, 70 (2014) 6373–6383.

[60] F. Villa, B. Pitts, P.S. Stewart, B. Giussani, S. Roncoroni, D. Albanese, C. Giordano, M. Tunesi, Efficacy of zosteric acid sodium salt on the yeast biofilm model Candida albicans, Microb. Ecol., 62 (2011) 584–598.

[61] D. Pinna, B. Salvadori, M. Galeotti, Monitoring the performance of innovative and traditional biocides mixed with consolidants and water-repellents for the prevention of biological growth on stone, Sci. Total Environ., 423 (2012) 132–141.

[62] E. Nun, M. Oles, B. Schleich, Lotus-Effect® – surfaces, Macromol. Symp., 187 (2002) 677–682.

[63] M. Kuhr, S. Bauer, U. Rothhaar, D. Wolff, Coatings on plastics with the PICVD technology, Thin Solid Films 442 (1–2) (2003) 107–116.

[64] M. Perez, M. Garcia, B. del Amo, G. Blustein, M. Stupak, Core-shell pigments in antifouling paints, Surf. Coat. Int. Part B – Coat. Trans. 86 (4) (2003) 259–262.

[65] L.C. Zhou, B. Koltisko, Development of soft feel coatings with waterborne polyurethanes, Jct. Coatingstech., 2(15) (2005) 54–60.

[66] J.C. Tiller, C.J. Liao, K. Lewis, A.M. Klibanov, Designing surfaces that kill bacteria on contact, Proc. Natl. Acad. Sci. USA 98(11) (2001) 5981–5985.

[67] M. Thouvenin, J.J. Peron, C. Charreteur, P. Guerin, J.Y. Langlois, K. Valle-Rehel, A study of the biocide release from antifouling paints Prog. Org. Coat. 44 (2002)75–83.

[68] S.K. Ghosh, Functional Coatings and Microencapsulation: A General Perspective in Functional Coatings by Polymer Microencapsulation, WILEY-VCH Verlag GmbH & Co. KGaA Weinheim (2006) 1-25.

[69] I. Omae, General Aspects of Tin-Free Antifouling Paints Chem Rev (Washington, DC, U S),103 (2003) 3431.

[70] E. Almeida, T.C. Diamantino, O. De Sousa, Marine paints: The particular case of antifouling paints, Prog. Org. Coat., 59 (2007) 2.

[71] M. A. Trojer, L. Nordstierna, J. Bergek, H. Blanckc, K. Holmberg, M. Nydén, Use of microcapsules as controlled release devices for coatings, Advances in Colloid and Interface Science, 222 (2015) 18–43.

[72] S. Jämsä, R. Mahlberg, U. Holopainen, J. Ropponen, A. Savolainen, A.-C. Ritschkoff, Slow release of a biocidal agent from polymeric microcapsules for preventing biodeterioration, Progress in Organic Coatings, 76 (2013) 269– 276.

[73] L. McCusker, F. Liebau, G. Engelhardt, Nomenclature of structural and compositional characteristics of ordered microporous and mesoporous materials with inorganic hosts(IUPAC Recommendations 2001), Pure and Applied Chemistry, 73(2) (2009) 381-394.

[74] M.A. Malik, M.Y. Wani, M.A. Hashim, Microemulsion method: a novel route to synthesize organic and inorganic nanomaterials: 1st nano update, Arabian J. Chem., 5 (4) (2012) 397-417.

[75] P.A. Lovell, M.S. El-Aasser (Eds.), Emulsion polymerization and emulsion polymers, Wiley, New York, (1997).

[76] H.-D. Dörfler, Grenzflächen und Kolloid-Disperse System, Springer, Berlin, (2002.)

[77] D. Lombardo, M.A. Kiselev, S. Magazù, P. Calandr, Amphiphiles Self-Assembly: Basic Concepts and Future Perspectives of Supramolecular Approaches, Advances in Condensed Matter Physics, Article ID 151683 (2015)

[78] A.C. Chan, M. Bravo Cadena, H.E. Townley, M.D. Fricker, I.P. Thompson, Effective delivery of volatile biocides employing mesoporous silicates for treating biofilms, J. R. Soc. Interface,14 (2017) 20160650.

[79] A. Popat, J. Liu, Q. Hu, M. Kennedy, B. Peters, G. Q. (Max)Lu, S. Z. Qiao, Adsorption and release of biocides with mesoporous silica nanoparticles, Nanoscale, 4(3) (2012) 970–975.

[80] Z. Zheng, X. Huang, M. Schenderlein, D. Borisova, R.Cao, H.Möhwald, D. Shchukin, Self-Healing and Antifouling Multifunctional Coatings Based on pH and Sulfide Ion Sensitive Nanocontainers, Adv. Funct. Mater., 23 (2013) 3307–3314.

[81] M. Michailidis, I. Sorzabal-Bellido, E. A. Adamidou, Y. A. Diaz-Fernandez, J. Aveyard, R. Wengier, D. Grigoriev, R. Raval, Y.Benayahu, R. A. D'Sa, D. Shchukin, Modified Mesoporous

Silica Nanoparticles with a Dual Synergetic Antibacterial Effect, ACS Applied Materials & Interfaces, 9 (44) (2017) 38364-38372.

[82] K. Rózga-Wijas, U. Mizerska, W. Fortuniak, J. Chojnowski , R. Hałasa, W. Werel,Quaternary Ammonium Salts (QAS) Modified Polysiloxane Biocide Supported on Silica Materials, Journal of Inorganic and Organometallic Polymers and Materials, 17 (4) (2007) 605–613.

[83] K. Kermannezhad, A. N.Chermahini, M. M. Momeni, B. Rezaei, Application of amine-functionalized MCM-41 as pH-sensitive nanocontainer for controlled release of 2-mercaptobenzoxazole corrosion inhibitor, Chemical Engineering Journal, 306 (2016) 849–857.

[84] F. Tang, L. Li, D. Chen, Mesoporous silica nanoparticles: synthesis, biocompatibility and drug delivery Adv. Mater., 24 (12) (2012) 1504-1534.

[85] S.H. Wu, C.Y. Mou, H.P. Lin, Synthesis of mesoporous silica nanoparticles, Chem. Soc. Rev., 42 (9) (2013) 3862-75.

[86] R.W. Jones, Fundamental Principles of Sol-Gel Technology (1989).

[87] C. Brinker, G. Scherer, Journal of Non-Crystalline Solids, 70 (1985) 301.

[88] C.J. Brinker, Hydrolysis and condensation of silicates: Effects on structure, Journal of Non-Crystalline Solids, 100 (1988) 31-50.

[89] L.C. Klein, G.J. Garvey, Effect of Water on Acid- and Base-CatalyzedHydrolysis of Tetraethylorthosilicate (TEOS), Mater. Res. Soc. Sym. Proc., (1984) 32.

[90] C. Jeffrey Brinker, Y. Lu, A. Sellinger, H. Fan, Evaporation-Induced Self-Assembly: Nanostructures Made Easy, Adv. Mater, 11 (7) (1999) 579-585.

[91] O.V. Dement'eva, I.N. Senchikhina, E.M. Sedykhb, I.N. Gromyakb, V.A. Ogareva, V.M. Rudoy, Mesostructured SiO_2-based nanocontainers synthesized on a functional template: capacity and rate of unloading, Colloid J., 78 (1) (2016) 52–64.

[92] H. Chen, J. He, H. Tang, C. Yan, Porous Silica Nanocapsules and Nanospheres: Dynamic Self-Assembly Synthesis and Application in Controlled Release, Chem. Mater., 20 (2008) 5894–5900.

[93] K.D. Keefer, The effect of hydrolysis conditions on the structure and growth of silicate polymers, Mater. Res. Soc. Sym. Proc. (1984) 32.

[94] L. L. Hench, J. K. West, The sol-gel process, Chemical Reviews, 90 (1990) 33-72

[95] A. M. Buckley, M. Greenblat, The Sol-Gel Preparation of Silica Gels, Journal of Chemical Education, 71 (7) (1994) 599-602.

[96] R. Zárraga, J. Cervantes, C. Salazar-Hernandez, G. Wheeler, Effect of the addition of hydroxyl-terminated polydimethylsiloxane to TEOS-based stone consolidants, Journal of Cultural Heritage, 11 (2) (2010) 138-144.

[97] T.J. Garino, The cracking of sol gel films during drying, Proceedings of Materials Research Society Symposium, Materials Research Society, San Francisco, 1990, 497–502.V

[98] J. Brus, P. Kotlík, Cracking of organosilicon stone consolidants in gel form, Studies in Conservation, 41 (1996) 55–59.

[99] M.J. Mosquera, M. Bejarano, N. De la Rosa-Fox, L. Esquivias, Producing crack-free colloid-polymer hybrid gels by tailoring porosity, Langmuir, 19 (2003) 951–957.

[100] C. Salazar-Hernández, R. Zárraga, S. Alonso, S. Sugita, S. Calixto, J. Cervantes, Effect of solvent type on polycondensation of TEOS catalyzed by DBTL as used for stone consolidation, Journal of Sol-Gel Science & Technology, 49 (2009) 301–310.

[101] R. Angulo-Olais, Juan F. Illescas, J. Aguilar-Pliego, C. A. Vargas,3 and C. Haro-Pérez, Gel point determination of TEOS-based polymeric materials with application on conservation of cultural heritage buildings, Advances in Condensed Matter Physics, 2018 (2018) Article ID 5784352.

[102] J. Wen, J. E. Mark, Sol-Gel preparation of composites of poly(dimethylsiloxane) with SiO_2 and SiO2/TiO2, and their mechanical properties, Polymer Journal 27 (5) (1995) 492–502.

[103] J. F. Illescas, M. J. Mosquera, Surfactant-synthesized PDMS/silica nanomaterials improve robustness and stain resistance of carbonate stone, The Journal of Physical Chemistry C, 115 (30) (2011) 14624–14634.

[104] L. Pinho, F. Elhaddad, D. S. Facio, M. J. Mosquera A novel TiO_2–SiO_2 nanocomposite converts a very friable stone into a self-cleaning building material Applied Surface Science 275 (2013) 389– 396.

[105] F. Xu, D. Li, Q. Zhang, H. Zhang, J. Xu, Effects of addition of colloidal silica nanoparticles on TEOS-based stone protection using n-octylamine as catalyst, Progrss in Organic Coatings, 75 (2012) 429-434.

[106] K.C. Molloy, T.G. Purcell, D. Cunningham, P. McCardle, T. Higgins, Organotin biocides. X. Synthesis, structure and biocidal activity of organotin derivatives of 2-mercaptobenzothiazole, 2-mercaptobenzoxazole and 2-mercaptobenzimidazole, Applied Organometallic Chemistry, 1(2) (1987) 119–131.

[107] F.E. Dayan, J.G. Romagni, Lichens as a potential source of pesticides, Pesticide Outlook, 12 (2001) 229-232.

[108] R. M. Ribeiro-Costa, A. J. Alves, N. P. Santos,S. C. Nascimento, E. C. P. Gonc¸ Alves, N. H. Silva, N. K. Honda And N. S. Santos-Magalhães, In vitro and in vivo properties of usnic acid encapsulated into PLGA-microspheres, J. microencapsulation, 21 (4) (2004) 371–384.

[109] C. Gazzano, S. E. Favero-Longo, Paola Iacomussi, R. Piervittori, Biocidal effect of lichen secondary metabolites against rock-dwelling microcolonial fungi, cyanobacteria and green algae,International Biodeterioration & Biodegradation, 84 (2013) 300-306.

[110] C. Bille Jendresen, A. Toftgaard Nielsen, Production of zosteric acid and other sulfated phenolic biochemicals in microbial cell factories, Nature Communications, 10 (2019) 4071.

[111] B. Zhang Newby, T. Cutright, C.A. Barrios, Q. Xu, Zosteric acid—an effective antifoulant for reducing fresh water bacterial attachment on coatings, JCT Res., 3 (2006) 69–70.

[112] L. Ruggiero, E. Di Bartolomeo, T. Gasperi, I. Luisetto, A. Talone, F. Zurlo, D. Peddis, M. A. Ricci, A. Sodo, Silica nanosystems for active antifouling protection: nanocapsules and mesoporous nanoparticles in controlled release applications, Journal of Alloys and Compounds, 798 (2019) 144-148.

[113] L. Ruggiero, L. Crociani, E. Zendri, N. El Habra, P. Guerriero, Incorporation of the zosteric sodium salt in silica nanocapsules: synthesis and characterization of new fillers for antifouling coatings, Applied Surface Science, 439 (2018) 705–711.

[114] C. Yu, B. Tian, J. Fan, Nonionic Block Copolymer Synthesis of Large-Pore Cubic Mesoporous Single Crystals by Use of Inorganic Salts, J. Am. Chem. Soc., 124 (2002) 4556-4557.

[115] S. Rajeshkumar, G.M. Anilkumar, S. Ananthakumar, K.G.K. Warrier, Role of drying techniques on the development of porosity in silica gels Journal of Porous Materials, 5 (1) (1998) 59-63.

[116] R. Ryoo, Large Cage Face-Centered-Cubic F*m*3*m* Mesoporous Silica: Synthesis and Structure, J. Phys. Chem. B, 107 (2003) 14296-14300.

[117] W. Chang, J. R. Deka, H. Wu, F. Shieh, S.Huang, H. Kao, Synthesis and characterization of large pore cubic mesoporous silicas functionalized with high contents of carboxylic acid groups and their use as adsorbents, Applied Catalysis B: Environmental, 142–143 (2013) 817-827.

[118] L.C. Cides da Silva, T.V.S. dos Reis, I.C. Cosentino, M.C.a. Fantini, J.R. Matos,R.E. Bruns Factorial design to optimize microwave-assisted synthesis of FDU-1 silica with a new triblock copolymer, Microporous and Mesoporous Materials, 133 (2010) 1-9.

[119] S. Meoto, N. Kent, M. M. Nigra, M. Coppens, Effect of stirring rate on the morphology of FDU-12 mesoporous silica particles, Microporous and Mesoporous Materials, 249 (2017) 61-69.

[120] M. Thommes, K. Kaneko, A.V. Neimark, J.P. Olivier, F. Rodriguez-Reinoso, J. Rouquerol, K.S.W. Sing, Physisorption of gases, with special reference to the evaluation of surface area and pore size distribution (IUPAC Technical Report) Pure and Applied Chemistry, 87 (2015) 1051-1069.

[121] N. K. Raman, M. T. Anderson, C. Jeffrey Brinker, Template-Based Approaches to the Preparation of Amorphous, Nanoporous Silicas, Chem. Mater., 8 (1996) 1682-1701.

[122] F. Maia, A. P. Silva, S. Fernandes, A. Cunha, A. Almeida, J. Tedim , M.L. Zheludkevich, M.G.S. Ferreira, Incorporation of biocides in nanocapsules for protective coatings used in maritime applications, Chemical Engineering Journal, 270 (2015) 150–157.

[123] Z. A. Alothman, A Review: Fundamental Aspects of Silicate Mesoporous Materials, Materials, 5(12) (2012) 2874-2902.

[124] A.K. Rai, R. Singh, K.N. Singh, V.B. Singh, FTIR, Raman spectra ab initio calculations of 2-mercaptobenzothiazole, Spectrochimica Acta Part A, 63 (2006) 483-490.

[125] A. Fidalgo, L.M. Ilharco, Chemical Tailoring of Porous Silica Xerogels: Local Structure by Vibrational Spectroscopy. Chemistry – A European Journal, 10 (2004) 392–398.

[126] L. B. Capeletti, I. M. Baibich, I. S. Butler, J. H.Z. dos Santos, Infrared and Raman spectroscopic characterization of some organic substituted hybrid silicas, Spectrochimica Acta Part A: Molecular and Biomolecular Spectroscopy, 133 (2014) 619-625.

[127] A. Fidalgo, R. Ciriminna, L.M. Ilharco, M. Pagliaro, Role of the alkyl-alkoxide precursor on the structure and catalytic properties of hybrid sol-gel catalysts, Chemistry of Materials, 17 (26) (2005) 6686-6694.

[128] M. A. Azam, B. Suresh, Biological Activities of 2-Mercaptobenzothiazole Derivatives: A Review, Sci. Pharm., 80(4) (2012) 789-824.

[129] A. Alessi, S. Agnello, G. Buscarino, F.M. Gelardi Raman and IR investigation of silica nanoparticles structure, Journal of Non-Crystalline Solids, 362 (2013) 20–24.

[130] A. Alessi, S. Agnello, G. Buscarino and F. M. Gelardi, Structural properties of core and surface of silica nanoparticles investigated by Raman spectroscopy, J. Raman Spectrosc. 2013, 44, 810–816.

[131] K. Zhang, G. A. Hope, A. N. Buckley, H. Li, The interaction of sodium mercaptobenzothiazole with gold electrode and nanorod surfaces, Minerals Engineering, 96–97 (2016) 135-142.

[132] H. Gökce and S. Bahçeli, The Molecular Structures, Vibrational Spectroscopies (FT–IR and Raman) and Quantum Chemical Calculations of n–Alkyltrimethylammonium Bromides, Optics and Spectroscopy, 115 (2013) 632–644.

[133] Q. Mu, T. Chen, Y. Wang, Synthesis, characterization and photoluminescence of lanthanum hydroxide nanorods by a simple route at room temperature, Nanotechnology, 20 (2009) 345602.

[134] X. Wang, X. Liu, X. Wang, Self-assembled synthesis of Ag nanodendrites and their applications to SERS, Journal of Molecular Structure, 997 (2011) 64–69

[135] K. Zhang, G. A. Hope, A. N. Buckley, H. Li, The interaction of sodium mercaptobenzothiazole with gold electrode and nanorod surfaces, Minerals Engineering 96–97 (2016) 135–142 Beattie, D.A., Kempson, I.M., Fan, L.-J., Skinner, W.M., Synchrotron XPS studies of collector adsorption and co-adsorption on gold and gold: silver alloy surfaces. Int. J. Miner. Process., 92 (2009) 162–168.

[136] A. Chenan, S.Ramya, R.P.George, U.Kamachi Mudali, Hollow mesoporous zirconia nanocontainers for storing and controlled releasing of corrosion inhibitors, Ceramics International, 40(2014) 10457–10463.

[137] P. Sarkar, A. Chattopadhyay, Micellar dipole potential is sensitive to sphere-to-rod transition, Chemistry and Physics of Lipids 195 (2016) 34–38.

[138] D. Lombardo, M. A. Kiselev, S. Magazù, P. Calandra, Amphiphiles Self-Assembly: Basic Concepts and Future Perspectives of Supramolecular Approaches, Advances in Condensed Matter Physics Volume 2015, Article ID 151683, 22.

[139] A. Desai, D. Varade, J. Mata, V. Aswal, P. Bahadur, Structural transitions of cetyltrimethylammonium bromide micelles in aqueous media: Effect of additives, Colloids and Surfaces A: Physicochemical and Engineering Aspects, 259 (2005) 111-115.

[140] Howell G.M. Edwards, E. M. Newton, D. D. Wynn-Williams, Molecular structural studies of lichen substances II: atranorin, gyrophoric acid, fumarprotocetraric acid, rhizocarpic acid, calycin, pulvinic dilactone and usnic acid, Journal of Molecular Structure, 651–653 (2003) 27-37.

[141] D. A. Long, Infrared and Raman characteristic group frequencies. Tables and charts George Socrates John Wiley and Sons, Ltd, Chichester, Third Edition, 2001.

[142] I. Aguilar-Hernández, N. Kristian Afseth, T. López-Luke, F. F. Contreras-Torres, J. Petter Wold, N. Ornelas-Soto, Surface enhanced Raman spectroscopy of phenolic antioxidants: A

systematic evaluation of ferulic acid, p-coumaric acid, caffeic acid and sinapic acid, Vibrational Spectroscopy, 89 (2017) 113-122.

[143] J. Ma, X. Zhou, J. Ma, Z. Ji, X. Zhang, F. Xu, Raman Microspectroscopy Imaging Study on Topochemical Correlation Between Lignin and Hydroxycinnamic Acids in Miscanthus sinensis, Microsc. Microanal., 20 (2014) 956–963.

[144] T. Nguyet Tran, P. Pasetto, C. Pichon, D. Bruant, G. Brotons, A. Nourry, Natural rubber based films integrating Zosteric acid analogues as bioactive monomers, Reactive and Functional Polymers,144 (2019) 104343.

[145] M. Thommes, K. Kaneko, A.V. Neimark, J.P. Olivier, F. Rodriguez-Reinoso, J. Rouquerol, K.S.W. Sing, Physisorption of gases, with special reference to the evaluation of surface area and pore size distribution (IUPAC Technical Report) Pure and Applied Chemistry 87 (2015) 1051-1069.

[146] H. Chen, J. He, H. Tang, C. Yan, Porous silica nanocapsules and nanospheres: dynamic self-assembly synthesis and application in controlled release, Chemistry of Materials, 20 (2008) 5894-5900.

[147] C. Yang, J. Zhang, S. Han, X. Wang, L.Wang, W. Yu, Z. Wang, Compositional controls on pore-size distribution by nitrogen adsorption technique in the Lower Permian Shanxi Shales, Ordos Basin, Journal of Natural Gas Science and Engineering, 34 (2016) 1369-1381.

[148] UNI 10923, 2001. Beni culturali: Materiali lapidei naturali ed artificiali. Allestimento di preparati biologici per l'osservazione al microscopio ottico. UNI, Milano.

[149] M.D. Guiry, G.M. Guiry, AlgaeBase Version 4.2. World-wide Electronic Publication. National University of Ireland, Galway http://www. algaebase. org. (2007)

[150] C. Gazzano, S. E. Favero-Longo, P. Iacomussi, R. Piervittori, Biocidal effect of lichen secondary metabolites against rock-dwelling microcolonial fungi, cyanobacteria and green algae. International Biodeterioration & Biodegradation, 84 (2013) 300-306.

[151] D. Pinna, B.Salvadori, M. Galeotti, Monitoring the performance of innovative and traditional biocides mixed with consolidants and water-repellents for the prevention of biological growth on stone. Science of the Total Environment, 423 (2012) 132-141.

[152] K. Schulze, D. A. López, U.M. Tillich, M. Frohme, A simple viability analysis for unicellular cyanobacteria using a new autofluorescence assay, automated microscopy, and ImageJ. BMC biotechnology, 11(1) (2011) 118.

[153] E. K. Kim, J. Won, Jin-young Do, S. D. Kim, Y. S. Kang, Effects of silica nanoparticle and GPTMS addition on TEOS-based stone consolidants, Journal of Cultural Heritage, 10, Issue 2, 2009, 214-221.

[154] J.F. Illescas, M.J. Mosquera, Producing Surfactant-Synthesized Nanomaterials In Situ on a Building Substrate, without Volatile Organic Compounds, ACS Applied Materials & Interfaces, 4 (2012) 4259-4269.

[155] P.N. Manoudis, A. Tsakalof, I. Karapanagiotis, I. Zuburtikudis, C. Panayiotou, Fabrication of super-hydrophobic surfaces for enhanced stone protection, Surface & Coatings Technology, 203 (2009) 1322-1328.

[156] R. Zárraga, J. Cervantes, C. Salazar-Hernandez, G. Wheeler, Effect of the addition of hydroxyl-terminated polydimethylsiloxane to TEOS-based stone consolidants, Journal of Cultural Heritage, 1 (2010) 138.

[157] A. R. Cairncross, F. L. Francis, L. E. Scriven, Predicting drying in coatings that react and gel: Drying regime maps, AlcHem Journal, 46 (1996) 55-67.

[158] C. Milani, M.L. Velo-Simpson, G. W. Scherer, Particle-modified consolidants: a study on the effect of particles on sol-gel properties and consolidation effectiveness, Journal of Cultural Heritage, 8 (2007) 1-6.

[159] L. Pinho, M. J. Mosquera, Titania-Silica Nanocomposite photocatalysts with application in stone self-cleaning, J. Phys. Chem. C, 115 (2011) 22851-22862.

[160] A. Tamayo, J. Rubio, Structure modification by solvent addition into TEOS/PDMS hybrid materials, Journal of Non-Crystalline Solids, 356 (2010) 1742–1748.

[161] J.F. Illescas, M.J. Mosquera, Surfactant-Synthesized PDMS/Silica Nanomaterials Improve Robustness and Stain Resistance of Carbonate Stone, Journal of Physical Chemistry C, 115 (2011) 14624-14634.

[162] X. Zhang, H. Ye, B. Xiao, L. Yan, B. Jiang, Sol−Gel Preparation of PDMS/Silica Hybrid Antireflective Coatings with Controlled Thickness and Durable Antireflective Performance, Journal of Physical Chemistry C, 114 (2010) 19979-19983.

[163] L. Tellez, J. Rubio, F. Rubio, E. Morales, J.L. Oteo, Synthesis of inorganic-organic hybrid materials from TEOS, TBT and PDMS, Journal of Materials Science, 38 (2003) 1773.

[164] D. Li, F. Xu, Z. Liu, J. Zhu, Q. Zhang, L. Shao, The effect of adding PDMS-OH and silica nanoparticles on sol–gel properties and effectiveness in stone protection, Applied Surface Science, 266 (2013) 368– 374.

[165] A. Fidalgo, R. Ciriminna, L. M. Ilharco, M. Pagliaro, Role of the Alkyl-Alkoxide Precursor on the Structure and Catalytic Properties of Hybrid Sol-Gel Catalysts, Chemistry of materials 17, 26, (2005) 6686-6694.

Acknowledgments

Il dottorato è stato un percorso formativo che mi ha permesso di crescere umanamente e professionalmente. Ho compreso che la ricerca scientifica è una scelta di vita impegnativa che richiede il coraggio di confrontarsi con i propri limiti, la determinazione nel superarli e la forza di affrontare le delusioni che ne possono derivare. Ho vissuto questi tre anni donando al mio progetto di ricerca tutta la passione e l'entusiasmo necessari a far crescere un'idea. Durante questa avventura ho avuto la fortuna di interfacciarmi con Professori, ricercatori e dottorandi che mi hanno accolta nei loro laboratori, permettendomi di portare avanti la mia ricerca.

Desidero ringraziare la Prof.ssa Maria Antonietta Ricci per aver creduto nel mio progetto di dottorato, sostenendo le mie idee con competenza e disponibilità.

Vorrei ringraziare la Dott.ssa Armida Sodo per avermi accolto in laboratorio e per aver affrontato con me la sfida di questa ricerca. Oltre ad avermi guidata nello strutturare questo lavoro, i suoi suggerimenti e i suoi insegnamenti mi hanno permesso di crescere come professionista. Un ringraziamento particolare va alla Prof.ssa Tecla Gasperi per aver supportato le mie ricerche con disponibilità e competenza. Vorrei, inoltre, ringraziare la Dott.ssa Barbara Capone, il Prof. Marco Barbieri e il Prof. Fabio Bruni per avermi coinvolta nelle loro interessanti attività di ricerca, dandomi la possibilità di contribuire.

Vorrei, inoltre, ringraziare la Dott.ssa Simonetta Tuti, la Prof.ssa Elisabetta Di Bartolomeo e la Dott.ssa Francesca Zurlo per avermi permesso di portare avanti questo progetto utilizzando diverse tecniche analitiche.

Vorrei, inoltre, ringraziare il Dott. Davide Peddis per avermi ospitata nel suo laboratorio mettendomi a disposizione spazi e strumentazione.

Desidero ringraziare la Prof.ssa Giulia Caneva per aver apprezzato il mio progetto di dottorato a tal punto da proporlo alla Regione Lazio nella call "Gruppi di Ricerca". Inoltre, vorrei ringraziare la Dott.ssa Flavia Bartoli e la Dott.ssa Maria Rosaria Fidanza per aver lavorato al mio fianco durante le prime fasi del progetto SUPERARE, occupandosi degli aspetti biologici della ricerca.

Infine, desidero ringraziare gli amici di sempre che mi sono stati accanto e i colleghi di laboratorio che con il tempo sono diventati compagni di avventura e amici sempre presenti. L'affetto e il sostegno che mi hanno dimostrato rendono questo traguardo ancora più prezioso.

Un ringraziamento speciale va ai miei genitori che mi hanno sempre incoraggiata a seguire con determinazione le mie passioni e a credere nelle mie potenzialità. Ringrazio mia sorella, amica di una vita e per la vita. Grazie per la complicità che ci lega. Grazie perché, nonostante le differenze caratteriali, sai sempre come starmi vicina.

Un grazie di cuore ad Alessandro che con la sua sensibilità e il suo saper essere premuroso e attento mi è stato sempre accanto con amore.